Eva Schlenker

ZnO based Nanostructures – Properties and Device Applicability

Cuvillier Verlag Göttingen
Internationaler wissenschaftlicher Fachverlag

ZnO based Nanostructures - Properties and Device Applicability

Von der Fakultät für Elektrotechnik, Informationstechnik, Physik
der Technischen Universität Carolo-Wilhelmina zu Braunschweig

zur Erlangung der Würde einer

Doktor-Ingenieurin (Dr.-Ing.)

genehmigte Dissertation

von:	Eva Schlenker
aus:	Villingen-Schwenningen
eingereicht am:	13. Januar 2009
mündliche Prüfung am:	13. Februar 2009
Referenten:	Prof. Dr. rer. nat. A. Waag Prof. Dr.-Ing. W. Kowalsky

2009

Bibliografische Information der Deutschen Nationalbibliothek
Die Deutsche Nationalbibliothek verzeichnet diese Publikation in der Deutschen Nationalbibliografie; detaillierte bibliografische Daten sind im Internet über http://dnb.ddb.de abrufbar.
1. Aufl. - Göttingen : Cuvillier, 2009
Zugl.: (TU) Braunschweig, Univ., Diss., 2009

978-3-86727-967-3

Nonnenstieg 8, 37075 Göttingen
Telefon: 0551-54724-0
Telefax: 0551-54724-21
www.cuvillier.de

1. Auflage, 2009
Gedruckt auf säurefreiem Papier

978-3-86727-967-3

Contents

Summary

As miniaturization increases down to nanometer scales, conventional device processing techniques will finally reach their limits. Further shrinking of the chip dimensions can therefore only be ensured by applying bottom-up pattering methods that rely on the incorporation of nanostructures into the devices.
In recent years, a lot of effort has been put in the controlled synthesis of nanowires, nanopillars or nanobelts. In particular, nanostructures based on zinc oxide (ZnO) attracted much attention, since ZnO not only has the property of self-organized growth, but the resulting nanowires are also of highly crystalline quality. However, in order to take full advantage of the benefits offered by the multifunctional semiconducting nanostructures, they should be characterized in detail.

This work focuses on the electrical and magnetic properties of ZnO based nanowires and nanopowder particles. Thus, in the first part of the thesis, the electrical transport properties of single nanowires are investigated and the influence of changes in ambient conditions (illumination, atmosphere, humidity) on the conductivity is examined. Therefore, current-voltage and photoresponse measurements in various ambient conditions were performed on single ZnO nanowires as well as on layers consisting of ZnO nanopowder particles. Additionally, a comprehensive comparison of literature data concerning the resistivity values of ZnO nanowires is presented.
In the second part, the structural and magnetic features of ZnO nanostructures diluted with Mn-, Co- and V-ions are analyzed. Besides studying their chemical composition and their structural properties by X-ray diffraction, transmission electron microscopy, energy dispersive X-ray spectroscopy and electron energy loss spectroscopy measurements, main focus is on their magnetic features. As magnetic investigation tools serve SQUID magnetometry and magnetic force microscopy (MFM).

Finally, the gained knowledge is used to propose some novel device concepts.

Electrical properties

Single ZnO nanowires grown by vapor phase transport (VPT) are contacted employing electron-beam lithography. The current-voltage characteristics show a rectifying behavior resulting from Schottky contacts of different barrier heights. The deduced ideality factors strongly deviate from unity. This is attributed to the existence of an insulating layer between the metal contact and the nanowire.
From the determined resistivity values of the nanowires an estimate of the charge carrier concentration is deduced. The resistivities are quite high and the calculated charge carrier concentration is therefore rather low. This is attributed to a reduced effective cross-section for current transport as compared to the geometrical cross-section of the nanowire due to the existence of a surface depletion layer. This layer is caused by band bending effects resulting from Fermi level pinning at surface states.
Photoresponse measurements show a strong increase in current when the sample is illuminated with light having energy above the band gap energy. The photocurrent decay times are in the order of several minutes. The photocurrent can hence not only be attributed to the generation of electron-hole pairs, but is also due to a chemical modification of the surface induced by photon irradiation.
Based on these observations, a dynamic ”core-shell” model is developed that describes the experimental results. The model states the existence of a surface charge depletion layer (”shell”) of low conductivity surrounding the conductive bulk material (”core”) of the nanowire. The depletion layer is caused by adsorbates present on the ZnO surface. The surface states and therefore the conductivity of the nanowire can be modified by illumination with UV light. The system returns to the original state when the UV light is turned off again. Consequently, it is a reversible dynamic process.

A comprehensive comparison of literature data reveals significant differences in the reported resistivity values of nanowires grown from the gas phase. Factors that might influence the resistance measurements are analyzed and discussed in detail. At last, it is concluded that the discrepancies can not be attributed to a single reason, but they result from the interaction of multiple factors like the influence of ambient conditions (light, atmosphere) and the growth methods applied.

Furthermore, electrical transport investigations of nanowires synthesized by aqueous chemical growth (ACG) were performed. Different contacting methods were applied; however, independent on the method used, the deduced resistivities of the ACG grown nanowires are at least one order of magnitude lower than the values determined of the nanowires that are grown from the gas phase. The decrease in resistivity is assigned to

the increased number of point defects or residual impurities (like hydrogen) present in the crystal structure resulting in higher charge carrier concentrations.

Finally, the influence of illumination and ambient conditions (gas composition, humidity) is studied employing ZnO layers consisting of nanopowder particles. It is found that such porous layers are especially suitable for this kind of investigation since they exhibit an enormous surface to volume ratio. The measurements demonstrate that UV illumination increases the conductivity of the nanopowder layer by at least four orders of magnitude. Detailed investigations reveal that oxygen as well as water molecules present in the atmosphere strongly influence the photoresponse and the photocurrent decay times. These findings provide further confirmation of the correctness of the suggested dynamic ”core-shell” model.

Magnetic properties

ZnO based nanostructures diluted with Mn-, Co- and V-ions are investigated. The SQUID measurements performed on an ensemble of Mn doped nanopowder particles showed pure diamagnetism for temperatures exceeding 75 K, while at lower temperatures ($T < 75$ K), the overall observed signal indicates paramagnetic features. MFM investigations serve to analyze the magnetic features of individual particles. A pronounced magnetic contrast is particularly visible in some particles, while for other particles no contrast is detected. These results are consistent with the findings obtained from energy dispersive X-ray spectroscopy measurements that reveal an inhomogenous distribution of the Mn transition metal ions in the nanopowder.

Furthermore, Co doped ZnO nanopowders are investigated. The observed magnetic features are similar to the ones measured for the Mn-doped sample. So neither in the Mn- nor the Co-doped sample evidence for ferromagnetism can be found.

In addition to the investigations of the nanopowders, also studies of ZnO nanowires implanted with V-ions were performed. Transmission electron micrographs reveal a severely damaged material after implantation and annealing. Nevertheless, the MFM images taken after the application of an external magnetic field correspond to the images expected for multiple stacked magnetic dipoles and strongly indicate ferromagnetism at room temperature.

Device concepts

Finally, based on the findings presented in this work, some novel device concepts are proposed.
A porous layer consisting of ZnO nanopowder particles serves as gas sensing element in an oxygen sensor. It is found that oxygen molecules present in the atmosphere not only significantly reduce the photoresponse of the nanopowder samples upon UV illumination but also lead to a reduction of the photocurrent decay time. Therefore both the decay time and the maximum current correlate with the oxygen partial pressure in the atmosphere.

Furthermore, the concept and the results of the first experiments towards the realization of a magnetically-sensitive transistor are presented. A ZnO based spin-FET can be realized by utilizing undoped ZnO nanowires as non-magnetic channel while selected V implanted regions serve as ferromagnetic contacts.

Additionally, atomic force microscopy measurements were performed of V doped ACG grown nanowires. The images that were taken with or without application of an in-plane oriented external field show that the orientation of the nanowires can be switched between a vertical and horizontal alignment by applying a magnetic field. Therefore, a device concept is suggested employing nanowires as magnetically controlled nanoscale switches in electric circuits.

Zusammenfassung

Aufgrund der ständig fortschreitenden Miniaturisierung werden technologische Komponenten in nächster Zeit Abmessungen erreichen, die mit konventionellen Strukturierungstechniken nicht mehr zu realisieren sind. Um in noch kleinere Dimensionen vorzustoßen, sind Herstellungsmethoden, die auf dem "bottom-up" Prinzip und auf dem Einbau von Nanostrukturen beruhen, unabdingbar.

In den letzten Jahren wurden bemerkenswerte Fortschritte in der Herstellung von Nanodrähten erzielt. Ein Schwerpunkt lag dabei auf der Synthese von Zinkoxid (ZnO) basierten Nanostrukturen. ZnO bietet nicht nur den Vorteil, dass es selbstorganisiert wächst, sondern die erhaltenen Nanodrähte sind auch von hoher kristalliner Qualität. Um das Potenzial dieser multifunktionalen halbleitenden Nanostrukturen vollständig ausnutzen zu können, müssen diese zunächst genauestens charakterisiert werden.

In dieser Arbeit werden die elektrischen und magnetischen Eigenschaften von ZnO basierten Nanodrähten und Nanopulvern hinsichtlich der Verwendung in elektronischen und spintronischen Bauelementen untersucht. Ebenfalls evaluiert wird ihr Einsatzpotenzial in der Gassensorik. Der erste Teil dieses Manuskripts widmet sich daher den Ergebnissen elektrischer Transportmessungen an einzelnen Nanodrähten. Neben Photoleitfähigkeitsmessungen wird zudem der Einfluss der äußeren Bedingungen (Gaszusammensetzung der Atmosphäre, Luftfeuchtigkeit) auf die Leitfähigkeit der Nanostrukturen untersucht. Zusätzlich wird ein umfangreicher Überblick über die in der Literatur angegebenen Widerstände von einzelnen ZnO Nanodrähten gegeben und diskutiert.

Der zweite Abschnitt befasst sich mit den magnetischen Eigenschaften von mit Mn, Co und V dotierten ZnO Nanostrukturen. Neben der Untersuchung der chemischen und strukturellen Eigenschaften mittels Röntgendiffraktometrie, Transmissionselektronenmikroskopie, Energie-dispersiven Röntgen-Spektroskopie und Elektronen-Energieverlust-Spektroskopie Messungen, liegt der Schwerpunkt dieses Abschnitts auf den magnetischen Eigenschaften der Nanostrukturen. Zur Analyse werden dazu SQUID Magnetometrie und magnetische Rasterkraft-Mikroskopie Messungen herangezogen.

Schließlich werden einige Bauelement-Entwürfe vorgestellt, deren Funktionsprinzipien auf den neu gewonnenen Erkenntnissen beruhen.

Elektrische Eigenschaften

Nanodrähte aus der Gasphase wurden unter Zuhilfenahme von Elektronenstrahl-Lithographie (zur Strukturierung der Leiterbahnen) elektrisch kontaktiert. Die Kennlinien der Nanodrähte zeigen ein gleichrichtendes Verhalten, was auf Schottky-Kontakte mit unterschiedlichen Barrierenhöhen schließen lässt. Auch die bestimmten Idealitätsfaktoren weichen von dem zu erwartenden Wert einer idealen Diode ab. Dies weist darauf hin, dass sich zwischen dem Kontaktmetall und dem Nanodraht noch eine isolierende Zwischenschicht befindet.

Aus den ermittelten Widerstandswerten der Nanodrähte wird eine Ladungsträgerkonzentration abgeschätzt. Da die Nanodrähte sehr hochohmig sind, ist die berechnete Ladungsträgerkonzentration sehr gering. Dies wird darauf zurückgeführt, dass zur Bestimmung des spezifischen Widerstands der geometrische Querschnitt des Nanodrahts verwendet wird. Allerdings weisen der verhältnismäßig hohe Wert des spezifischen Widerstands und die daraus resultierende niedrige Ladungsträgerkonzentration darauf hin, dass der effektive Querschnitt für den Stromtransport gegenüber dem geometrischen Querschnitt reduziert ist. Aufgrund von Oberflächenzuständen am Nanodraht kommt es zum Pinning des Ferminiveaus und somit zu Bandverbiegungseffekten in den Nanodraht hinein. Eine Oberflächen-Verarmungszone bildet sich aus.

Bei Beleuchtung des Nanodrahts mit Licht einer Energie, die über der Bandlückenenergie von ZnO liegt, steigt der Strom deutlich an. Die damit zusammenhängenden Zeitkonstanten dieser Photoleitung bei Abschalten des Lichts liegen im Bereich von mehreren Minuten. Dies lässt darauf schließen, dass die aufgezeichneten Reaktionen auf Oberflächen- und nicht (ausschließlich) auf Volumen-Effekte zurückzuführen sind.

Basierend auf diesen Beobachtungen wird ein sogenanntes dynamisches ”core-shell” Modell entwickelt, welches die experimentellen Ergebnisse adäquat beschreibt. Das Modell postuliert die Existenz einer nicht leitenden Schicht (Oberflächenverarmungszone, ”shell”) um den leitfähigen Kern (”core”) des Nanodrahts. Die Verarmungszone resultiert von Adsorbaten an der Oberfläche des Nanodrahts. Die Beleuchtung mit UV Licht bewirkt eine Änderung der Oberflächenzustände (und folglich auch der Leitfähigkeit des Nanodrahts). Nach Abschalten des UV Lichts kehrt das System in den ursprünglichen Zustand zurück. Dieser Vorgang ist somit ein reversibler dynamischer Prozess.

Weiter beinhaltet diese Arbeit eine Literaturübersicht von spezifischen Widerständen von Nanodrähten, die aus der Gasphase abgeschieden wurden. Die Zusammenstellung offenbart signifikante Unterschiede in den publizierten Daten. Mögliche Faktoren, die das Ergebnis elektrischer Transportmessungen beeinflussen können, werden analysiert und ausführlich diskutiert. Die Untersuchungen zeigen, dass die beobachteten Abweichungen nicht auf den Einfluss einzelner Faktoren zurückgeführt werden können. Sie resultieren vielmehr aus dem Zusammenspiel diverser Faktoren wie Umgebungsbedingungen (Licht, Atmosphäre) und verwendete Wachstumsmethoden.

Transportmessungen wurden ebenfalls an nasschemisch gewachsenen Nanodrähten durchgeführt, wobei unterschiedliche Kontaktierungsmethoden angewandt wurden. Unabhängig von der gewählten Methode zeigen die nasschemisch hergestellten Strukturen eine um mindestens eine Größenordnung höhere Leitfähigkeit als die Nanodrähte, die aus der Gasphase abgeschieden wurden. Die erhöhte Leitfähigkeit wird einer vergrößerten Zahl von Punktdefekten oder Fremdatomen (wie Wasserstoff) im Kristall zugeordnet, die in einem Anstieg in der Ladungsträgerkonzentration resultieren.

Weiter wird die Sensitivität der ZnO Nanostrukturen gegenüber Änderungen in der Beleuchtung und in den äußeren Bedingungen (Gaszusammensetzung der Atmosphäre, Luftfeuchtigkeit) untersucht. Die Messungen wurden an schichtähnlichen Strukturen bestehend aus undotierten ZnO Nanopartikeln durchgeführt. Diese eignen sich aufgrund ihrer großen Oberfläche aber dennoch hohen Beständigkeit und leichten Handhabung besonders für solche Untersuchungen.
Bei Beleuchtung mit UV Licht steigt der Strom um mindestens vier Größenordnungen an. Ausführliche Untersuchungen zeigen weiter, dass Sauerstoff und Wassermoleküle in der Atmosphäre die Höhe und die Abklingzeit des Photostroms stark beeinflussen. Die gewonnenen Ergebnisse bestätigen das zuvor vorgestellte ”core-shell” Modell.

Magnetische Eigenschaften

Mit Mn-, Co- und V-Ionen dotierte ZnO Nanostrukturen werden untersucht. Die SQUID Messungen an einem Ensemble von mit Mn dotierten Nanopartikeln (Pulver) zeigen bei Temperaturen über 75 K ein rein diamagnetisches Signal, während bei tiefen Temperaturen ($T < 75$ K) lediglich ein paramagnetisches Verhalten detektiert werden kann.
Die magnetischen Eigenschaften einzelner Nanopartikel werden anhand von magnetischen Rasterkraft-Mikroskopie Messungen untersucht. In einigen Nanopartikeln ist der

magnetische Kontrast besonders ausgeprägt, während für andere nahezu kein Signal erkennbar ist. Diese Resultate stimmen mit den Ergebnissen aus Energie-dispersiven Röntgen-Spektroskopie Messungen überein, die eine inhomogene Verteilung der Mn-Ionen in den Nanokristallen offenbaren.
Auch mit Co dotierte ZnO Nanopulver wurden untersucht. Die Proben zeigen ein ähnliches Verhalten wie die mit Mn dotierten Pulver. Letztlich führte weder die Dotierung mit Mn noch mit Co zu ferromagnetischen Eigenschaften der Proben.

Neben den Nanopulvern wurden auch Untersuchungen an ZnO Nanodrähten durchgeführt, die mit V implantiert wurden. Transmissionselektronenmikroskopie Aufnahmen belegen, dass die Kristallstruktur der Nanodrähte nach der Implantation und auch noch nach dem Anlassen erheblich geschädigt ist. Dennoch zeigen magnetische Rasterkraft-Mikroskopie Bilder, die nach dem Anlegen eines externen magnetischen Feldes aufgenommen wurden, deutlich magnetische Kontraste. Die Aufnahmen zeigen Muster, die den Feldlinienverläufen von mehreren aufeinander gestapelten Stabmagneten entsprechen. Die Ergebnisse geben daher starke Hinweise auf ein ferromagnetisches Verhalten bei Raumtemperatur.

Anwendungen

Die in den vorherigen Kapiteln gewonnenen Ergebnisse werden herangezogen, um einige Bauelement-Anwendungen vorzustellen.
Eine poröse Schicht (bestehend aus ZnO Nanopartikeln) dient als sensitives Element in einem Sauerstoff-Sensor. Die Anzahl der Sauerstoff-Moleküle in der Atmosphäre reduziert nicht nur den Anstieg des Photostroms unter UV Beleuchtung, sondern verringert auch die Abklingdauer nach Abschalten des Lichts. Sowohl die Abklingzeit als auch der maximal detektierte Strom geben daher Aufschluss über den Sauerstoff-Partialdruck in der Atmosphäre. Der Sensor wird auf seine Genauigkeit und Zuverlässigkeit getestet.

Zusätzlich werden das Konzept und die ersten Experimente hinsichtlich der Realisierung eines Spin-sensitiven Transistors präsentiert. Ein undotierter ZnO Nanodraht dient dabei als nicht-magnetischer Kanal, während selektiv implantierte Bereiche die ferromagnetischen Kontakte zur Spininjektion bilden.

Ferner wurden Rasterkraft-Mikroskopie Aufnahmen an mit V-Ionen implantierten nasschemisch gewachsenen Nanodrähten durchgeführt. Die Messungen zeigen, dass sich die Ausrichtung (stehend oder liegend) der Nanodrähte durch Anlegen eines externen magnetischen Feldes verändern lässt. Die Nanodrähte können aufgrund dieser Eigenschaft auch als magnetisch kontrollierbare nanoskalige Schalter in elektrischen Schaltungen eingesetzt werden.

Chapter 1

Introduction

”Nanowires, nanorods or nanowhiskers. It doesn’t matter what you call them, they’re the hottest property in nanotechnology.”

These are the opening sentences of an article published in *Nature* in 2002 [1], where the author[1] attributes the remarkable progress made in the field of nanotechnology in the recent decade to the discovery and controlled synthesis of carbon nanotubes [2] and semiconducting nanowires [3] that can serve as a basis for various device structures. Devices based on nanowires combined with bottom-up (instead of top-down) patterning techniques will not only ensure a further shrinking of the chip dimensions down to nanometer scales, but will also considerably upgrade their performances at a reduced electrical power consumption. Especially semiconducting nanowires seem advantageous for device applications, since they grow in a self-organized process and their chemical composition can be tailored, too.
Today, semiconducting nanowires and nanoparticles, or nanostructures in general, are already employed in various applications. Nanowires are mostly incorporated in electronic devices like nanoscale field effect transistors [4] and logic gates [5] or in optoelectronic devices [6], whereas nanoparticles, because of their enormous surface to volume ratio, are preferentially used as sensing elements in gas or humidity detectors.

Among research on semiconducting nanostructures, especially nanowires based on zinc oxide (ZnO) recently attracted much attention. The II-IV semiconductor has the property of self-organized growth leading to a variety of shapes like nanowires, nanorings, nanobelts and nanoparticles. The resulting structures are of high crystallinity with low defect densities and the dimensions are controllable by adjusting the growth parameters.

---

[1] D. Appell, freelance science writer.

With a direct band gap of 3.37 eV and an exciton binding energy of 60 meV at room temperature, ZnO is a promising candidate for optoelectronic applications. Additionally, growth may result in ordered and well aligned nanowire arrays building regular block structures that can be used, for instance, as basis for high density pixel arrays in displays and LEDs. Furthermore, the environmentally friendly, long-term stable, radiation and oxidation resistant material is also valued for its piezoelectric features that can be exploited for power generation [7].

Changes in ambient conditions strongly influence the electrical properties of ZnO nanostructures, a property that can be employed for detection of oxidizing and reducing gases. Moreover, besides the use in electronics, optoelectronics and sensorics, ZnO could also form the basis for spintronic devices: Theoretical calculations predict that when doped with transition metal (TM) ions, ZnTMO should exhibit ferromagnetism even at room temperature [8, 9].

ZnO nanostructures have many unique properties; however, in order to fully exploit their functionality, it is important not only to study their electrical transport characteristics in a laboratory environment, but also to thoroughly investigate their behavior upon changing atmospheric and light conditions. Even though many groups have already examined the electrical properties and also the photoresponse of ZnO upon UV illumination, the discrepancies in the reported photocurrent decay times (ranging from nanoseconds [10] up to minutes [11]) reveal that the photocurrent mechanism is very complex and not yet fully understood. One objective of this work is therefore to deliver a complete investigation of the electrical transport properties of ZnO nanostructures and to provide a model describing the observed effects. The analysis is subdivided into the investigation of nanowires grown by vapor phase transport and by aqueous chemical growth. Also layers consisting of ZnO nanopowder particles are examined.

Furthermore, there are still some open questions regarding the applicability of transition metal doped ZnO for spin sensitive devices. The magnetic properties of ZnTMO layers have already been extensively studied; however, due to considerable differences in the observed experimental results, ferromagnetism in ZnTMO is still under debate. While most investigations focus on layers, only few reports deal with research on magnetic ZnO nanowires or nanostructures. The second aim of this thesis is therefore to investigate Mn-, Co- and V-doped ZnO nanostructures concerning their magnetic properties and their applicability as basis for spin-sensitive devices.

Finally, one more goal is to present device structures and concepts based on the obtained results.

The thesis is structured as follows:

Chapter 2 shortly recapitulates the historical development of nanotechnology by presenting some of the major discoveries and findings as well as a number of the technological progresses involved. Furthermore, some semiconducting nanowire based devices are presented.

Chapter 3 introduces the basic properties of the semiconducting material ZnO, the specific characteristics of ZnO nanostructures and the synthesis techniques involved in this work.

Chapter 4 presents the electrical property studies of ZnO nanostructures. The first part deals with the investigation of nanowires grown by vapor phase transport. Additionally, an overview of published data concerning the resistivities of nanowires is given and factors influencing the resistance are discussed. The second part investigates the transport characteristics of nanowires grown in an aqueous chemical process and contacted using various methods. The results concerning the influence of illumination and ambient conditions on the electrical properties of nanopowder layers complete this chapter.

After a short introduction of magnetism in semiconductors, Chap. 5 shows the results from the magnetic property investigations of Mn-, Co- and V- doped ZnO nanostructures.

Chapter 6 presents a few device concepts based on the findings presented in the previous chapters.

A short outlook completes this work.

Furthermore, it should be pointed out that even though quasi zero- and one-dimensional structures (like quantum dots, quantum wells or thin films) are also referred to as nanostructures (by definition, nanostructures have *at least* one dimension on the nanometer scale), in this thesis, the term nanostructures or nanosystems is exclusively used for structures having two or three dimensions on the nanoscale.

Chapter 2

Single crystal nanosystems

Already in the 1950's, the miniaturization of devices and instruments was regarded as a highly important challenge. However, in contrast to today's definition of smallness, at that time people were referring to dimensions below 1 mm^2.
In 1959, at the annual meeting of the American Physical Society, R. P. Feynman delivered the after dinner speech entitled ”There is plenty of room at the bottom” in which he forecasted the possibilities and the potentials of miniaturization that he considered wide beyond the level achieved at that time [12]. While some regard his speech as the first reference to the concepts of nanotechnology, it actually took another 15 years until the term ”nanotechnology” was first used by N. Taniguchi [13] in 1974. From that time on, research and applications based on nanostructures rapidly increased. While first reports dealing with the achievements in the field of organic nanotechnology date back to the year 1974, it took almost another quarter of a century till inorganic semiconducting nanostructures finally found application in nanoscale devices.

The following sections present a short overview of the historical development of the nanotechnology approach. Furthermore, the advantages and disadvantages of using semiconducting nanowires in comparison to organic materials and thin films are discussed. A number of selected nanowire based applications are depicted with a special focus on ZnO based nanostructures.

2.1 Historical development of nanotechnology: Discoveries and experimental advances

Even though nanostructures, mostly silver or copper particles, have already been unwittingly used back in the 9^{th} century to generate a glittering effect on pottery, the knowledge of nanotechnology we have today was not gained until the last decades due to enhanced and interdisciplinary research in the fields of chemistry, biochemistry, physics and engineering. First respectable results were reported in the field of organic materials in 1974, when Aviram and Ratner proposed that molecules might serve as electronic elements [14]. They presented a rectifier based on a single molecule and suggested that all circuit components of a computer might be built out of individual molecules. Another major breakthrough in this field was achieved in 1977/78 by A. J. Heeger, A. G. MacDiarmid and H. Shirakawa who discovered that doping of organic polymers is possible[1] [15].

Quick development steps followed. In 1980, Sagiv *et al.* found out that specific molecules spontaneously react with glass surfaces and assemble themselves into individual layers [16], and shortly after, Nuzzo and Allara showed that some molecules also self-assemble into individual or monolayers [17]. These findings provided the basis to form 3-dimensional structures in a layer-by-layer deposition process, a method that can be used to build molecular based electronic devices.

But also technical innovations led to further progress in miniaturization. In 1981, Binning *et al.* presented the first scanning tunneling microscope (STM) [18, 19] and five years later, the atomic force microscope (AFM) was invented [20].

In the mid 80's, C. W. Tang and S. Van Slyke achieved pioneering successes in the field of molecular electronics. In 1986, they presented an organic photovoltaic cell achieving a power conversion efficiency of about 1 % [21], and only one year later, they reached an external quantum efficiency of 1 % with a light emitting diode (LED) consisting of a double layer structure of organic thin films [22]. At around the same time, in 1984, Kudo *et al.* presented the first organic field-effect transistor [23].

Not only in the field of organic semiconductors research proceeded, also inorganic semiconducting nanosystems were intensively studied. A significant contribution in the field of semiconducting particles was made in 1983, when Brus *et al.* discovered that nanocrystals of the same material but differing in size exhibited different colors [24].

---

[1] For their discovery they were awarded the Nobel prize in chemistry in 2000.

The nanoparticles were later referred to as quantum dots and the observed effect was attributed to quantum confinement.

So far, most nanoscale devices were based on organic molecules and their property of self-assembly, but in 1990, Eigler and Schweizer achieved the positioning of single Xe atoms in a STM set-up. This enabled the fabrication of structures with all kinds of desired designs and demonstrated the capability for further device miniaturization [25].

Nanoscience of inorganic materials got another boost in 1991, when S. Iijima discovered the existence of carbon nanotubes (CNTs) [2]. He found several tubes nested inside each other, therefore the structures were referred to as multi-wall CNTs. Only a short period later, the groups around D. S. Bethune and S. Iijima independently developed a method to fabricate single-wall CNTs [26, 27]. However, it took another four years until the first carbon nanotube single-electron transistors [28, 29] and field-effect transistors (FETs) [30, 31] were actually presented in 1997.

But not only research in the field of CNTs advanced, also an intensified interest in semiconducting nanowires was triggered which was mainly due to the results achieved by the groups of C. Lieber, Z. L. Wang, P. Yang, and L. Samuelson [3, 32–34] and only shortly after, sophisticated devices incorporating nanowires were presented [5, 35, 36].

Today, despite of the relatively short development phase, inorganic semiconducting nanostructures already found their way into everyday applications and serve more and more as substitutes for thin films. The following section discusses the benefits of using nanostructures and presents some applications.

2.2 Semiconducting nanosystems between molecular electronics and thin films

Traditionally, the fabrication of electronic components or integrated circuits relies on the patterning of silicon films or wafers. The manufacturing of silicon has already been known and optimized for years, its electronic properties are fully under control and the technology processes required for structuring the devices are well established and very successful techniques. Usually top-down methods like etching, deposition and lithography are used to form individual components into the wafers. Over the years, the permanent improvement of the technology concepts ensured the continuous downsizing of the chip dimensions. However, when it comes to nanometer scales, top-down approaches will no longer be the method of choice, since the technological effort required for further miniaturization gets increasingly complex and demands expensive equipment. Therefore the quest is on to develop new strategies, like using self-organized growth methods and bottom-up instead of top-down patterning approaches. Electronic circuits incorporating organic molecules or inorganic semiconducting nanostructures might push miniaturization limits even further and might additionally enhance the device performances.

Today, organic nanomaterials already find application in everyday products like displays of mobile phones, TV screens and photocopy machines. There are numerous benefits of the molecular approach. One major advantage of organic structures is that they can be easily produced on a large scale at very low costs. No crystalline films and therefore no expensive growth methods are required; the films can simply be applied by spin-coating, evaporation or ink jet printing. Since no high temperature steps are involved, all kinds of substrates, including flexible ones, can be used. In summary, the molecular approach enables the production of low-cost flexible electronics on a large scale. However, there are also some factors curtailing the expectations of this material. Generally, organic films have low charge carrier concentrations and mobilities. Furthermore, regarding the long term stability, encapsulation is indispensable since organic materials willingly react with oxygen.

In recent years, much research has been performed in the field of inorganic nanostructures, like CNTs and semiconducting nanostructures for the use in electronic components. Nanotubes/wires are comparably easy to synthesize and are usually of highly crystalline quality. Furthermore, they have an extremely large surface to volume ratio which is advantageous regarding gate-effects and charge carrier control. This also indicates that nanowires are especially sensible to changes in ambient conditions which makes them ideal candidates for gas sensing and light detecting applications.

While it is difficult to control the metallic or semiconducting properties of CNTs, semiconducting nanostructures still exhibit the electronic properties of the volume material, even if their diameter is just a few tens of nanometers. This implies that after synthesis, each semiconducting nanowire has the same defined crystal properties as the corresponding bulk material. Therefore band-gap engineering and doping to alter electronic or magnetic properties known from research on the bulk material are also applicable for nanowires and nanopowders.

Nanostructures can be synthesized by a number of relatively easy and cost-effective processes. Mostly vapor deposition techniques are applied, relying on thermal evaporation and recondensation of the material itself or its compounds. But also low-temperature wet chemical approaches exist; permitting growth on flexible substrates too.

In short, inorganic semiconducting nanostructures perfectly combine the benefits offered by organic semiconductors, namely the use of flexible substrates and relatively cost-effective growth methods, and the advantages offered by thin film approaches like control of the composition and the structural properties.

Numerous devices have been presented by now. Whereas semiconducting nanoparticles have already been used for some time in everyday products like UV absorbers in sun screen or gas detectors in sensors, most devices based on nanowires are still in the laboratory stage. In the following sections, some applications will be presented.

2.3 Devices based on semiconducting nanowires

There are several publications reporting the successful application of nanowires in electronics, opto-electronics, sensorics and power generation on a laboratory scale. Some of the implementation approaches are presented in the following .

2.3.1 Electronic devices

A bipolar transistor was realized by Cui and Lieber by crossing p- and n-type silicon (Si) nanowires [37]. The nanowires were synthesized using a laser-assisted catalytic growth method and were doped either with boron (p-type Si) or phosphorus (n-type Si). By sequentially depositing the p-/n-type nanowires out of a solution onto a substrate or by manipulation, p-n junctions and n^+-p-n structures were formed. The contacts were defined by employing electron-beam (e-beam) lithography. Figure 2.1 shows the schematic and the corresponding field emission (FE) scanning electron microscopy (SEM) images of the n^+-p-n Si nanowire bipolar transistor.

The n^+- nanowire functions as emitter, while the p- and n-type nanowires respectively serve as base and collector. The nanowire bipolar transistor exhibited behavior similar to the behavior found in standard thin film devices.

There are numerous publications reporting the implementation of nanowires in FETs and also several different concepts to realize such devices exist. One simple method is to deposit the nanowires on a conductive substrate covered by an isolating layer (like a SiO_2 covered Si wafer) that serves as gate electrode. Mostly, the source and drain contacts

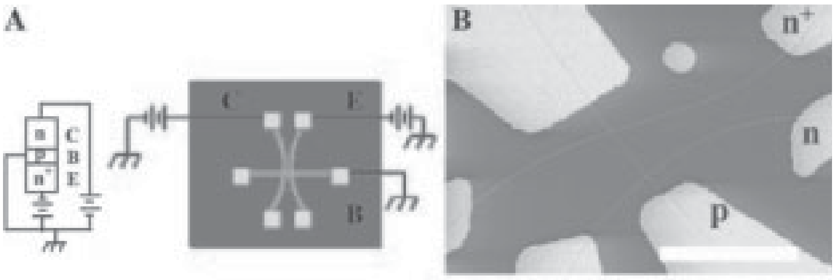

Figure 2.1: *(A) Schematic image and (B) field emission SEM image of a* n^+*-p-n Si nanowire bipolar transistor. The scale bar is 5 µm. Images taken from [37].*

are defined by employing lithographic techniques. Using such a set-up (and additionally passivating the surface of the nanowire), Chang *et al.* realized a ZnO FET showing an on/off ratio in the order of 10^4 with a mobility of 3118 cm^2/Vs [38].

Besides plain FETs, also logic devices based on single nanowires were already presented. Huang *et al.* formed nanowire blocks by assembling the nanowires from a solution. By crossing n-type gallium nitride (GaN) and p-type Si nanowires, they fabricated OR, AND and NOR gates and showed that nanowire computation is possible [5].

Memory arrays were realized by crossing Si/a-Si core-shell structured nanowires with Ag nanowires. Both the Si core and the Ag nanowires act as electrodes, while the a-Si shell functions as storage medium [39]. Electrical measurements showed that the devices could be switched between on (high resistance) and off (low resistance) states within defined threshold voltages at ratios $\geq 10^4$. The devices exhibited a memory retention time of at least 2 weeks.

2.3.2 Optoelectronic devices

Light emitting devices rely on the recombination of electrons and holes and therefore require p- and n-type material. By the method described above, Duan *et al.* formed p-n junctions by crossing n- and p-type indium phosphide (InP) nanowires [36]. In forward bias, a large current was detected, while in reverse bias only a small current was flowing.

Electroluminescence (EL) measurements like shown in Fig. 2.2 reveal that light originates from the p-n nanojunction. The maximum intensity was detected at 820 nm which is blue shifted with respect to the EL signal expected from bulk InP (925 nm). Additionally, it was found that the blue shift increases with decreasing nanowire diameter which was attributed to quantum confinement effects [36].

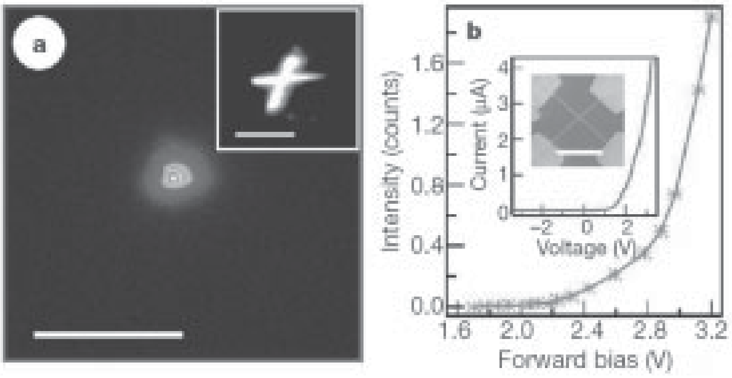

Figure 2.2: *(a) Electroluminescence (EL) from crossed p-/n-type InP nanowires in forward bias. The inset shows the corresponding photoluminescence (PL) image. (b) Intensity of the EL signal versus voltage. The inset depicts the related I-Vcharacteristic of the p-n junction and a FE-SEM image of the device. Scale bars in all figures are 5 μm. Images taken from [36].*

Pursuing a different concept, p-n junctions were formed by GaN nanowires having an n-type core that is surrounded by a p-type outer shell. Additionally, an intrinsic InGaN layer was deposited between the inner core and the outer shell. EL measurements revealed that in forward bias, the nanowires showed strong luminescence and besides this, by varying the In/Ga ratio, the wavelength of the emitted light could be tuned [6].

Nadarajah *et al.* employed an array of nanowires to obtain a LED structure. Undoped and Al-doped ZnO nanowires were grown by electrodeposition on a flexible transparent substrate covered with a conductive indium tin oxide (ITO) layer which served as back contact. The nanowires were embedded in a p-type polymer. For the undoped ZnO sample the EL spectra showed broad emission ranging from 500 nm to nearly 1100 nm, whereas for the sample employing Al-doped and annealed nanowires, UV emission at 390 nm was detected [40].

The results described above show that nanowires can act as light emitters. By using diverse materials or nanowires of different diameters, it is therefore possible to build LEDs on a nanometer scale covering the entire range of the UV, visible and near-infrared spectra.
In optoelectronic circuits, nanostructures might also be used as light detectors. Due to their photoconducting properties and their large surface to volume ratio, they are highly sensitive to exposure to light with energy above the band gap energy. The illumination-induced increase in conductivity may even exceed five orders of magnitude [41, 42] and the devices can be reversibly switched between on (low resistance) and off (high resistance)

states, analogous to the principle of gating effects in a FET. Furthermore, it is found that for some materials, like for example ZnO, the photoconductive gain and the photocurrent decay times strongly depend on ambient conditions [42], a finding that can be exploited to modify the design of the photodetectors.

Nanostructures are not only ideal candidates for miniaturized light sources like LEDs, but also for lasers, since they can be easily applied as resonators. Using bottom-up structured ZnO nanowire arrays grown on sapphire, Huang *et al.* fabricated nanolasers without the need of any additional cleavage or etching steps [43]. The authors took advantage of the fact that both ends of the nanowires are flat and capable to serve as mirrors. When optically pumped with an energy above the threshold energy, stimulated emission of the as-grown nanowires was detected. But not only in arrays, also in single isolated GaN nanowires optically pumped laser emission was detected [44].

2.3.3 Sensors

As already mentioned, nanostructures are ideal components in sensing applications due to their extremely large surface. In general, electron donors or acceptor molecules adsorb/desorb on the surface leading to an increase/decrease in band banding effects due to Fermi level pinning on surface states. The width of the space charge region modulates, which also implies a change in conductivity. By means of electrical measurements it is possible to already notice smallest changes in ambient gas conditions [45–47] or to detect biomolecules at very low concentrations [48].

2.3.4 Power generators

Nanoparticles already find application in dye-sensitized solar cells [49] for some years and the achieved efficiencies may even exceed 10 %. Today, also solar cells based on nanowire arrays are under investigation [50].

In contrast to the conventional energy extraction by converting the incident photon energy into electrical energy, Qin *et al.* presented an approach that exploits the piezoelectric features of ZnO nanowires. The nanowires were grown radially around Kevlar textile fibers. By entangling two fibers and brushing the nanowires grown on them in opposite directions, the mechanical energy is converted into electricity [7]. On the basis of their data, the authors estimated to achieve an optimum output power density from the coated textile fabrics of 20-80 mW/m^2.

This short overview shows that nanostructures have already been successfully incorporated into various device structures; however, most advanced applications are still in the laboratory stage. Today, a lot of research is still performed on CNTs as well as on Si nanowires that are investigated regarding their compatibility into already existing Si based devices. In addition, much effort has been put in the growth, characterization and device applicability of nanostructures based on compound semiconductors due to the possibility of band gap engineering. Most focus was on semiconductors with a direct band gap, like the metal oxide ZnO.

The following chapter presents the basic properties of the semiconductor as well as ZnO based nanostructures and their synthesis methods.

Chapter 3

The semiconductor ZnO

ZnO is a highly complex system having unique material properties. Research on ZnO, especially on bulk ZnO, has been going on for decades and the growth mechanisms as well as the optical and transport properties have already been extensively studied. However, due to lack of the technical possibilities in the past, research on ZnO nanostructures has just commenced to emerge within the last few years.

This section presents the basic properties of the ZnO crystal and the electronic band structure. Furthermore, defect states and the electronic properties of ZnO are being discussed.

3.1 Crystal properties

ZnO is a II-VI binary compound semiconductor that under ambient conditions usually forms in the hexagonal wurtzite structure. In this configuration every Zn^{2+}-cation is tetrahedrally coordinated to four O^{2-}-anions and vice versa. Each atomic layer is solely occupied by one species of atoms. The alternating stacking of the layers leads to a polar symmetry along the c-axis causing piezoelectric features of the ZnO crystals. Figure 3.1 shows a hexagonal unit cell characterized by the lattice constants a and c ($a \approx 3.250$ Å, $c \approx 5.206$ Å, the c/a ratio is about $c/a \approx 1.6$). ZnO has a density of 5.606 g/cm^3 [51].

Under specific conditions, ZnO also crystallizes in zincblende and rocksalt structures, but they are by far less common. Zincblende ZnO can only be stabilized when grown on cubic substrates, while rocksalt ZnO only forms under very high pressures.

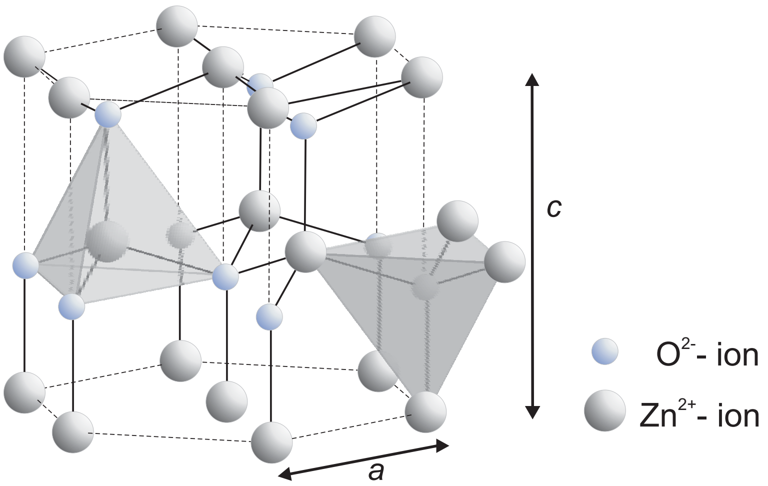

Figure 3.1: *Hexagonal wurtzite crystal structure.*

3.2 Band structure

Without adding any additional elements, ZnO has a direct band gap of E_g = 3.37 eV at room temperature, but the band gap can be tuned. Mostly Cd or Mg ions are used to substitute Zn atoms. Cd incorporation leads to a reduction of the band gap of even below 3 eV while the integration of Mg into the ZnO matrix increases the band gap (up to 4 eV) [52].

The electronic band structure of ZnO has already been calculated by various research groups [53, 54]. The energetically lowest conduction band corresponds to the empty Zn 4*s* levels while the uppermost valence band arises due to the occupied O 2*p* orbitals . In wurtzite ZnO, the crystal field and spin orbit interaction cause the valence band to split into three subbands referred to as A, B and C, respectively. While the energy splitting between B and C is comparably large ($\Delta E_{BC} \approx$ 43.7 meV, [55]), the energy difference between A and B was determined to only $\Delta E_{AB} \approx$ 4.9 meV [55], $\Delta E_{AB} \approx$ 9.5 meV [56] or $\Delta E_{AB} \approx$ 12 meV [57]. The splitting of the valence band is illustrated schematically in Figure 3.2.

3.3 Electrical and optical properties

Also in nominally undoped crystals, ZnO still exhibits intrinsic n-type conductivity. Even though it is difficult to generally quantify the electrical properties of ZnO, since they strongly depend on the crystal quality and may therefore vary significantly, undoped samples usually exhibit charge carrier concentrations between 10^{15} cm^{-3} and 10^{18} cm^{-3}.

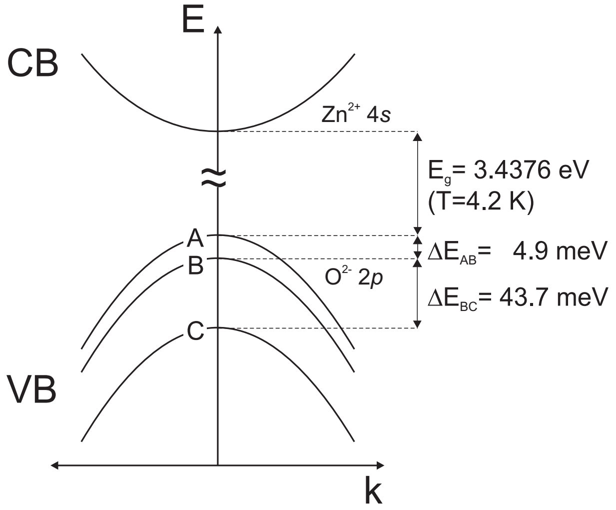

Figure 3.2: *Band structure of wurtzite ZnO and the splitting of the valence band into three subbands in the centre of the Brillouin zone. Values of the energy splitting taken from [55].*

In intentionally doped n-type layers, concentrations of up to 10^{20} cm^{-3} have been realized using excess Zn or by H-, Al-, Ga- or In-doping.
P-type doping of ZnO is still a problem. Whereas some claim to have achieved p-type conduction with concentrations of up to 10^{19} cm^{-3} [58], the results are still questionable particularly concerning the stability and the reproducibility.

It has long been commonly assumed that the n-type conductivity of ZnO is caused by excess Zn (either zinc interstitials (Zn_i) or oxygen vacancies (V_O)), acting as donors [59–61] or to hydrogen present in the crystal [62–64]. The defect levels are located about 10 - 60 meV below the conduction band and are therefore mostly ionized at room temperature. However, it has not yet been definitely clarified what causes the n-type conductivity. Recently, in contrast to the observations described above, Janotti and van de Walle claimed that native point defects are unlikely to be the cause of unintentional doping and that the majority of the results can be explained by the incorporation of residual hydrogen during growth [65].

Electron mobilities of ZnO films are mostly derived from temperature dependent Hall measurements. At low temperatures, values of up to 5000 cm^2/Vs were reported, while at 300 K, the highest mobilities range between 200 cm^2/Vs and nearly 500 cm^2/Vs [66, 67].

3.4 ZnO based nanostructures

Recently, ZnO nanostructures have been intensively investigated due to their outstanding physical properties and their anticipated performance in electronics as well as in opto- and magneto-electronics. An advantage of nanostructures as opposed to layers is the high crystallinity due to the relaxed growth with low lattice mismatched forces. Furthermore, high carrier concentrations can be achieved and, in matters of the desired functionality regarding magneto- and spin-electronics, small dimensions are required in order to fully exploit the advantages of spin. The shape and the dimensions (typically ranging from 5 to 500 nm) of the nanostructures depend on the growth method and parameters used. Figure 3.3 displays a selection of them.

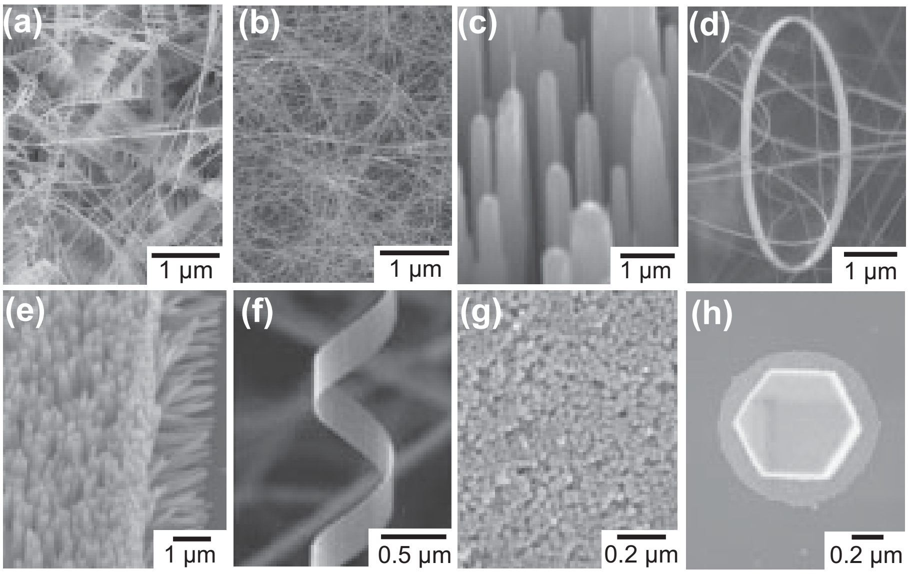

Figure 3.3: *Selection of ZnO nanostructures showing (a) nanocombs [68], (b) -wires [32], (c,e) pillars/-wires, (d) -rings [68], (f) -helices [69], (g) -particles (provided by Grillo Zinkoxid GmbH, Germany) and (h) platelets. - If no reference is given, samples were fabricated at the Institute of Semiconductor Technology.*

The nanostructures are usually of single crystalline quality, so when investigating electrical transport characteristics, scattering or band bending effects on grain boundaries do not have to be taken into account. Nevertheless, also in nanostructures a non-negligible defect density (mostly point defects) exists influencing not only the electrical but also the optical properties.

Lately, there has been considerable interest in the preparation of ZnO semiconducting nanostructures and nowadays all possible shapes of nanoparticles, -pillars, -wires, -belts and -helices exist. However, today special attention is given to ZnO nanowires and their device applicability. One major advantage as opposed to structures like nanobelts and

-helices is that they are grown in well-aligned, ordered and densely-packed nanowire arrays that are suitable for device applications.

3.4.1 Growth of ZnO based nanostructures

Self-organized ZnO nanowires are relatively easy to fabricate and today a number of growth techniques like molecular beam epitaxy, metal-organic vapor phase epitaxy, vapor phase transport, pulsed laser deposition, electrodeposition and aqueous chemical growth exist. While the vapor deposition techniques commonly require high temperatures, the wet chemical approaches only need temperatures of 60°C to 90°C. Therefore, all kinds of substrate materials (also low-cost polymer substrates) can be used. The position of the wires on the substrate can be precisely controlled and nanowire densities exceeding the pixel densities of commercially available displays are achievable. For hexagonal shaped ZnO nanowires, the highest growth rate is generally in (0001)-direction (c-axis).

Nanowires are usually grown either in a catalyst-free or in a catalyst-assisted process. The catalyst-assisted (often also referred to as vapor-liquid-solid (VLS)) approach relies on the use of catalysts to initiate and direct the growth. At first, metal catalyst clusters or films of a few nm thickness are deposited (for ZnO growth mostly Au is employed [70]) onto the substrate. The positions of the Au clusters determine the pattern of the resulting nanowires. By heating the substrate, the catalyst droplets melt. At the same time, the constituent elements of the semiconductor material are brought into gas phase and transported to the substrate by a carrier gas, where they preferentially condense at the catalyst droplets leading to the formation of a liquid alloy. When the alloy is supersaturated, crystallization at the liquid alloy/substrate interface takes place and nanowire growth starts. Growth will continue as long as the reactants are available and the catalyst droplets are in a liquid state. The epitaxial orientation and the aligned growth of the nanowires are determined by the lattice of the substrate while the dimensions of the catalyst droplets determine the wire diameter [68]. The resulting nanowires typically still have the solid catalyst particles at their tip and no catalyst material should be found in the semiconductor crystal. However, for Si nanowires it was found that during growth the Au catalyst wets the wire sidewalls and Au diffusion from smaller droplets to larger ones was observed [71]. Also the incorporation of small amounts of Au into the ZnO nanowires was reported [72] leading to unwanted doping effects.

In catalyst-free growth, ZnO nanowires are synthesized in a self-organized process (commonly referred to as vapor-solid (VS) growth) without introducing an extra catalyst.

The growth mechanism is similar to the VLS approach, but differs in the fact that one component of the gaseous supplied material might act as catalyst nuclei itself. Therefore, no contaminations from the incorporation of catalyst atoms should be present in nanowires grown in a catalyst-free approach.

3.4.2 Synthesis techniques involved in this work

The nanowires investigated in this thesis were either grown by vapor phase transport or aqueous chemical growth. This section presents the main principles of these growth methods.

Vapor phase transport

ZnO nanowires were grown in a home-made advanced horizontal vapor phase transport (VPT) system providing growth at temperatures from up to 1000°C and reactor pressures from 1 mbar to 1 bar. The nanowires were either grown by the use of a catalyst (Au droplets) on (001) Si substrates or in a catalyst-free process employing (11-20) Al_2O_3, 4H- and 6H-SiC substrates. Zn (6N) served as Zn source and O_2 (4.5N) and N_2 (5N) as reactant and carrier gas, respectively. The vaporized Zn was transported by the carrier gas while O_2 was channeled to the substrate by a separate line [73]. While for catalyst-assisted growth temperatures of up to 1000°C were required, for nanowires fabricated without the use of a wetting layer the temperatures ranged between 650°C and 800°C. Growth on ITO covered glass took place at 500°C.

Depending on growth parameters and substrates used, the nanowires have diameters ranging from a few tens of nm to nearly 1 µm. For the catalyst-free grown nanowires lengths of up to 12 µm were observed while for the samples grown with the use of a catalyst, lengths of up to several tens of µm could be reached. Figure 3.4 displays a selection of nanowires grown by VPT.

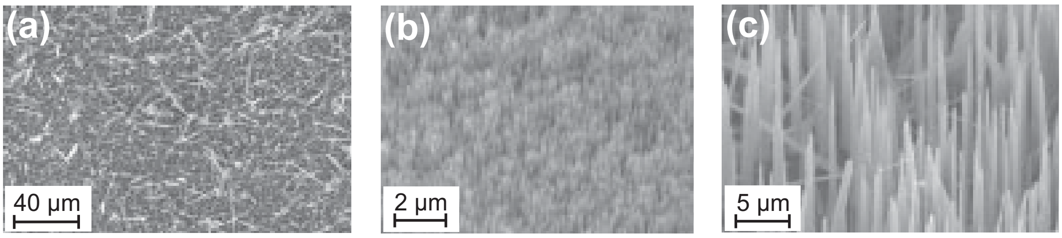

Figure 3.4: *Selection of ZnO nanowires grown by VPT with the use of a catalyst on (a) (100) Si and in a catalyst-free process on (b) Al_2O_3 and (c) 6H-SiC.*

The nanowires are of high crystalline quality with a low number of defects as transmission electron microscopy (TEM) and PL investigations reveal [74, 75]. Concerning the electrical transport properties, high purity crystals with a low number of defects exhibit low charge carrier concentrations and therefore high resistances.

All VPT grown nanowires investigated in this work were grown by A. C. Mofor and A. Behrends. A detailed description of the growth procedure and the structural and optical properties can be found in [76].

Aqueous chemical growth

Additionally, vertically aligned ZnO nanowires were grown by an aqueous chemical growth (ACG) process either on (100) Si substrates or on ITO covered glass. The solution contained equimolar amounts of analytic grade hexamethylenetetramine ($C_6H_{12}N_4$) and reagent grade zinc nitrate hydrate ($Zn(NO_3)_2{\cdot}6H_2O$) in deionised water. The average nanowire diameter and length are controllable by modulating the reactant concentration in the solution and the growth time. Concentrations between 0.01 and 0.05 mol l^{-1} were applied and typical reaction times were 3 h at temperatures of 90°C. Prior to the actual chemical growth, thin layers of ZnO seed crystals serving as catalysts were deposited onto the substrates.

The resulting nanowires grow densely packed over large arrays and show a good vertical alignment which is also confirmed by x-ray diffraction [77]. The wires are of conical shape with lengths of 1 - 2 µm and diameters between 100 and 200 nm. Figure 3.5 shows some nanowire arrays grown by ACG on Si and on ITO glass.

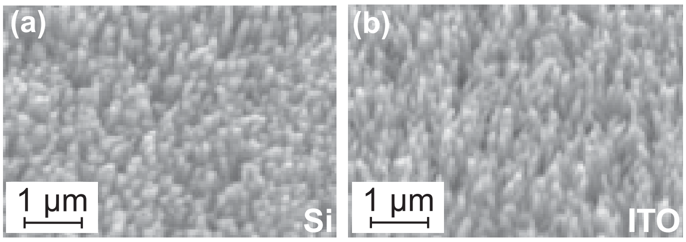

Figure 3.5: *Arrays of ZnO nanowires grown by ACG on (a) (100) Si and on (b) ITO covered glass. Both samples were grown at* 90° *C for 3 h at a concentration of 0.05 mol* l^{-1}.

TEM analysis and X-ray diffraction (XRD) measurements reveal that the nanowires are single crystalline and dislocation-free. However, in contrast to the nanowires grown by VPT, PL measurements show broad emission within the visible range. This is attributed to a high number of point defects. Furthermore, the large width of the near band edge luminescence ($\approx$ 120 meV at 300 K) is regarded as indication for high donor densities. Due to the higher defect densities and possibly larger amounts of H atoms present in the crystal (growth in aqueous solution), an increased conductivity as compared to the VPT grown samples is expected. While this might be disadvantageous concerning applications in sensorics, high carrier concentrations might be preferred regarding the realization of diluted magnetic semiconductors.

All ACG grown nanowires investigated in this work were grown by B. Postels. A detailed description of the growth procedure and the structural and optical properties can be found in [78].

Chapter 4

Electrical properties of ZnO nanosystems

Electrical transport measurements on nanostructures are not only a challenging task because of difficulties and the technical effort required for structuring the electrodes, but the intrinsic resistances of the nanostructures are also influenced by numerous factors like crystalline quality, defect density, surface morphology, surface states etc. Furthermore, due to their large surface to volume ratio, they are especially sensible to changes in ambient conditions.

This chapter presents the results of the investigations of the electrical properties of single ZnO nanowires and nanopowders. It starts with a short outline of the parameters charge carrier concentration and mobility; how they affect the resistivity of the nanostructures and how they depend on crystal properties like crystallinity and defect density. Since nanoscale contacts play an important role when electrical measurements are performed, the influence of Schottky barriers at the metal-semiconductor interfaces and the transport mechanisms over the barriers are discussed. Subsequently, the results of the current-voltage (I-V) measurements of single VPT grown nanowires are presented, as well as investigations concerning their photoconductive response. A model describing the observed effects is introduced. Additionally, it is shown how the deduced resistivity values fit to the published data of other groups.

In the second last section, the results of the electrical property measurements of ACG grown nanowires contacted by various techniques are presented. Studies concerning the influence of atmospheric conditions and humidity on the conductivity of ZnO nanpowders complete this chapter.

4.1 Conductivity and resistivity

The electrical conductivity σ gives a measure of a material's property to conduct an electric current. It is defined by the ratio of the resulting current density J to an applied electric field E:

$$\sigma(T) = \frac{J(T)}{E}. \tag{4.1}$$

The conductivity depends on the electron/hole concentrations $n_{n/h}(T)$ and the mobilities $\mu_{n/h}$ by

$$\sigma(T) = q(n_n(T)\mu_n(T) + n_h(T)\mu_h(T)), \tag{4.2}$$

where q denotes the elementary charge. Most reports give values for the resistivity instead of the conductivity, where the resistivity ρ is simply defined as the reciprocal of the conductivity

$$\rho = \frac{1}{\sigma} = \frac{1}{q(n_n(T)\mu_n(T) + n_h(T)\mu_h(T))}. \tag{4.3}$$

All electrical measurements presented in this work were performed at room temperature, so for simplification purposes, in the following, the temperature dependences of the carrier concentrations and mobilities will not be explicitly stated ($n(T) \rightarrow n$, $\mu(T) \rightarrow \mu$). Furthermore, in n-type ZnO, the number of holes contributing to the conductivity is sufficiently small ($n_h \rightarrow 0$), which means that for future considerations and evaluations they will not be taken into account. Therefore, the electron density n_n solely determines the carrier concentration.

The defect levels in ZnO are located about 10 - 60 meV below the conduction band, hence the defects act as shallow donors. The vast majority of them are singly ionized at room temperature as the calculation shown in Appendix A reveals. For simplification purposes, it is therefore assumed that the charge carrier density equals the donor density N_d:

$$n \approx n_n \approx N_d. \tag{4.4}$$

It is generally believed that point defects act as shallow donors and cause the n-type conductivity. So according to Eq. (4.3), the higher the defect density in the crystal, the lower the resistivity of the nanowire.

Another important parameter in carrier transport investigations is the mobility μ_n that describes to which extend the drift velocity v_d of the electrons is influenced by the applied electric field E:

$$v_d = -\mu_n E \tag{4.5}$$

where

$$\mu_n = \frac{q\tau}{m_n^*}. \tag{4.6}$$

m_n^* represents the effective mass and τ the average time between collisions, the so called mean free time. The mobility is therefore directly affected by various scattering mechanisms like scattering on phonon and impurity atoms. With increasing temperature, lattice vibrations and phonon scattering increase, leading to a decrease in mobility. Hence a significant temperature increase of the nanowire caused by the electric current passing through the nanowire should be avoided during measurement.

While in bulk crystals, scattering on phonons and impurity atoms are the most important mechanisms, in nanostructures also scattering on surfaces plays a significant role. This might lead to a reduced mobility in nanostructures compared to the mobilities measured in bulk crystals. Also the surface morphology of the nanowires has to be taken into account. Although they are mostly of single crystalline quality, they sometimes exhibit a considerably rough surface. In some cases, crystalline imperfections in the outermost layer are observed that may lead to a further reduction of the mobility.
Summarized, among other factors, defect densities and surface properties severely influence the resistivity of nanowires.

For layers, properties like resistivity, charge carrier concentration and mobility can be directly determined by Hall measurements. Unfortunately, this approach is not suitable to characterize the electrical properties of nanowires. In general, current-voltage measurements serve to determine the resistance R_{NW} of the nanowire which is linked to the resistivity by

$$R_{NW} = \rho\frac{l}{A}, \tag{4.7}$$

where l denotes the distance between the electrodes and A is the cross-section of the nanowire. The nanowires are predominantly measured in 2-point probe geometry, therefore the measured resistance R_{total} is the sum of the resistance of the nanowire R_{NW} and the contact resistances R_C:

$$R_{total} = R_{NW} + R_C. \tag{4.8}$$

Especially nanoscale contacts might critically influence I-V measurements. In the following paragraph, the formations of potential barriers at the metal-semiconductor interfaces as well as the transport mechanisms over the barriers are discussed.

4.2 Contact resistances and Schottky barriers

Electrical characterization of nanowires inevitably involves a metal-semiconductor-metal structure and in most cases the contacts are non-ohmic. The following sections describe the formation of Schottky barriers at the metal-semiconductor interface and how they influence the evaluation of the I-Vmeasurements.

4.2.1 Energy band diagrams

In this work, the nanowires were measured in 2-point-probe geometry as schematically shown in Fig. 4.1(a). Assuming that the n-type ZnO and the metal electrodes are in intimate contact (no interfacial layer), potential barriers are formed at the interfaces that are commonly referred to as Schottky barriers. Figure 4.1(b) displays the energy band diagram in thermal equilibrium and the corresponding equivalent circuit. It consists of two contrarily biased Schottky diodes and a resistor representing the resistance of the nanowire. When a voltage is applied, the band diagram shifts, whereby one Schottky diode will be in reverse and the second one in forward bias. Figure 4.1(c) shows a simplified image when a negative voltage is applied to the left electrode: the left Schottky diode will be in reverse bias while the right one will be in forward bias. Therefore, independent of the polarity of the applied voltage, in either case, one of the diodes will be in reverse bias.

Both metal electrodes form depletion contacts on the n-type semiconductor as shown in Figure 4.1(b). While the depletion layer in the metal is negligibly small, the width w of the depletion region formed in the semiconductor is determined by

$$w = \sqrt{\frac{2\epsilon\epsilon_0(V - V_{bi})}{qN_d}}, \tag{4.9}$$

where V denotes the applied reverse voltage, V_{bi} the build-in voltage and $\epsilon\epsilon_0$ the permittivity. The equation was obtained by assuming that the charge density ρ_c is equal to the density in the bulk of the semiconductor ($\rho_c \approx qN_d$) for $x < w$ whereas it falls abruptly to almost 0 for $x > w$, where x represents the distance from the metal-semiconductor interface [79].

It should be pointed out that in most metal-semiconductor-metal structures the ideal situation displayed in Fig. 4.1(b) is never attained. Usually, there is a thin layer of oxide (thickness between 1 - 2 nm) on the semiconductor surface [79]. Even though ZnO is a oxidation resistant material, there are also some results indicating the existence of such a metal-insulator-semiconductor structure as shown in Chap. 4.5.2.

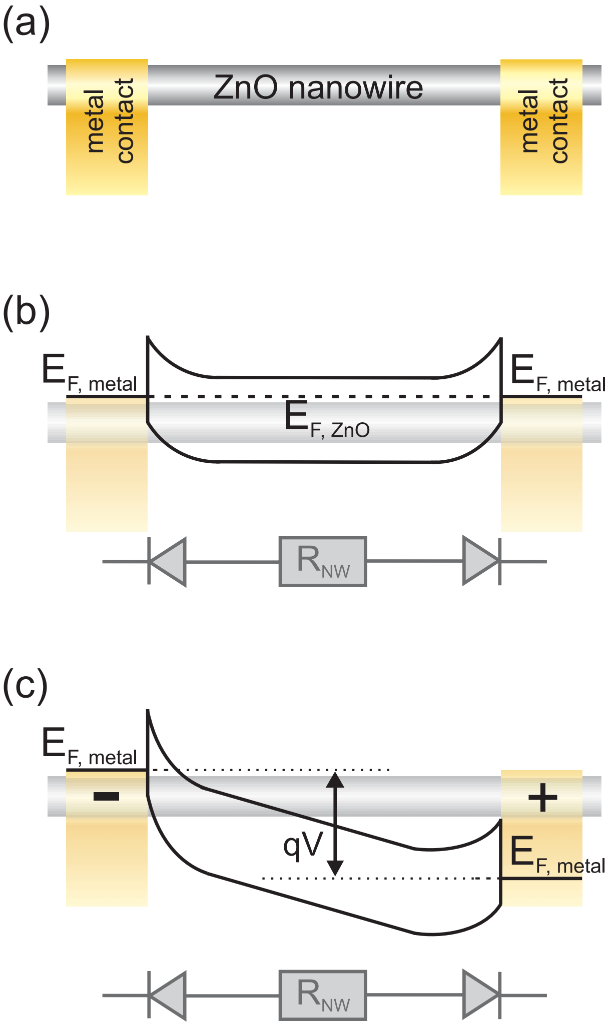

Figure 4.1: *(a) Schematic set-up of a ZnO nanowire contacted in 2-point-probe geometry. Energy band diagram of the metal-semiconductor-metal structure (b) in thermal equilibrium and (c) with an applied bias voltage.*

4.2.2 Transport mechanisms

Several transport mechanisms over the Schottky barrier exist as Fig. 4.2 shows.

For lowly-doped nanowires ($N_d \leq 10^{17}$ cm^{-3}, solid line in Fig. 4.2) thermionic emission is the dominating process, where the electrons gain sufficient thermal energy to overcome the barrier. In the intermediate doping range (10^{17} cm^{-3} $\leq N_d \leq 10^{19}$ cm^{-3}, dashed line), electrons are thermally excited to an energy level where the barrier width is sufficiently narrow for tunneling (thermionic field emission). For high concentrations ($N_d \geq 10^{19}$ cm^{-3}, dotted line), the barrier is very narrow and the electrons can tunnel directly into the metal. This mechanism is known as field emission [80], the higher the donor density, the higher the tunneling probability.

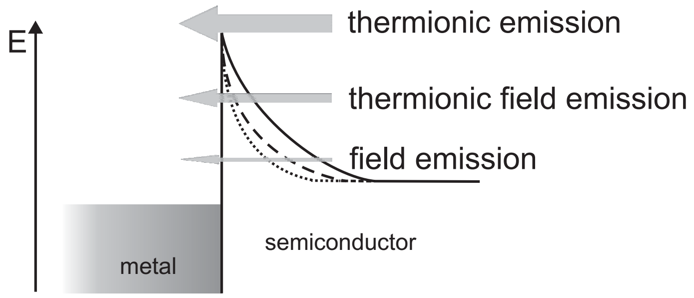

Figure 4.2: *Transport mechanism over the Schottky barrier.*

ZnO nanowires typically exhibit donor concentrations below 10^{19} cm^{-3}, therefore thermionic and thermionic field emission will be the main mechanisms. Defect states at the interface and defects within the band gap additionally enhance the tunneling chances of the electrons through the barrier.

4.2.3 Current-voltage measurements

Current-voltage measurements are a common technique for electrical characterization of nanowires. The correlation between bias voltage V and current density J for Schottky diodes is given by

$$J = J_S \left(exp\left(\frac{qV}{n_{id}kT} \right) - 1 \right), \tag{4.10}$$

where J_S denotes the saturation current density and n_{id} the ideality factor. All other parameters have their typical meaning and can be found in Appendix C.

The ideality factor gives a measure of the dominating recombination mechanism in the diode. For an ideal diode, this factor yields a value of 1 and only recombination of charge carriers over defect states in the neutral region takes place. Shockley-Read-Hall recombination occurs via defects in the space charge region. In this case, the value of n_{id} ranges between 1 and 2. For $n_{id} > 2$, recombination is influenced by tunneling effects. In thermionic field emission, the saturation current density J_S is

$$J_S = A^* T^2 exp\left(-\frac{q\phi_B}{kT} \right), \tag{4.11}$$

where in case of thermionic field emission, J_S is given by

$$J_S = A^* T^2 \left(\frac{\pi E_{00}}{k^2 T^2} \right)^{1/2} \left[qV + \frac{\phi_B}{cosh^2(E_{00}/kT)} \right]^{1/2} exp\left(\frac{-q\phi_B}{n_{id}kT} \right). \tag{4.12}$$

In either case, A^* symbolizes the Richardson-constant and ϕ_B the Schottky barrier height. In case of thermionic field emission, the factor E_{00} represents the characteristic tunneling energy [81] that depends on the donor concentration and effective mass m^*.

A disadvantage of the thermionic emission theory is that it underestimates the contribution of the reverse current [82] which may be in the order of several tens of nA. In microelectronic devices, this current flow produced by the tunneling of the electrons is negligibly small. However, for metal-nanowire-metal structures like investigated in this work, the measured current is almost comparable to the reverse current in the Schottky diode. This means that the current produced by tunneling of the electrons significantly influences electrical transport studies of nanoscale devices. At large reverse bias, it may even become the dominating mechanism [83].

4.3 Experimental set-up

Figure 4.3 shows a photograph of the computer-controlled home made experimental set-up used for electrical characterization. The set-up consists of multiple components, with the main module being the gas chamber where the sample is located. The sample is contacted by manipulator tips, as shown in the inset. Additionally, the interior is equipped with an UV LED, a humidity and a pressure sensor. Besides air and vacuum (a pump is installed that can bring the air pressure down to about 0.1 mbar), the chamber can be vented with argon, nitrogen, oxygen and hydrogen. Gas flow is controlled by four mass flow controllers. The relative humidity can be changed by using a temperature regulated water bubbler.

Current-voltage measurements were performed by using a Keithley 6487 picoamperemeter with an integrated voltage source, while an Agilent E3631 A served as power supply for the UV LED.

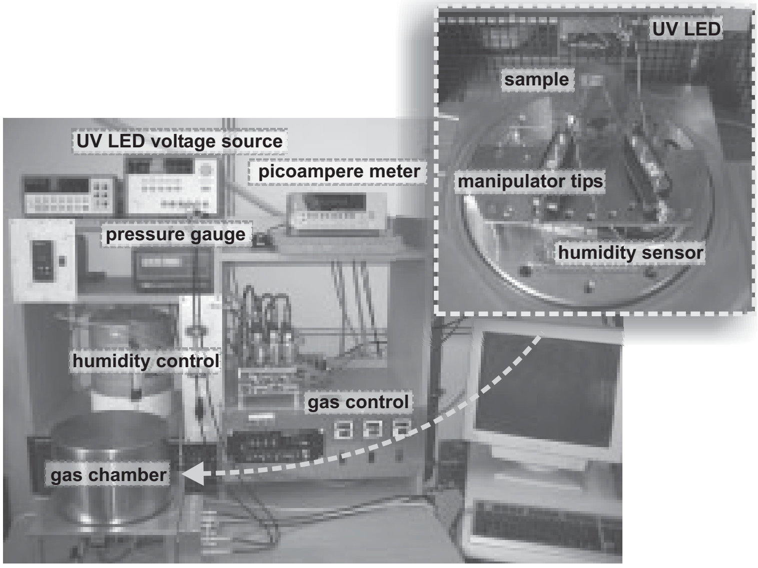

Figure 4.3: *Home made experimental set-up for electrical characterization. Besides control of the pressure and gas composition, the humidity in the gas chamber is also adjustable.*

4.4 Determination of contact material

Before contacting single nanowires or ensembles of nanowires, experiments on ZnO thin films were performed in order to determine the most suitable metal to form ohmic contacts. The samples were grown by molecular beam epitaxy (MBE) on sapphire [84] (samples provided by A. El-Shaer, Insitute of Semiconductor Technology) and the contact materials were thermally evaporated.

Figure 4.4(a) displays the I-Vcharacteristics of the ZnO films contacted by different electrode materials. Ti and Ag seem to form better contacts with lower contact resistances than Au, Ni and Pd. Since some Ag contacts showed slightly non-linear I-Vcurves, Ti was chosen as contact material for the following investigations.

To get an estimate of the contact resistance of Ti on ZnO, the films were structured into stripes by employing photolithography techniques and resistance measurements were performed according to the transmission line method. Figure 4.4(b) shows the determined total resistance over distance of the electrodes; the upper inset displays a schematic image of the sample structure. In order to prevent oxidation of the Ti contacts, an additional layer of Au was evaporated onto the electrodes.

The contact resistance derived from the linear fit (dashed gray line in Fig. 4.4(b)) is about 50 Ω resulting in a contact resistivity of approximately $4 \cdot 10^{-4}$ Ωcm of the as-deposited Ti/Au contacts on ZnO thin films.

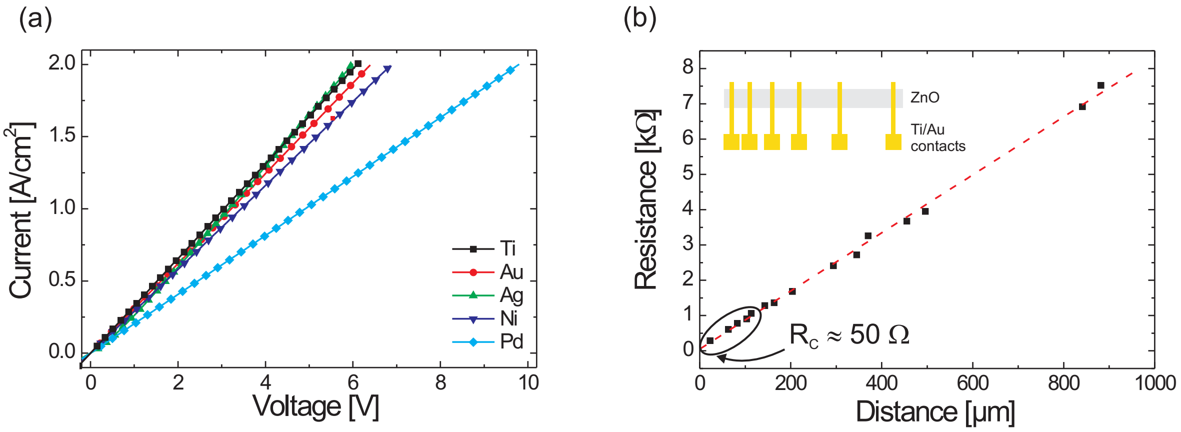

Figure 4.4: *(a) I-Vmeasurements of ZnO layers using different electrode materials. (b) Determination of contact resistance of Ti/Au contacts on ZnO layers according to the transmission line method.*

4.5 Electrical properties of VPT grown nanowires

In first attempts to contact single isolated nanowires, prestructured Ti/Au (Ti as adhesive layer, Au as contact material) conductive paths served as electrodes. The VPT grown nanowires were first dispersed in ethanol and then arbitrarily spread onto the substrate. Even though some nanowires were electrically contacted and *I-V*measurement could be performed, this random approach had some major disadvantageous. Besides the lack of position control and the possible existence of ethanol contaminations between the electrodes and the nanowires, only larger sized wires could be measured using this approach. The reason for this was that the conductive paths were structured employing photolithographic techniques and the distance between the electrodes was at least 5 µm. So in order to be able to also contact smaller sized nanowires, in the following part of the study, the structuring of the conducting paths was performed by employing e-beam lithography which was carried out by T. Weimann and P. Hinze at the Physikalisch-Technische Bundesanstalt (PTB) in Braunschweig.

4.5.1 Contacting by employing e-beam lithography

In order to contact single isolated nanowires, they were detached from the corresponding growth substrate (like shown in Fig. 4.5(a)) and dispersed in ethanol in an ultrasonic bath. A droplet of the dispersion was brought onto a Si substrate covered with a 300 nm insulating SiO_2 layer. To get rid of possible ethanol contaminations on the ZnO surface, the sample was thoroughly rinsed with deionized water.

Prior to deposition of the nanowires on the SiO_2/Si substrate, large arrays of markers were structured in a first lithography step together with global alignment markers for the e-beam tool in order to locate the position of the randomly spread nanowires. The first investigations were carried out with optical microscopes, after which SEM image acquisition was applied to determine the position of the nanowires on the substrate as shown in Fig. 4.5(b). The images were imported into a CAD system to be able to individually design the layouts of the electrodes for each nanowire.

A double layer structure of 960 k and 200 k polymethyl methacrylate (PMMA) of different thicknesses was used as photoresist which was developed in a solution of isopropylalcohol for 60 s. The contacts were patterned by e-beam lithography using a Leica EBPG 5000+ e-beam system in combination with lift-off techniques, while thermally evaporated Ti/Au (30 nm/260 nm) served as contact material. The maximum thickness of the electrodes was limited to 300 nm to ensure a proper lift-off process. Figure 4.5(c) shows a device processed in such a manner.

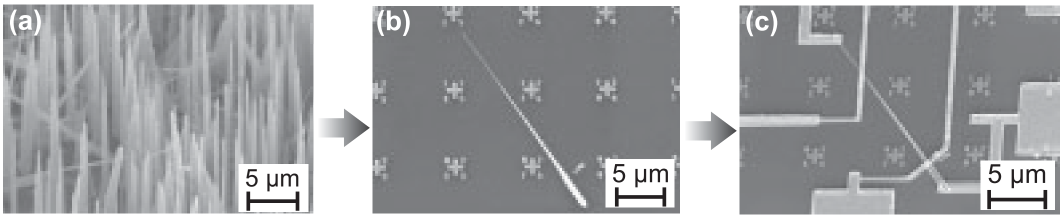

Figure 4.5: *Fabrication steps required to contact single nanowires by employing e-beam lithography techniques: (a) Detachment of nanowires from growth substrate, (b) determination of position of the randomly distributed nanowires by SEM, (c) patterning of electrodes by e-beam lithography and lift-off techniques. E-beam lithography was carried out by T. Weimann and P. Hinze at the PTB in Braunschweig.*

However, broken conductive paths were observed as shown in Fig. 4.6 when the contact material was merely evaporated in a planar geometry. Therefore, in order to prevent failure of the contacts, evaporation of the metals was subdivided into two steps: In the first step, evaporation of Ti/Au on the planar substrate was performed while in the second step, the substrate was inclined at an angle of about 45° during the evaporation process.

4.5.2 Typical *I*-*V* characteristics

The electrical transport properties of nanowires both grown in a catalyst-assisted as well as in a catalyst-free growth process were investigated. All *I*-*V* measurements were performed at room temperature and under standard air conditions (if this is not the case, it will be explicitly stated).

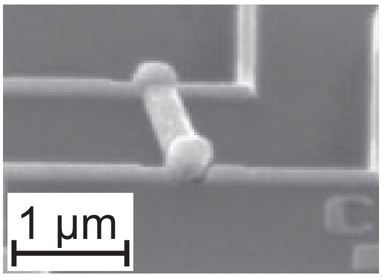

Figure 4.6: *SEM image of a nanowire with a broken conductive path.*

Figure 4.7(a) shows a SEM image of a contacted ZnO nanowire. The wire was grown with the use of an Au catalyst and is about 400 nm in diameter and 46 µm in length; therefore, several contacts could be applied. For the sake of clarity, the contacts are labeled from a to f. Figure 4.7(b) displays the corresponding I-Vcharacteristics, where one electrode was fixed (contact a) and the second electrode was varied (contacts b to f).

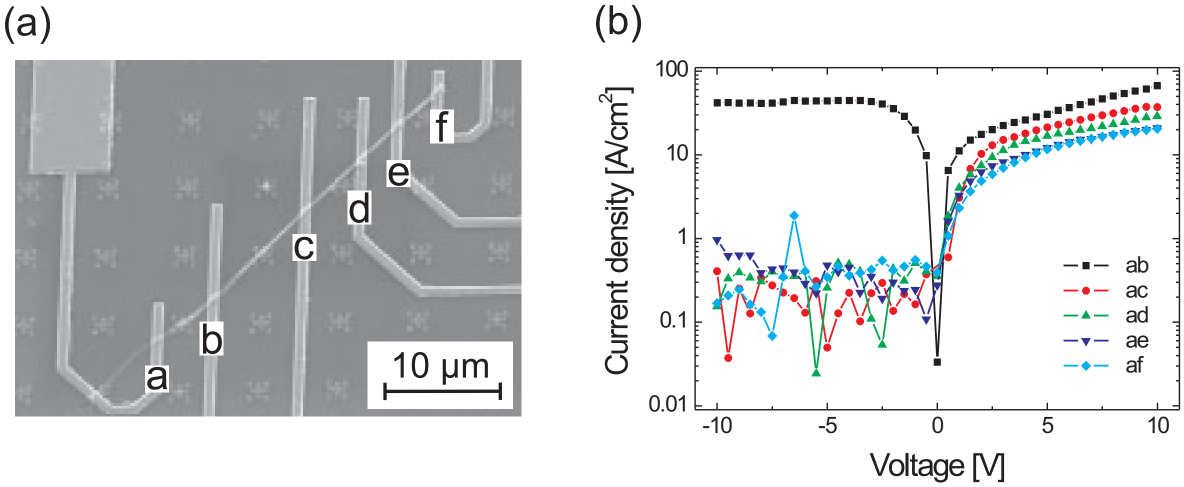

Figure 4.7: *(a) SEM image of a nanowire contacted by several electrodes labeled from a to f. (b) I-Vcharacteristics measured between contact a and contacts b,c,d,e,f.*

As already described in Chap. 4.4 and also confirmed by literature [85], Ti forms ohmic contacts to ZnO layers, even without any postdeposition treatment. However, in this case, under dark conditions and up to a bias voltage of ± 10 V, no current could be detected on a pA scale. Under light (ordinary laboratory fluorescent lamp), the I-Vcharacteristics shown in Fig. 4.7(b) display a strong rectifying behavior indicating Schottky contacts of different barrier heights. The current densities at positive bias voltages range between 10 A/cm^2 and 100 A/cm^2, while no reverse-bias breakdown

occurs up to -10 V. Asymmetric contacts of the same contact material have already been observed in other ZnO based nanodevices [86, 87].
Additionally, it is observed that the *I-V* characteristic measured between contact a and b saturates. This effect is likely due to limitation of the injected current in the metal-semiconductor-metal structure.

For further investigation of the quality of the Schottky contacts, the ideality factors and the barrier heights were deduced by fitting the linear section of the current in forward bias as shown by the gray dashed line added in Fig. 4.8. According to Eq. (4.10), from the slope of the fit, the corresponding value of the ideality factor was obtained, resulting in $n_{id} \approx 6$.

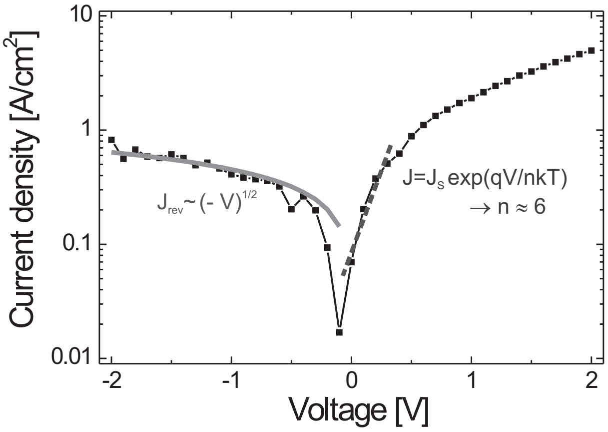

Figure 4.8: *I-V characteristic measured between contact a and e as shown in Fig. 4.7(a). Additionally displayed are fits of sections of the current in forward and reverse bias.*

Since it is extremely difficult to identify the linear section of the *I-V* data, the deduced ideality factor should only be regarded as a rough estimation. Nevertheless, the determined n_{id} strongly differs from unity, the value expected for an ideal diode, but fitting the characteristic at higher bias voltages would even lead to higher values.

Such a large deviation of the ideality factor may be attributed to the existence of an insulating interfacial layer between the Ti/Au electrode and the ZnO nanowire [88]. There are two possible scenarios explaining this metal-insulator-semiconductor (MIS) structure: Ti may either react during evaporation with residual oxygen in the evaporation chamber to form insulating TiO_x or it may compound with oxygen adsorbed on the ZnO surface.

At negative voltages, the reverse current of the I-Vcharacteristics can be fitted by $J_{rev} \propto \sqrt{-V}$ as shown by the gray line added in Fig. 4.8 indicating that the current flow in reverse bias is mainly due to charge carriers generated in the depletion region [89].

By extrapolating the fit to zero voltage one obtains a value for the saturation current density J_s which (according to Eq. (4.11)) depends on the barrier height ϕ_b. The Mott-Schottky theory predicts that ϕ_b is only determined by the potential difference of the Fermi level of the metal electrode ϕ_m and the electron affinity of the semiconductor χ_{sc} ($\phi_{b,theo} = \phi_m - \chi_{sc}$). The work function of Ti yields about 4.33 eV [90] and the electron affinity of ZnO is 4.35 eV [91], so Ti on ZnO should result in $\phi_{b,theo} \approx -0.02$ eV. But in contrast to the theoretical predictions, all deduced barrier heights $\phi_{b,exp}$ (calculated using $A^* = 32$ A/cm^{2}K^2 [92]) range between 0.3 eV and 0.5 eV, one order of magnitude higher than the theoretically expected value. However, this is not surprising regarding the possible existence of surface states or an insulating layer. Furthermore, it should be emphasized that the determined barrier heights of Schottky diodes exhibiting such high ideality factors are not reliable and the obtained values should be just regarded as figures of merit.

4.5.3 Investigation of the metal-semiconductor interface

In order to investigate the interface between the ZnO nanowires and the Au/Ti contact layers in more detail, the samples were analyzed after electrical characterization by transmission electron microscopy. For TEM image acquisition, the samples had to be placed onto an electron transparent substrate; therefore a 100 nm thin insulating Si_3N_4 membrane was fabricated by anisotropic etching of silicon in KOH. The resulting membranes were about 200 µm x 200 µm in size while the dimensions of the whole chip were chosen in such a way (3.8 mm x 3.8 mm) that they fitted into the sample holder of the TEM (Philips CM 200 FEG). Figure 4.9 shows a schematic view of such a device.

An energy dispersive X-ray (EDS) spectroscopy tool integrated in the TEM was used to study the chemical composition of the nanorods after electrical characterization. The nanowires were deposited onto the membrane using the same method as described in Chap. 4.5.1. A thin supporting substrate also increases the spatial resolution of the EDS analysis by decreasing the volume of the interaction between the electrons and the sample down to a range of 20 nm.

For some wires, a smearing of the electrodes at the nanowire interface after electrical characterization was observed, as shown in the SEM image in Fig. 4.10(a). The dotted

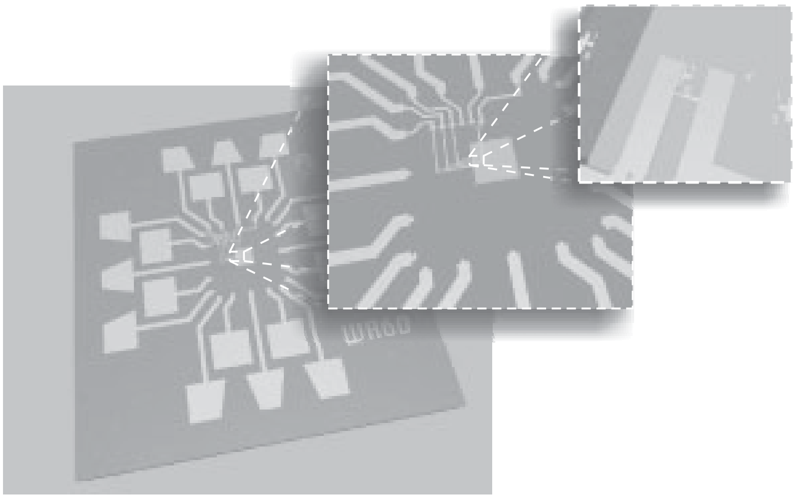

__Figure 4.9:__ Schematic view of a Si_3N_4 membrane carrying a contacted nanowire. Images provided by T. Weimann, PTB Braunschweig.

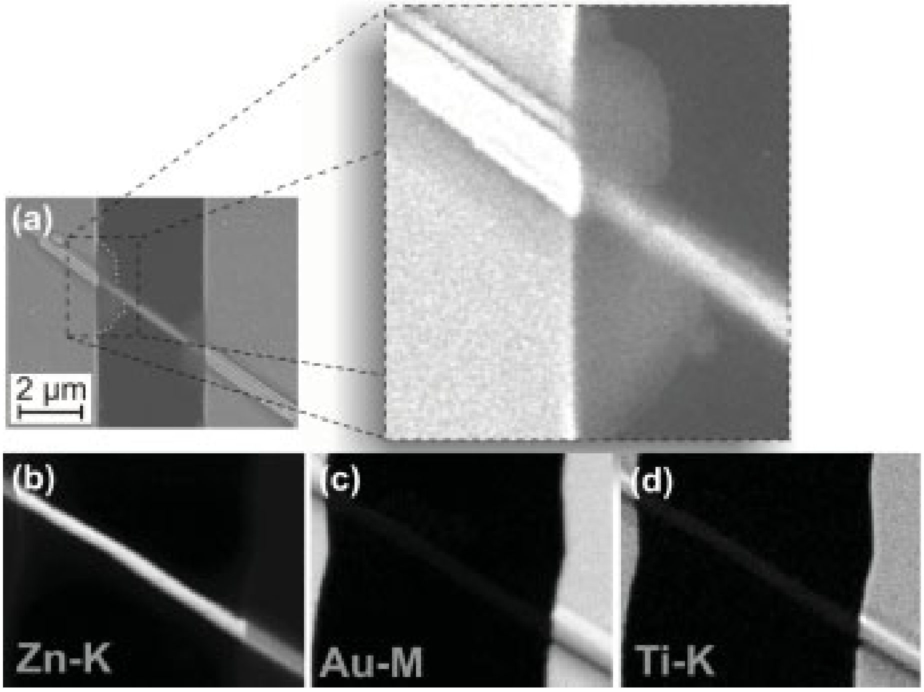

__Figure 4.10:__ (a) SEM image of a contacted ZnO nanowire after transport measurements; the dotted line defines the area of the smeared region and the inset displays a magnification of the nanowire/electrode interface. (b-d) Mapping results of the same wire (also taken after electrical characterization) show the spectra of the Zn-K, Au-M and Ti-K line measured by EDS in a TEM. Measurements performed by P. Hinze, PTB Braunschweig.

line defines the area and the inset shows a magnification of the smeared region. The corresponding results from the EDS map of the Zn-K, Au-M and Ti-K lines are presented in Fig. 4.10(b to d).

The Zn-K spectrum not only shows a clear Zn signal at the position of the nanowire but also at the position of the electrodes. This is due to the fact that the energies of the Au-L (not shown here) and the Zn-K signal lie in close proximity to each other, so that the contrast observed in the region of the conducting paths is caused by the insufficient spectral resolution of the detector.

However, the composition of the blurred region still remains unknown; neither a Zn nor a Au or Ti signal was observed. This is likely because of the small thickness of the blurred layer that was also invisible to TEM image aquisition. Nevertheless, the measurements give no indications that severe electromigration from the contact material into the ZnO occurs, since neither the Au-M nor the Ti-K results reveal an accumulation of Au/Ti in the nanowire itself (within the EDS detection limit).

4.5.4 Contact resistance, resistivity and charge carrier concentration

To obtain a rough estimate of the contact resistance of the VPT grown samples contacted by Ti/Au electrodes (all wires displayed nonlinear I-V curves), the total resistances R_{total} were deduced from the linear sections of the I-V curves in forward bias and plotted as function of length. The data are shown in Fig. 4.11.

The extrapolation of the linear fit to zero length roughly yields a contact resistance of about 85 MΩ which lies within the same range as the wire resistance. The upper inset again displays a SEM image of the device while the lower inset shows the I-V characteristic measured between contacts a and f, including the fit of the linear section in forward bias.

From the slope of the fit of the data, the resistance of the nanowire over length (R_{NW}/l) can be determined which yields a value of 12 MΩ/µm and results in a resistivity of $\rho \approx 130$ Ωcm (see Eq. (4.7)). Using Equation (4.3) one can estimate the charge carrier concentration n_n, yet the mobility still remains an unknown factor. Reported mobility values differ significantly ranging from 1 cm^2/Vs of as-grown MBE nanowires [93] to exceeding 1000 cm^2/Vs for in polyimide embedded nanowires [94]. The mobility μ is strongly influenced by the defect structure: any disturbance in the crystal lattice as well as the existence of surface states cause μ to decrease.

TEM images prove that the VPT grown nanowires are of single crystalline quality and photoluminescence spectra reveal a narrow linewidth of the nearband-edge emission

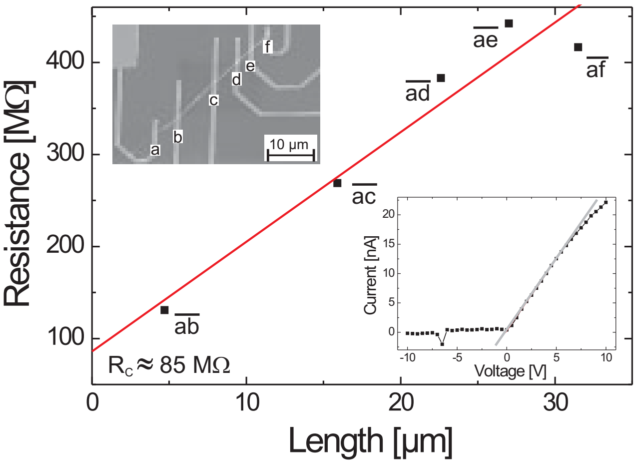

Figure 4.11: *Deduced total resistance over length of a single VPT grown ZnO nanowire. The upper inset shows a SEM image of the completed device while the lower inset depicts the I-Vcharacteristic measured between contacts a and f including the fit (grey solid line) of the linear section in forward bias.*

(≈ 0.7 meV). Also free exciton transitions appear hinting at high quality nanowires with low number of defects [76]. Therefore a mobility of 50 cm^2/Vs is assumed, which seems to be a reasonable value. If the number of holes in the n-type semiconductor is neglected, the obtained carrier concentration yields about 10^{15} cm^{-3}, which is quite low for ZnO. It is likely that, due to band bending effects resulting from Fermi level pinning at surface states, the actual cross-section A_{eff} for current transport differs from the geometrical cross section A_{geo} ($A_{eff} < A_{geo}$) that was used to determine the resistivity. This may lead to lower calculated carrier concentrations.

I-*V* data were also taken using other electrode combinations. Figure 4.12 depicts the obtained characteristics measured between electrodes a-b, e-f and a-e. As can be clearly seen, the current densities measured between contacts a-b differ significantly from the ones measured between contacts e-f, even though the distances between them are almost identical. However, in both measurements the current in forward and reverse bias are within the same order of magnitude, while the *I*-*V* curve obtained using contacts a-e shows a strong rectifying behavior. The current flow in forward bias exceeds the reverse current by more than one order of magnitude.

The differences in the obtained *I*-*V* data hint towards an inhomogeneous charge carrier concentration within the nanowire. This might be due to varying defect densities in the different growth stages. When growth starts, a higher defect density due to nucleation and lattice mismatch is likely while in regions further away from the substrate, a reduction in the number of defects is expected due to the relaxed growth with low lattice mismatched forces.

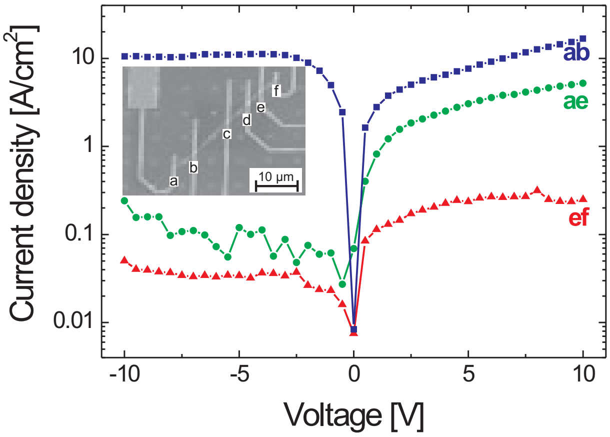

Figure 4.12: *I-Vcharacteristics measured between varying contact combinations (a-b, e-f, a-e) as shown in the SEM image inset.*

4.5.5 Photoresponse measurements

In order to investigate the photoconductive properties, ZnO nanowires were illuminated with monochromatic light using a set-up consisting of a 150 W Xe-lamp in combination with a monochromator (Jobin Yvon Hr 250) and a Si photodiode. Figure 4.13(a) shows a selection of characteristics measured under illumination with different wavelengths. Independent of the wavelength of the incident light, all I-Vcurves exhibit a rectifying behavior and saturate for voltages exceeding 2 V; however, the values of the saturation currents depend on the wavelength of the incident light. A significant increase in current due to photogenerated carriers occurs when the sample is illuminated with light at energy above the band gap energy, as can be seen in Fig. 4.13(a) in the characteristic measured at 340 nm. In addition, under illumination with light having an energy above the band gap energy, an increased current flow is also observed in the negative bias region. This is attributed to a decrease in the Schottky barrier width due to photogenerated holes in the depletion region of the reverse biased junction which are either trapped in the depletion region or in surface states, resulting in a positive charge. The positive charge leads to a reduction of the depletion width, additional electrons can tunnel through the barrier [95, 96] and an increased current flow is detected. When the energy of the incident light exceeds the band gap energy there is a strong increase in reverse current which is also shown in Fig. 4.13(b).

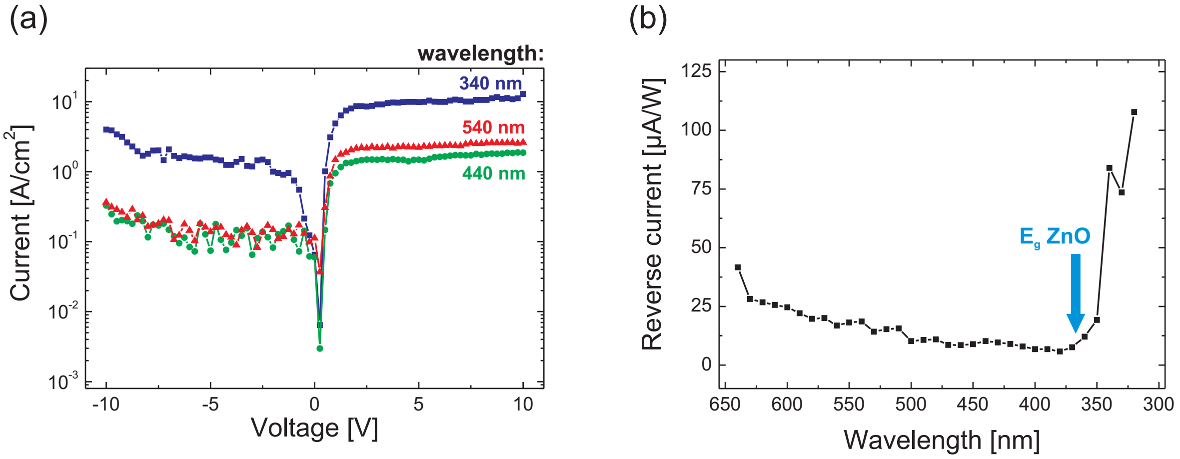

Figure 4.13: *(a) I-Vcharacteristics of photocurrents excited by 340 nm, 440 nm and 540 nm wavelength light. (b) Reverse current over wavelength of incident light showing a strong increase when the nanowire is illuminated with light above the band gap energy.*

4.5.6 Dynamic core-shell model

There are already numerous publications concerning the behavior of ZnO upon UV illumination, but in spite of these efforts, the photocurrent mechanism is not yet completely understood: the reported photocurrent decay times range from 20 ns [41] to several minutes [95].

Figure 4.14 displays the results of the photoresponse measurement of a ZnO nanowire under illumination of light having a wavelength of 385 nm and after the light was switched off. Over the whole measuring time the bias voltage was held constant at 15 V. The current decrease when the light is switched off follows an exponential decay according to

$$I(t) = I_O + A_1 * exp(-\frac{t}{\tau}), \tag{4.13}$$

as shown by the fit to the measured data (gray line). The deduced decay constant τ was determined to about 400 s, where I_O denotes the current under dark conditions and A_1 the amplitude. Several measurements of the rise and the decay times of various VPT grown nanowires reveal slow response times (all are in the range of several minutes) and therefore indicate that the effects are surface, rather than bulk related.

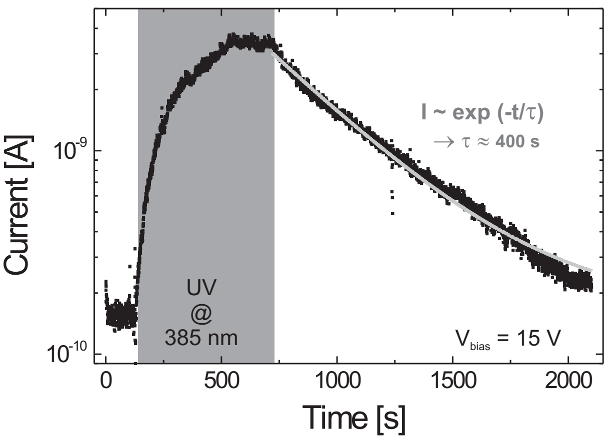

Figure 4.14: *Photoresponse of a ZnO nanowire under continuous illumination of 385 nm light and after turning off the light measured in air. Applied bias voltage was held constant at 15 V. Additionally added is a fit of the data following an exponential decay (first order). The corresponding decay constant τ was determined to about 400 s.*

It is commonly known that in darkness, oxygen molecules adsorb on the ZnO surface and capture electrons from the semiconductor [10, 41, 97]

$$\mathrm{O}_{2,gas} + e^- \rightarrow \mathrm{O}_{2,ad}^- \tag{4.14}$$

resulting in a surface charge depletion layer of low conductivity (”shell”) surrounding the conductive bulk material (”core”), as schematically shown in Fig. 4.15(a). Due to band bending effects resulting from Fermi level pinning at those surface states, the effective cross section A_{eff} for current transport differs from the geometrical cross section A_{geo} .

The behavior under illumination with light at energy above the band gap energy is shown in Fig. 4.15(b). UV illumination generates electron-hole pairs. Due to the decrease in the electro-chemical potential for the holes in direction to the surface, the holes drift to the surface region and neutralize the negatively charged oxygen ions according to

$$\mathrm{O}_{2,ad}^- + h^+ \rightarrow \mathrm{O}_{2,gas}. \tag{4.15}$$

which desorb from the ZnO nanowire surface leading to decreased band bending effects and an increased A_{eff} . It can be concluded that UV illumination not only results in an increase in current due to generation of additional carriers, but it also leads to a broader cross section for current transport. When the light is switched off, oxygen molecules adsorb on the nanowire surface and the conductivity decreases again, so the modification of surface states and conductivity under illumination is a reversible dynamic process.

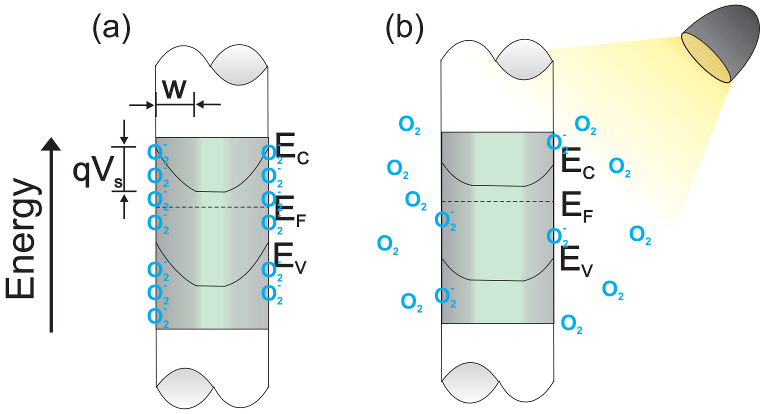

Figure 4.15: *Suggested core-shell model. (a) State of the ZnO nanowire under dark conditions and (b) modification of surface states and band bending effects under illumination with UV light.* V_s *denotes the surface potential,* w *the width of the depletion zone ("shell") while* E_F*,* E_C *and* E_V *respectively, represent the energy positions of the Fermi level, the conduction and the valence band.*

I-V measurements of the VPT grown ZnO nanowires were also performed and evaluated by D. H. Weber from the University of Bielefeld by using a low energy electron point-source (LEEPS) microscope to directly contact freestanding nanowires. In his set-up, a transmission electron microscopy graphite grid coated with a 100 nm gold layer and interspersed with holes about 3 µm in diameter, served as substrate. The nanowires with one end freestanding in the hole of the grid, were contacted by a movable manipulator tip (etched tungsten tip coated with Pt) while the carbon grid itself acted as counter electrode. A more explicit description of the measuring set-up using a LEEPS microscope can be found in [98, 99].

Also diameter-dependent measurements were performed (carried out in vacuum and under dark conditions), the obtained results are displayed in Fig. 4.16. Assuming that the effective cross section for current transport A_{eff} equals the geometrical cross section A_{geo} of the nanowires, the experimentally determined wire resistances of unit length R_L(black dots in Fig. 4.16) should follow an $1/d^2$ dependence (in accordance with $R_L = 4\rho/(\pi d^2)$), as indicated by the gray solid line, where d denotes the nanowires' diameters. However, especially for thinner wires, a deviation of the experimental data from the predicted $1/d^2$ behavior is noticed; the resistances lie below the expected values. This deviation from the expected behavior is attributed to the existence of a core-shell structure of the nanowires: It is assumed that the shell of thickness w exhibits a much larger resistivity than the core material ($\rho_{shell} >> \rho_{core}$). The equivalent circuit of the nanowire then consists of a core and a shell resistor in parallel configuration and the total resistance yields

$$\frac{1}{R_L} = \frac{1}{R_c} + \frac{1}{R_s} = \frac{\pi(d-2w)^2}{4\rho_c} + \frac{\pi[d^2-(d-2w)^2]}{4\rho_s}, \tag{4.16}$$

according to [98]. By using this geometrical model that separates between the shell (surface) and the core (bulk contributions) it was possible to fit the experimental data as shown by the dashed gray line added in Fig. 4.16. The determined shell thickness yields a value of $t \approx 23$ nm which is in good agreement with the width of the surface layer thickness deduced from diameter dependent PL measurements [100, 101].

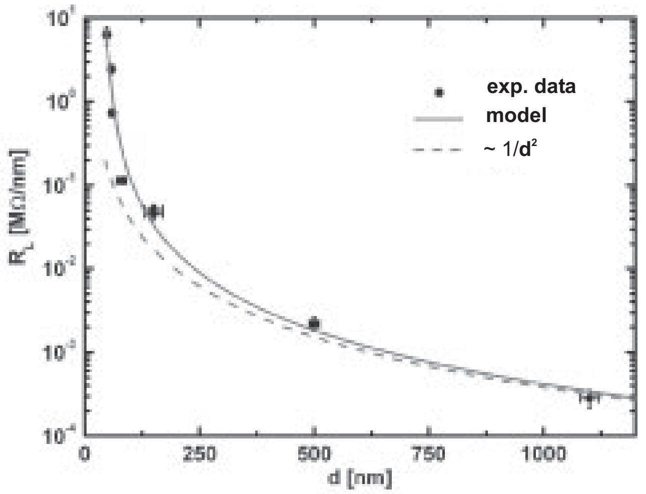

Figure 4.16: *Wire resistance per unit length over diameter of VPT grown ZnO nanowires measured in a LEEPS microscope. The solid gray curve corresponds to the expected* $1/d^2$ *behavior, while the solid line represents the best fit to the experimental data using the geometrical model (Eq. (4.16)). Image taken from [99].*

The existence of a shell of low conductivity especially influences nanowires of small diameters (the shell/core ratio might even exceed a value of 1), while for thicker nanowires the core is far larger than the shell and so hardly any impact is noted.

According to Eq. (4.9), the extension w of the surface depletion zone depends on the donor density N_d as well as on the surface potential V_S ($w \approx V_S/\sqrt{N_d}$). Figure 4.17 displays a set of calculated depletion widths for varying donor densities and surface voltages. The grey bars mark the results of the deduced shell width from the diameter dependent resistivity measurements performed in the LEEPS microscope (which yielded a value of about 23 nm) and the carrier concentration obtained from the I-V measurements presented in Chap. 4.5.4, from which a concentration of about 10^{15} cm^{-3} was estimated (by assuming an electron mobility of 50 cm^2/Vs). This value seems quite low even for high purity ZnO nanowires; however, it should be kept in mind that it was calculated by guessing that A_{eff} equals A_{geo}, whereas above results unambiguously reveal that $A_{eff} < A_{geo}$, so the actual carrier density in the nanowire will be larger than 10^{15} cm^{-3}. Therefore, values ranging between 5 x 10^{15} cm^{-3} and 5 x 10^{16} cm^{-3} were chosen that well match the carrier concentrations determined of bulk ZnO grown by vapor phase techniques [58].

As it can be seen by the calculations displayed in Fig. 4.17, the surface potential V_s should therefore range somewhere between 1 mV and 50 mV, depending on the donor density. This value seems to be small, however, regarding the low donor density in the high purity nanowires, already smallest potential fluctuations at the surface might have remarkable influences. Nevertheless, the obtained values of the surface potential should be just regarded as a rough estimate.

Furthermore, it should be kept in mind that the shell thickness of ≈ 23 nm was deduced from measurements performed in vacuum (by employing a LEEPS microscope). The width of the depletion layer in air will most likely exceed this value.

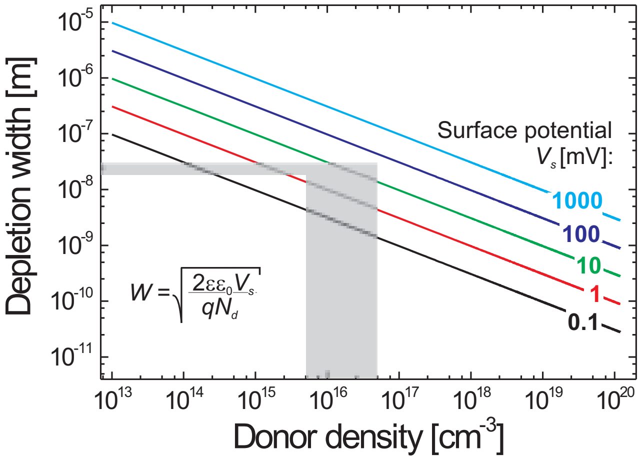

Figure 4.17: *Calculated depletion widths according to Eq. (4.9) for varying donor densities and surface potentials. The grey bars indicate the results of the deduced shell width and the carrier concentration.*

Additionally, calculations were performed in order to investigate the influence of the donor density, the nanowire radius and the mobility on the conductance (reciprocal of resistance) of a nanowire exhibiting such a core-shell structure. As basis for the simulation serves an equivalent circuit consisting of two resistors arranged in parallel configuration. One resistor represents the highly conductive core. It is assumed that charge carrier concentration in the core is constant and that it equals the donor density ($n \approx N_d$). The second resistor symbolizes the resistance of the depletion layer ("shell"). The extension of the depletion zone (w) depends on the donor density in the crystal according to Eq. (4.9). Furthermore, because of band bending effects due to Fermi level pinning at the nanowire surface, the carrier concentration in the depletion layer is not constant. It is determined by

$$n = N_C exp\left(-\frac{E_C - E_F}{kT}\right), \tag{4.17}$$

where N_C denotes the effective density of states in the conduction band.

For parallel arranged resistors, the total conductance is given by

$$G_{total} = \sigma_{shell}\frac{A_{shell}}{l} + \sigma_{core}\frac{A_{core}}{l}, \tag{4.18}$$

where σ_{shell} and σ_{core} denote the conductivity of the shell and core, respectively, A_{shell} and A_{core} the corresponding cross-sections and l the length. The conductance times the length of the nanowire therefore yields

$$G_L = \underbrace{2\pi q\mu N_d \int\limits_{r-w}^{r} xexp\left(-\frac{q^2 N_d}{2\epsilon\epsilon_0 kT}x^2\right)dx}_{\sigma_{shell}(x)A_{shell}} + \underbrace{q\mu N_d \pi(r-w)^2}_{\sigma_{core}A_{core}}, \tag{4.19}$$

where r symbolizes the radius of the nanowire, w the width of the depletion layer and x the radial distance from the center of the nanowire. A more detailed derivation of Eq. (4.19) can be found in Appendix B.

Figure 4.18(a) displays the calculated depletion widths over surface potential for varying donor densities. The dashed line represents a typical nanowire radius of 200 nm. Like already mentioned, for low donor concentrations already small band bending effects at the surface result in a broad depletion zone, e.g. for a donor concentration as low as 10^{15} cm^{-3}, less than 40 meV surface potential lead to the total depletion of the nanowire.

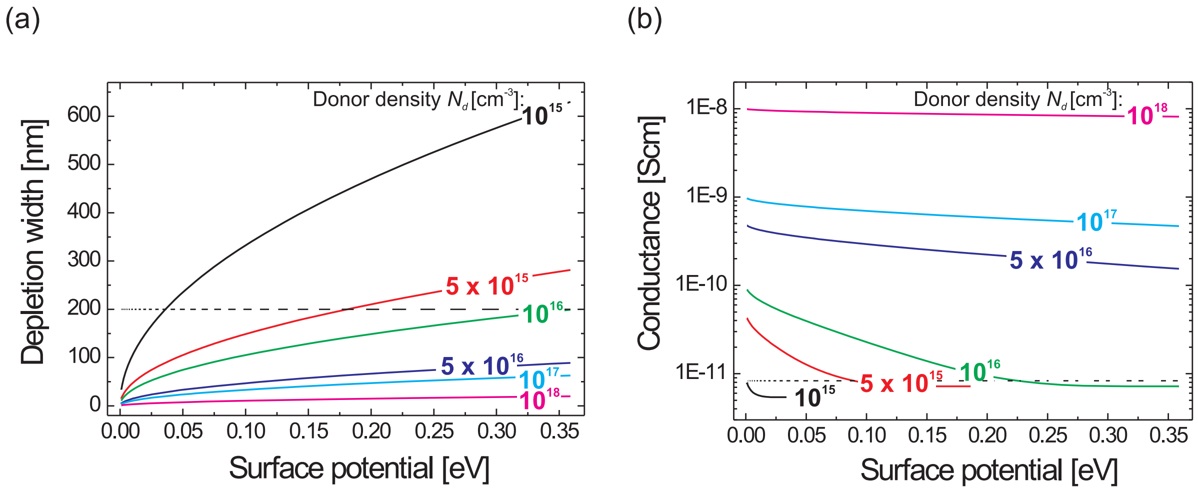

Figure 4.18: *(a) Calculated depletion widths (according to Eq. (4.9)) and (b) conductances (according to Eq. (4.19)) for varying donor densities and surface potentials. The curves in (b) were determined assuming a constant mobility of 50 cm^2/Vs and a nanowire diameter of 200 nm.*

The influence of band bending effects on the conductance of the nanowires is also clearly observable in Fig. 4.18(b). The curves were calculated supposing a constant nanowire radius of 200 nm and a mobility of 50 cm^2/Vs. The dashed black line corresponds to the value deduced from the measurement presented in Chap. 4.5.4, where a resistance of the nanowire over length of 12 MΩ/µm was determined. This value corresponds to a conductance of about 8 x 10^{-12} Scm.

As the simulated data clearly show, the conductance considerably decreases with increasing surface potential. The decrease is especially pronounced for low donor densities, whereas hardly any influence on the conductance is noted for donor densities exceeding 10^{17} cm^{-3}. For the nanowire investigated in Chap. 4.5.4 for which a diameter of 200 nm was determined, this yields a surface potential of about 0.23 eV (for a carrier concentration of 10^{16} cm^{-3} and by assuming a mobility of 50 cm^2/Vs).

Besides the donor density, also the diameter of the nanowire plays a significant role. Figure 4.19 displays the calculated conductances for varying nanowire radii using donor concentrations of 5 x 10^{15} cm^{-3} (Fig. 4.19(a)) and 10^{16} cm^{-3} (Figure 4.19(b)).

While in both cases the conductances rapidly decrease with increasing surface potential and decreasing wire radius, the decline is particularly distinct in nanowires with low donor densities.

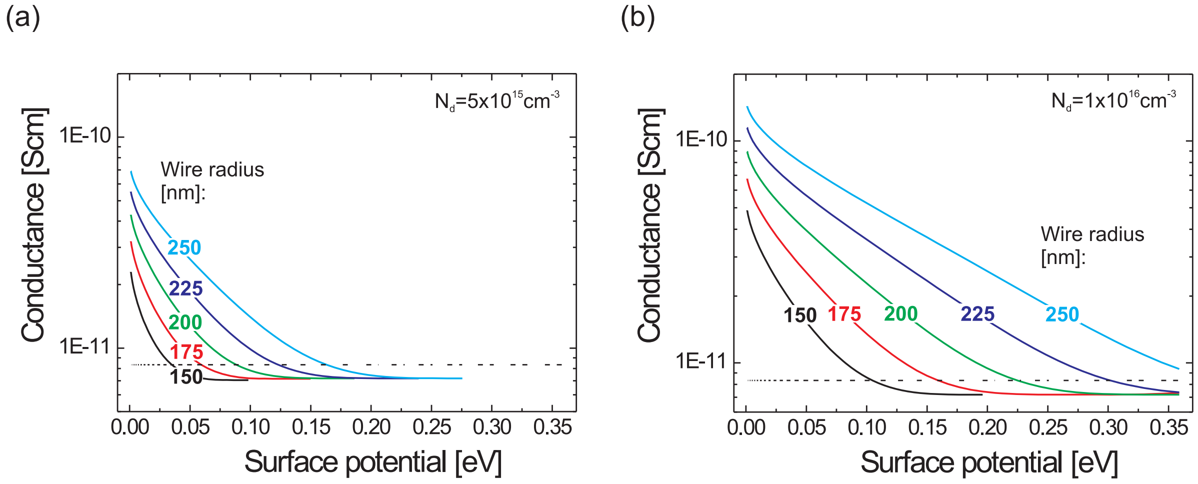

__Figure 4.19:__ Calculated conductances (according to Eq. (4.19)) for varying wire radii. The curves were determined assuming a constant mobility of 50 cm^2/Vs and donor densities of (a) 5 x 10^{15} cm^{-3} and (b) 1 x 10^{16} cm^{-3}.

Until now, a constant mobility of 50 cm^2/Vs has been assumed. However, it should be emphasized that surface effects not only directly influence the conductivity of the ZnO nanowires because of the diminished effective cross section caused by Fermi level pinning at surface states, but also the charge carrier mobility that sensitively depends on defects varies significantly with changing surface properties. Chang *et al.* reported an increase in mobility by a factor of 100 by passivating the surfaces of the nanowires with a SiO_2/Si_3N_4 bilayer coating [38]. Park *et al.* embedded nanowires in polyimide and found a rise in mobility from 75 to 1000 cm^2/Vs [94]. Also PL measurements reveal a reduction of surface traps by embedding the nanowires in PMMA [102].

Figure 4.20 displays the results of the calculated conductance values for varying mobilities. The curves were obtained assuming a nanowire radius of 200 nm and a constant donor density of 1 x 10^{16} cm^{-3}.

As expected, an increase in mobility leads to an increase in conductance. However, the behavior of the simulated data with increasing surface potential remains the same, independent of the mobility value used.

In order to investigate the influence of different atmospheres, *I*-*V* measurements of layers consisting of ZnO nanopowders were performed at various ambient conditions. Nanopowder particles have an enormous surface to volume ratio and are therefore especially suitable for this kind of investigation. The results are presented in Chap. 4.7.2.

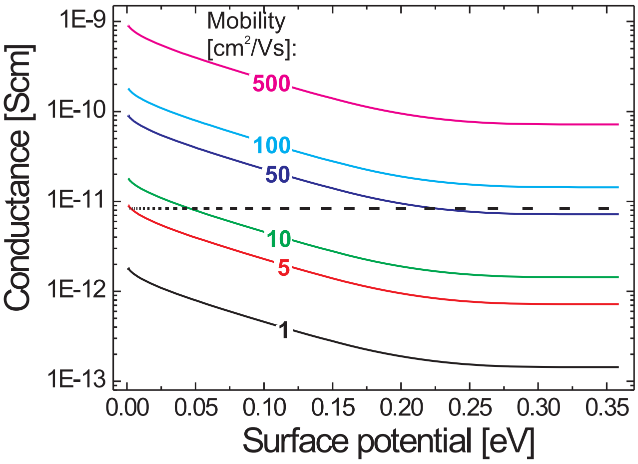

Figure 4.20: *Calculated conductances (according to Eq. (4.19)) for varying mobility values. The curves were determined assuming a constant nanowire diameter of 200 nm and a donor density of 1 x* 10^{16} *cm*$^{-3}$*.*

4.5.7 Overview of resistivity data

In this section, the resistivities of nanowires from multiple publications are brought together and compared to the values obtained from the measurements of the nanowires grown by VPT at the Institute of Semiconductor Technology which from here on will be simply referred to as "VPT grown". The VPT grown nanowires were either contacted by employing lithographic techniques as described above or they were measured by D. H. Weber in a LEEPS microscope [99].

When the resistivities of the nanowires were not explicitly stated in the literature, the values were deduced from the I-Vcharacteristics and the information given. Possible reading errors were taken into account (indicated by error bars). The I-Vcurves either show a linear, nonlinear or even rectifying behavior. In the latter case, the resistance of the device was determined from the linear section in forward bias like already shown in the lower inset of Fig. 4.11. Furthermore, data were extracted from single-nanowire FET characteristics at zero gate voltage.

It should be noted that this overview only considers ZnO nanostructures grown by non-aqueous approaches and at high temperatures. Additionally, although it is not explicitly mentioned in all the cited articles, it is assumed that all wires are of wurtzite crystal structure and preferentially grown in the c-axis direction. For the calculation of the resistivity they were treated like cylindrical wires.

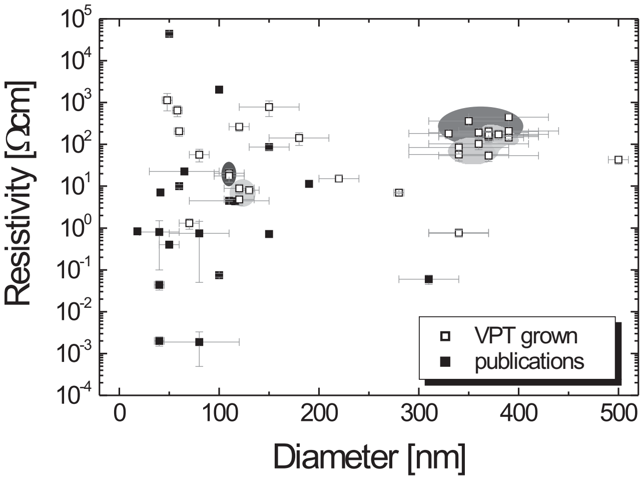

Figure 4.21: *Resistivity values of single ZnO nanowires over their diameter. The open symbols represent the data from measurements of the VPT grown samples; measurements belonging to different sections of the same wire are marked by the same color. Also added are the resistivities extracted from references [11, 38, 82, 93, 94, 103–113] (solid symbols). Possible reading errors are indicated by error bars.*

Figure 4.21 presents the measured resistivities of single ZnO nanowires over diameter. The open symbols correspond to the results of the VPT grown samples. For some devices multiple contacts along the wire were applied which enabled the investigation of the uniformity of the conducting channel. Measurements belonging to the same wire are marked by the same color. The resistivities deduced from measurements of the same nanowire lie close together, however, discrepancies up to one order of magnitude are also observed. They are likely due to the influence of contact resistances and inhomogeneities in carrier concentration within the nanowire.

The solid symbols represent values obtained from various publications [11, 38, 82, 93, 94, 103–113]. It should be pointed out that it is sometimes difficult to identify the actual shape of the nanowires by SEM. Like already stated, for determination of the resistivities, circular cross sections of the nanowires were assumed. However, in some cases, the wires were possibly rather oval-shaped.

As becomes clear from Fig. 4.21, the deduced resistivities of the VPT grown nanowires vary widely. The values range from about 1 Ωcm to 10^3 Ωcm; however, when taking into account all data, the resistivities differ even more, from 10^{-3} Ωcm to nearly 10^5 Ωcm. They differ by more than seven orders of magnitude, the variation is especially pronounced for diameters below 100 nm.

There are numerous factors influencing the resistance measurements of nanowire devices, like contact resistances, structural differences or ambient conditions. In the following section, some of these factors will be investigated in detail.

Measuring techniques and contact resistances

It seems likely that the applied measuring techniques also influence the electrical property measurements. Nearly all wires, except the ones measured in the LEEPS microscope, were deposited on a substrate, so that there was a good heat coupling between the nanowires and the environment. For the freestanding nanowires measured in the LEEPS set-up, no significant difference in resistivity was observed compared to those deposited onto a Si substrate and contacted by Ti/Au electrodes.

In order to investigate the influence of the contacting techniques, Fig. 4.22(a) assigns the experimental data to the contacting methods. For some measurements, movable tips served as electrodes (referred to as ”manipulator”), but the vast majority of nanowires were contacted by top-electrodes patterned either by using e-beam- or photo-lithography. In three cases, the nanowires were deposited onto a substrate already pre-structured with electrodes (this category is referred to as ”deposition”), and, for one device, the conducting paths were directly defined by employing focused ion beam (FIB). As Fig. 4.22(a) shows, no influence of the measuring technique on the deduced resistivity is observable.

Figure 4.22(b) allocates the resistivities to the shape of the corresponding I-Vcurves. The majority of the devices exhibit a non-linear behavior indicating Schottky contacts of different barrier heights. Also a number of samples show linear I-Vcharacteristics which tend to have smaller resistivities compared to the nanowires showing a non-linear behavior. This is displayed by the dashed lines included in Fig. 4.22(b) as a visual aid.

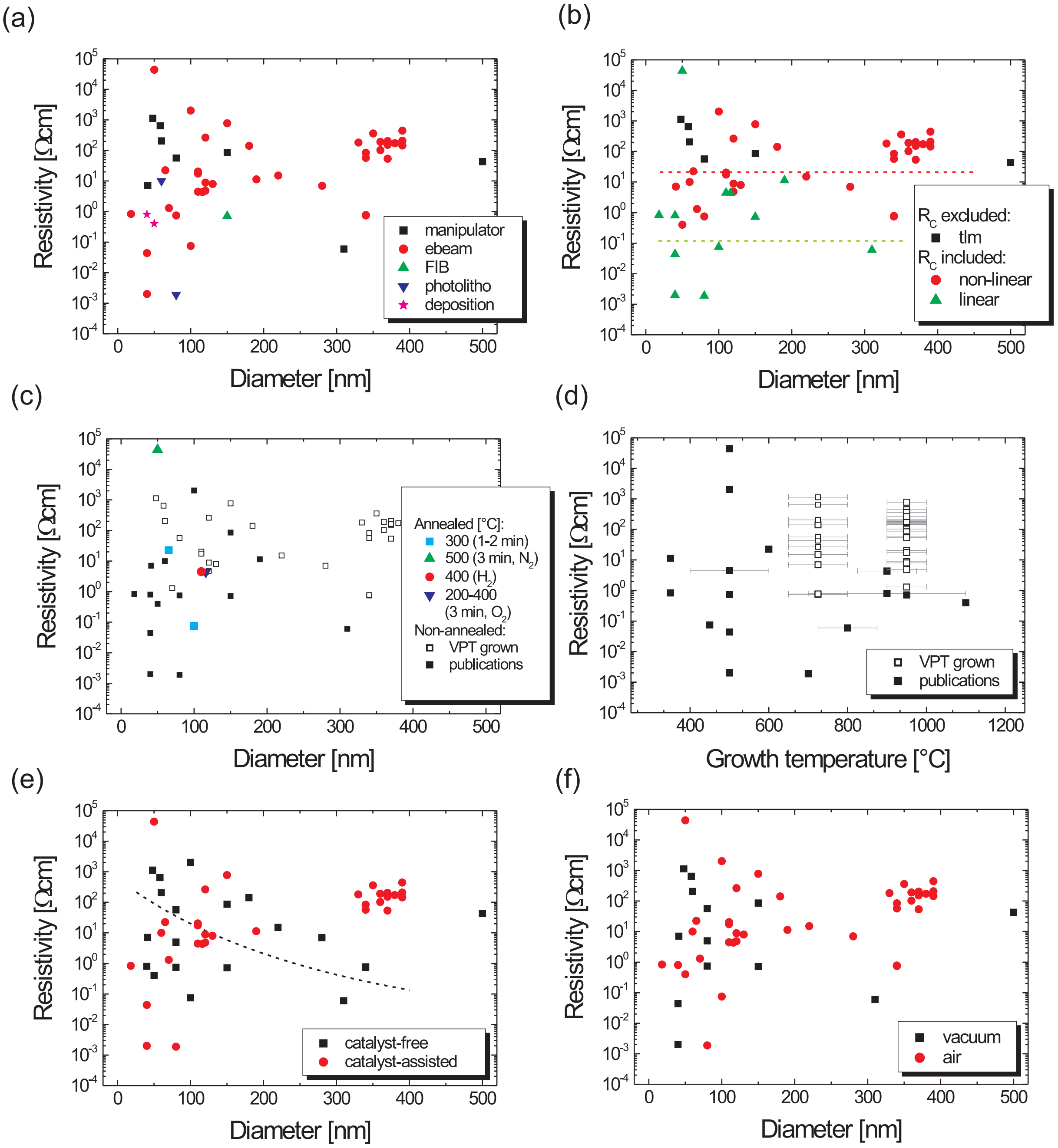

Figure 4.22: *Resistivity values of single ZnO nanowires. The deduced values are classified according to (a) the measuring method applied and (b) the shape of the corresponding I-V characteristics. Note that the lines do not represent the average values of the measured data but are merely added to guide the eye. Image (c) shows the dependence on post-deposition heat treatments and (d) the dependence on growth temperature. The graph in (e) depicts the influence of the use of a catalyst during growth while (f) assigns the resistivities to the ambient conditions (vacuum, air).*

Since most data points are extracted from two-probe devices, the measured resistances contain contributions from the resistances of the nanowires as well as from the contact resistances. Possible influences from non-ohmic contacts can be excluded from measurements performed in the LEEPS microscope. In this set-up, the contact resistances can be totally eliminated from the resistance of the nanowire by performing a series of measurements (transmission line measurements (TLM)) at different positions of the nanowires [98]. A rough estimate of the contact resistance of the VPT grown samples contacted with Ti/Au electrodes (all wires displayed non-linear I-Vcurves) yielded a contact resistance of about 85 MΩ as presented in Chap. 4.5.4. This value lies within the same range as the wire resistance.

But also for linear I-Vcharacteristics, contact resistances still play an important role. Goldberger *et al.* contacted nanowires by Ti/Au electrodes and measured in two- as well as in four-probe geometry (in air). Even though both devices showed linear I-Vcharacteristics, the contact resistance was still 2 to 10 times the resistance of the nanowire [110]. Lao *et al.* obtained rectifying I-Vcurves by aligning ZnO nanobelts across prefabricated Au electrodes using a dielectrophoresis technique. For the same device, they deposited Pt by using FIB at the nanowire/Au interface in order to change the contact properties. After deposition, the I-Vcharacteristics became linear and the total resistances decreased 5 to 20 times [87].

It is indisputable that contact resistances significantly influence electrical transport measurements of ZnO nanostructures. But, as mentioned above, investigation of the contact resistances show that they lie within the same range as the resistances of the nanowires or exceed them by about one order of magnitude. Additionally, the VPT grown samples measured by the TLM method show comparatively high resistivities (Fig. 4.22(b)), even though the contact resistances are explicitly subtracted from the resistances of the nanowires. Therefore, the contact behavior cannot be solely responsible for the enormous differences in the resistivities (10^{-3} Ωcm to 10^{5} Ωcm). However, the shape of the I-Vcharacteristic gives indications of the charge carrier concentration within the nanowires.

Like already extensively discussed in Chap. 4.2.1, higher doping concentration and therefore a higher charge carrier concentration in the system leads to increased tunneling through a narrower Schottky barrier formed at the metal/ZnO interface. If the width is sufficiently small, the electrons can effectively tunnel through the barrier even at low applied voltages resulting in a linear I-Vbehavior. For nearly undoped ZnO, the depletion region extends far into the semiconducting material and higher voltages are necessary to achieve a current flow (non-linear I-Vcurves). These findings are supported by experiments on ZnO layers where the influence of near-interface defects on Schottky barriers were investigated. Low-defect crystals exhibited strongly rectifying I-Vcharacteristics while ZnO layers with a high defect density showed an ohmic behavior. This finding was attributed to either impurity band transport or increased doping with increasing defect density [114].

Additionally, it should be noted that the deposition of contacts using FIB seems to be a reliable technique to obtain linear I-Vcurves [87, 104]. This is probably due to the ion bombardment of the nanowire that results in a local increase of the charge carrier concentration at the position of the electrodes.

Transport measurements carried out with the LEEPS microscope show that even the contact geometry influences the shape of the I-Vcurves. Furthermore, it was demonstrated that simple point contacts result in linear I-Vcurves [99]. This is owing to the fact that with decreasing contact size, the Schottky barrier thickness decreases due to an increase in the electric field strength. As a consequence, the contact resistance of the diode is strongly reduced and the contribution of tunneling to the total conductance is significantly enhanced [115].

For nanowires contacted by top-electrodes, a variety of metals were utilized (mostly Ti, but also other metals like Ni or Al); however, the analysis of the experimental data implementing different contact materials revealed no influence.

In some cases post-deposition heat treatments were applied to lower the contact resistances [94, 103, 105, 107, 110], as shown in Fig. 4.22(c). All annealed devices exhibit linear I-Vcharacteristics, as can be derived from comparing Fig. 4.22(b) and Fig. 4.22(c). Annealing leads to a metal-semiconductor alloy and to the local increase of charge carriers at the position of the electrodes. This results in a decreased Schottky barrier width and an increased tunneling current. Note that in one case the second electrode was evaporated after annealing since it was intended to produce rectifying contacts [107].

It can be concluded that contact resistances influence the electrical measurements of ZnO nanostructures; however, the investigations revealed that they can not be the main reason for the discrepancies observed in the resistivities; they have to be attributed to other factors.

Structural differences

According to Eq. (4.3) the resistivity ρ is inversely proportional to the charge carrier concentration n and to the mobility μ, therefore structural differences in the nanowires influence ρ in multiple ways. Figure 4.22(d) shows the determined resistivities over the growth temperature (in references [82, 113] no information was given). All samples under investigation were grown at temperatures exceeding 350°C. The largest variation (10^{-3} Ωcm to nearly 10^{5} Ωcm) occurs at around 500°C, however no general tendency is observed.

Growth temperature affects the crystallinity as well as the defect density in the nanowires. Another factor that may influence the number of defects (like incorporated impurity atoms) is the use of a catalyst. Figure 4.22(e) compares the resistivities of the nanowires grown in a catalyst-assisted process with the ones grown without the use of a catalyst. No definite dependence is noticed, but a slight tendency is observed; the nanowires grown with the use of catalysts exhibit smaller resistances than the ones produced without. Furthermore, the resistivities of the latter tend to decrease with increasing diameter, as indicated by the dashed line which was included as a visual aid. A similar behavior was already observed in the diameter dependent resistance measurements presented in Fig. 4.16 which was attributed to surface effects which impact decreases with increasing diameter of the nanowires.

Figure 4.22(d) and 4.22(e) both illustrate possible influences of growth parameters on the crystallinity of the samples. Independent of temperature and method applied, almost all nanowires are of single crystalline quality ([11, 38, 93, 94, 103, 104, 106–113], for [82, 105] no information is given) as TEM images reveal. The images show no structural defects and prove the single crystallinity of the nanostructures. However, no conclusions can be drawn concerning the number of point defects like vacancies or interstitials, since image acquisition in TEM is based on diffraction and interference and is nearly insensitive to randomly distributed point defects [116]. As already stated, the existence of point defects influences the resistivity in multiple ways; on the one hand they lead to an enhanced carrier concentration but on the other hand they diminish the mobility.

Liu *et al.* and Lao *et al.* studied the resistance behavior over time upon air-exposure. Lao *et al.* performed measurements on nanobelts at time intervals ranging between 2 hours and 7 days after fabrication of the devices. At all times, they obtained rectifying I-Vcharacteristics and the resistance was stable throughout the whole period [87]. In contrast, Liu *et al.* passivated parts of the surface of a ZnO nanobelt. The passivation process introduced defects to the nanobelts leading to an increased number of oxygen vacancies. Over a period of 8 days, the conductivity of the nanobelt decreased by almost 50 % which was attributed to oxygen diffusion into the ZnO and the filling of the oxygen vacancies [117]. Therefore, the density of point defects seems to be one of the determinant factors concerning the resistivity of ZnO nanowires.

However, it should be noted that the cause of the n-type conductivity is still widely debated. In the year 2000, Van de Walle claimed that the prevailing n-type conductivity can not be attributed to native defects. His theoretical calculations reveal that hydrogen is always a donor in ZnO which is easily ionized. It therefore seems to be the dominant donor in ZnO nanostructures that were exposed to hydrogen during growth [64]. In contrast to these results, Look *et al.* state that native donors contribute significantly to the conduction in ZnO but as complexes, rather than isolated elements [118].

Surface morphology

Even though the nanowires are of single crystalline quality, sometimes they exhibit a considerably rough surface, and in some cases, crystalline imperfections in the outermost layer are observed. Lin *et al.* found out that even if grown under identical conditions, some nanowires are covered with a non-crystalline or amorphous layer, while others showed perfect crystalline structures even at the boundary layer [106]. The origin of the amorphous layer is not yet clear. Comini *et al.* ascribe the formation to condensation of vaporized material during cooling in the growth process [119]. It also seems likely that it is formed when the nanowires are exposed to ambient conditions and adsorption on the surface takes place.

Not only from TEM but also from PL measurements conclusions can be drawn concerning the surface morphology of the nanostructures. Voss *et al.* detected a stronger contribution of the first longitudinal optical (1LO) phonon replica of the free exciton (FX) in the PL spectra of VPT grown nanowires. This transition is usually forbidden in perfect crystals and therefore indicates a higher level of crystal imperfections [120]. However, TEM images did not reveal any structural defects or dislocations. The authors assume that the fairly rough surface might be responsible for the occurrence of the FX-1LO peak. It therefore seems possible, that surface roughness also influences the electrical properties of the nanowires.

Influence of ambient conditions

Like already discussed in Chap. 4.5.6, also ambient conditions essentially affect the electrical characteritics of ZnO. Particularly nanostructures with their large surface to volume ratio are sensitive to variations in illumination, atmospheric composition and humidity. Figure 4.22(f) assigns the resistivities to the atmospheric composition, either air or vacuum, but no general trend is observed.

Ambient conditions sensitively influence the electrical properties. This is not only valid during execution of the experiment, also the conditions (like illumination) in the time period before the actual measurement may still interfere with the result. When regarding the relatively long decay times in the order of several minutes, it is absolutely necessary that the device is given sufficient time to settle in a stable state. Alternatively, the ambient conditions should be explicitly stated. Especially for nanowires measured in a TEM or SEM set-up, care should be taken to rule out possible impact of the electron radiation on the resistivity measurements of the nanowires.

The discussion above therefore shows that it is not possible to pinpoint the differences in the observed resistivites to one single reason. They result from the interaction of multiple factors influencing the resistance measurements. Special care should be taken when interpreting electrical measurements of single ZnO nanowires and ambient conditions. Time periods prior to the actual measurement should also be taken into account.

4.6 Electrical properties of ACG grown nanowires

This section presents the results of electrical transport investigations of single ZnO nanowires grown by an aqueous chemical approach. All measurements were performed at room temperature and in air, but different contacting techniques were applied. The results of the measurements employing different measurement set-ups are compared.

4.6.1 Electrical properties of nanowires grown on conductive substrates

Sets of nanowire arrays were grown by ACG on glass covered with conductive ITO which served as back contact. Manipulator tips were employed as top electrodes which enabled the contacting and the measuring of electrical properties of single as-grown ACG nanowires. One set of samples was investigated by using an atomic force microscope (AFM) equipped with a conductive tip. Further measurements took place in a SEM.

Measurements performed by conductive AFM

In one approach, *I-V* characteristics of as-grown nanowires were obtained using an AFM system with a conductive polygonal shaped tip. The tips had a radius of curvature of about 100-200 nm and were about 10-15 µm in height.

In a slightly modified set-up, the gaps between the as-grown nanowires were filled with an insulating material in order to prevent short-circuiting between the AFM-tip and the ITO. The nanowires were embedded in photoresist and subsequent exposure of the photoresist to UV-illumination in combination with selective etching lead to electrically isolated nanowires with only their tips exposed. Figure 4.23 shows a SEM image of such a device.

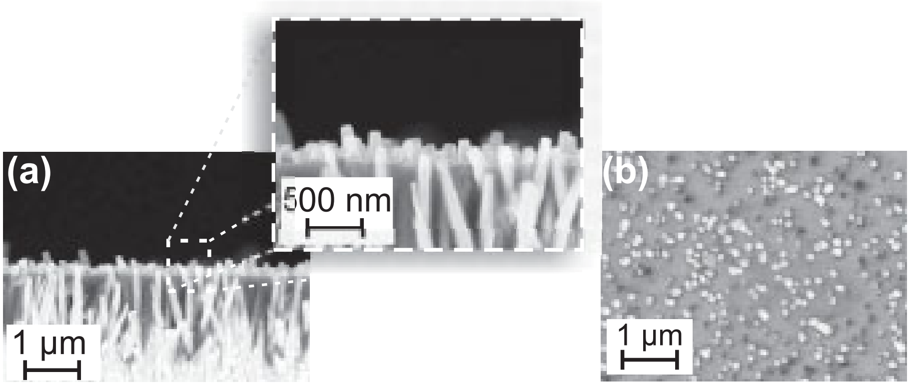

Figure 4.23: *(a) Lateral and (b) top view of ACG grown nanowires embedded in photoresist with only their tips exposed. (For SEM image acquisition, nanowires were grown on a Si substrate.)*

Figure 4.24(a) shows the averaged *I-V* data of four measurements taken at different positions on the bare nanowire array, the inset displays a schematic view of the corresponding set-up. The obtained characteristic clearly displays a rectifying behavior corresponding to the one expected for Schottky contacts either with barriers of different heights at the front as well as at the back contact or with one barrier and a break-down voltage with a value similar to the turn-on voltage for an opposite bias. The turn-on/breakdown voltages were found to be in the range of 0.4 V and -0.5 V for positive and negative bias, respectively. The corresponding averaged *I-V* curve measured from the embedded nanowires is shown in Fig. 4.24(b). Compared to the characteristic obtained of the bare nanowires, in the negative bias range, only a much smaller current is measured whereas for positive bias voltages no difference is detected.

Regarding the geometry of the AFM-tip (height 15 µm) and the length of the nanowires (about 2 µm) it seems likely that for the investigations on the bare wires, the tip might penetrate the nanowire array, encounters the ITO and partly short-circuits the measurement. For the embedded wires, a rectifying characteristic corresponding to an AFM-tip/ZnO-nanowire Schottky contact is obtained. Therefore, filling the gaps of the wires with insulating material is essential when using manipulator tips to contact single as-grown nanowires. However, it should be kept in mind that enclosure of the nanowire surface always involves a change of surface states and therefore a change of resistivity.

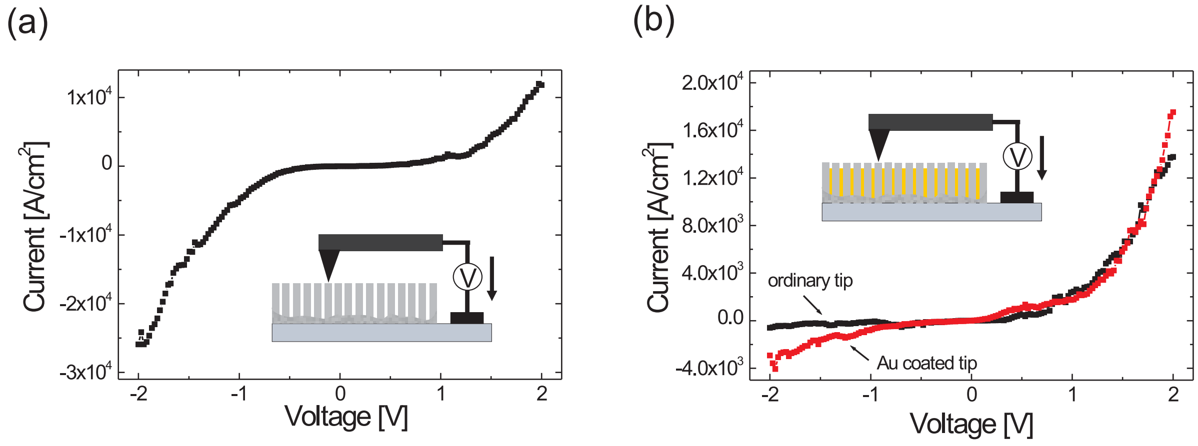

Figure 4.24: *I-Vcharacteristics of the ITO/ZnO/AFM-tip structure on (a) bare and on (b) embedded nanowires. The characteristics display the averaged data of multiple measurements taken at different positions of the nanowire array sample. The insets show the corresponding schematic current sensing AFM set-ups.*

Both the AFM-tip and the ITO form Schottky contacts to the ZnO; however, the barrier width at the ZnO/ITO interface is smaller compared to one at the ZnO/AFM tip. As described in Chap. 3.4.2, randomly oriented ZnO seed crystals spread over the ITO layer serve as catalysts. Therefore, the nanowires grow in arbitrary directions according to the orientation of the seed crystals at the beginning of growth. This leads to the formation of a defect rich and therefore highly conductive polycrystalline layer in direct vicinity to the substrate, as the TEM measurements shown in Fig. 4.25 reveal. A more detailed explanation describing the origin of this layer can be found in [78].

In order to apply a different contact metal, the bare AFM-tip was coated with Ti/Au (30 nm/100 nm, Ti as adhesion layer). Therefore, in this slightly modified set-up, Au served as electrode material. The gray curve in Fig. 4.24(b) represents the obtained *I*-*V* data. The results indicate that there is no significant difference in the behavior compared to the non-modified tip.

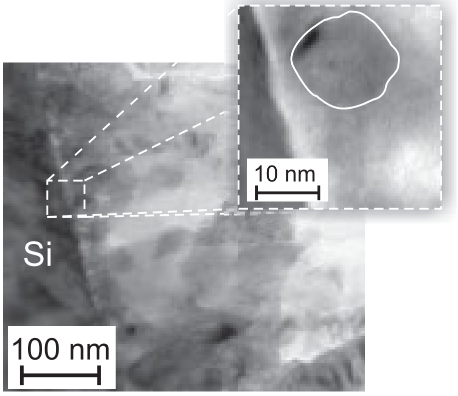

Figure 4.25: *TEM measurements of the growth substrate/nanowire interface region revealing the existence of a polycrystalline layer. Image provided by A. Travlos, Demokritos Institute of Athens, Greece.*

An estimate of the resistivity of the ACG grown nanowires was deduced by fitting the linear section of the averaged I-V characteristic measured with the Au coated tip. Taking the dimensions of the nanowires into account (average diameter of 160 nm and 2 µm in length) the resistivity yields a value of about 0.2 Ωcm.

Measurements performed by a manipulator tip in a SEM

Additionally, measurements of single as-grown nanowires were performed in a SEM at Kleindiek Nanotechnik in Reutlingen, Germany. In this set-up, an etched tungsten tip was employed as movable electrode to provide the top contact, while ITO served again as back electrode.

Figure 4.26 depicts the results of the I-V measurements of several nanowires. The majority of characteristics show rectifying behaviors due to the contact barrier formed at the tip/ZnO interface (note that the voltage was applied to the manipulator tip while the ITO was grounded), but also a linear I-V curve was obtained. Furthermore, all characteristics intersect the abscissa not at zero voltage but at around -0.4 V. Such a voltage shift was also observed on measurements on GaN nanopillars measured employing a tungsten manipulator tip in a SEM (at Kleindiek Nanotechnik). It was found that the voltage shift depends on the sweep direction of the applied bias voltage, both if the measurements were performed from negative to positive bias and vice versa. This indicates that the observed voltage shifts are likely due to the charging and discharging of either contact capacitances or of capacitances caused by the measurement set-up. Nevertheless, the shift will have no impact on the resistivity which was determined to about 0.1 Ωcm. This value was

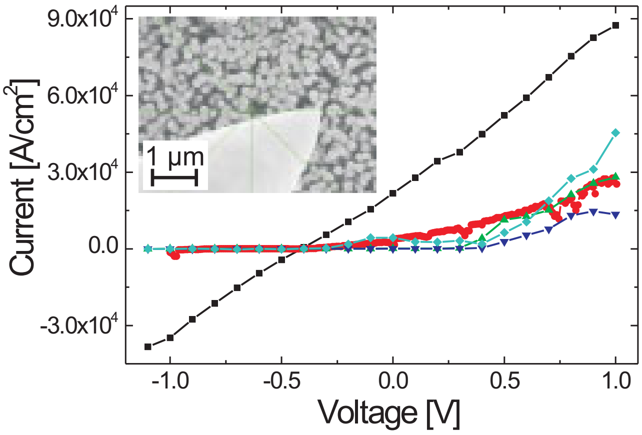

Figure 4.26: *I-Vcharacteristics of embedded nanowires grown on ITO and contacted by a tungsten manipulator tip in a SEM. The insets shows a SEM picture of a contacted nanowire. Measurements were performed at Kleindiek Nanotechnik.*

calculated by assuming a wire diameter of 180 nm and a length of 2 µm and it represents the averaged data of all five measurements.

4.6.2 Electrical properties of single isolated nanowires

In addition to the electrical transport investigations carried out on nanowires grown on conductive substrates, also measurements on from the growth substrate detached wires were performed. Those were either contacted by employing e-beam lithography for structuring the electrodes (like described in Chap. 4.5.1) or the samples were investigated by D. H. Weber, University of Bielefeld, in a LEEPS microscope.

Figure 4.27 depicts *I-V* curves of single ACG grown nanowires. The inset shows a SEM image of the contacted nanowire belonging to the marked *I-V* characteristics.

The nanowires have different diameters ranging from 160 nm to 300 nm and lengths ranging from 610 nm to 1.45 µm. A rough estimation of the average resistivity of the ACG nanowires yields about 4 Ωcm which is in good agreement to the value of 4.9 ± 1.2 Ωcm obtained by measuring an ACG grown nanowire in the LEEPS microscope [99].

Table 4.1 summarizes the deduced resistivity values of the ACG grown nanowires contacted by different methods. Independent of the contacting method applied, all deduced values lie within a narrow range. Compared to the specific resistances of the samples grown by high-temperature VPT processes, it is found that the resistivities of the ACG

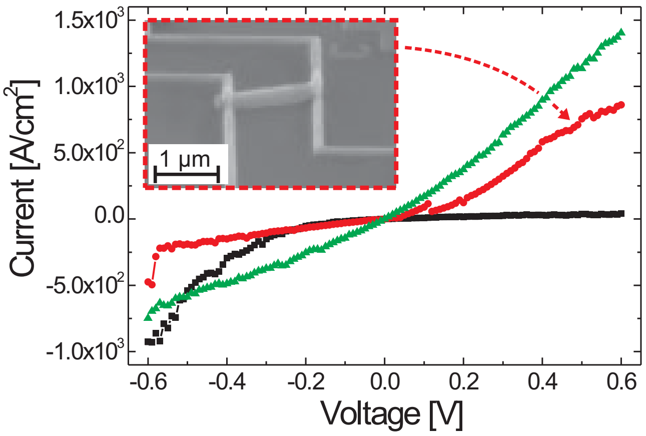

Figure 4.27: *I-Vcurves of single isolated nanowires grown by ACG. The inset shows a SEM image of the contacted nanowire belonging to the marked characteristic.*

Table 4.1: *Resistivity values of ACG grown nanowires contacted by using various methods.*

Contacting method	**Wire diameter [nm]**	**Resistivity [Ωcm]**
Conductive AFM	160	0.2
Manipulator tip (SEM)	180	0.1
E-beam lithography	300	3.8
LEEPS microscope	80	4.9

grown nanowires are at least one order of magnitude lower than the ones determined of the VPT grown nanowires (1 Ωcm- 10^3 Ωcm). This decrease in resistivity could be due to an increased amount of hydrogen atoms incorporated into the ZnO nanowires (growth in aqueous solution) while hydrogen is identified to act as shallow donor in ZnO. Furthermore, it is well known that aqueous chemical growth leads to an enhanced formation of defects in the crystal matrix resulting in an increased carrier concentration. This assumption is also confirmed by PL measurements. While the PL spectra of the ACG grown samples reveal a large linewidth of the near-band-edge emission (∼ 10 meV) and the absence of excitonic transitions which are signs of a high defect and donor density [121, 122], the linewidth of the VPT grown sample is rather small (∼ 0.7 meV) and also free exciton transitions appear which indicate high quality nanowires with a low number of defects.

In order to get an estimate of the carrier concentration in the nanowires, a mobility of 50 cm^2/Vs is again assumed which (according to Eq. (4.3)) results in values between 3 x 10^{16} cm^{-3} and 6 x 10^{17} cm^{-3}. However, the nanowires grown by ACG will most likely exhibit lower mobilities than the VPT grown samples due to an enhanced scattering rate on defects. Therefore, the actual charge carrier concentrations will probably be around 10^{18} cm^{-3} or even higher.

The listing of the resistivities in Tab. 4.1 shows that even though the variation of the resistivity is quite small, a slight tendency is observed that the embedded nanowires have lower resistances than the single ones from the growth substrate detached samples. On the one hand this might result from the influence of the contact resistances; however, it might also be due to a reduction of surface states because of the sheathing of the nanowires with photoresist. In contrast to the VPT grown nanowires, the influence of surface states will be less significant on electrical transport properties of ACG grown nanowires; the larger the carrier concentration in the wires, the smaller the extension of the depletion region.

4.7 Electrical properties of nanopowders

While nanowire based devices are still in the laboratory stage, the pressing and sintering of powders has already been used for years to produce ZnO based electroceramics like varistors [123]. Also powders consisting of nanoscale particles already found application as sensing elements in gas detectors [124, 125].

There are multiple ways to fabricate ZnO nanopowders, for example by wet chemical synthesis [126], solid state pyrolic reactions [127] or by thermal oxidation [128]. Today, they can be ordered from industry in every desired particle size.

In this work, high-purity ZnO nanopowder was obtained from Grillo (Grillo Zinkoxid, Germany). One set of samples was prepared by pressing the powder particles under quasi-hydrostatic pressure of 30 MPa at 250°C for 5 min. The resulting disks have typical dimensions of about 1.3 cm in diameter and less than 250 µm in thickness and require no supporting substrate. In a different approach, the powder particles were dispersed in isopropanol. Nanopowder layers were deposited by dropping the colloidal dispersion onto insulating substrates (for example glass) covered by a thin layer of ZnO seed crystals. Evaporated Ti/Au electrodes served as electrical contacts.

The results of the structural investigation of the ZnO nanopowder are presented in the following paragraph. Furthermore, the influence of UV illumination, different atmospheres and humidity on the electrical transport properties are discussed.

4.7.1 Structural properties

Figure 4.28 displays scanning electron micrographs of a disk consisting of pressed ZnO nanopowder. The ZnO particles are very homogeneous in shape and size, their average diameter was determined to about 25 nm.

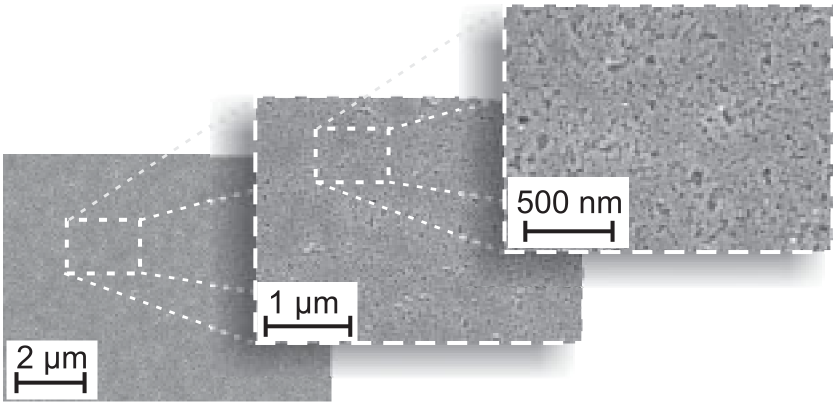

Figure 4.28: *Scanning electron micrographs of varying magnification showing pressed ZnO nanopowder particles.*

The surface of the pressed devices was investigated by AFM. On the 500 nm x 500 nm scan shown in Fig. 4.29, a maximum elevation of 25 nm was observed which is consistent with the average particle diameter. The evaluated roughness (root mean square) yields a value of 3.45 nm.

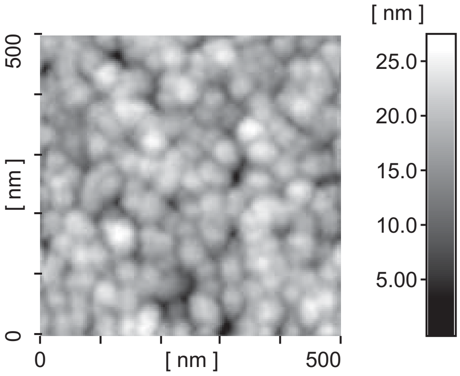

Figure 4.29: *Atomic force micrograph of a pressed ZnO nanopowder disk.*

In order to investigate the crystallinity of the samples, TEM and X-ray diffraction (XRD) spectroscopy measurements were performed by H. Schmid, University of Bonn and

H. Bremers, Technical University of Braunschweig. The specimens for TEM investigations were prepared by dispersing the powder particles on a holey carbon film. The particles are of single crystalline quality as proved in Fig. 4.30, but also agglomeration is observed.

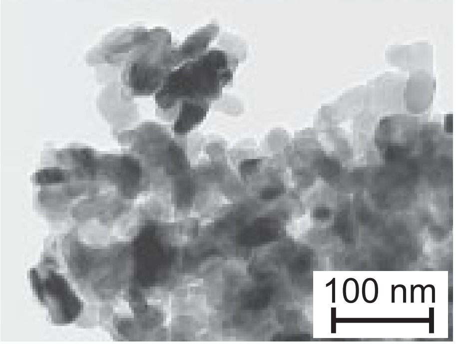

Figure 4.30: *Transmission electron micrograph showing loosely aggregated powder particles of single crystalline quality.*

The corresponding XRD spectrum is shown in Fig. 4.31. For comparison, the peak positions of a simulated XRD scan of randomly oriented wurtzite ZnO powder are also displayed. All diffraction peaks observed in the $\theta - 2\theta$ scan match the powder pattern of wurtzite ZnO.

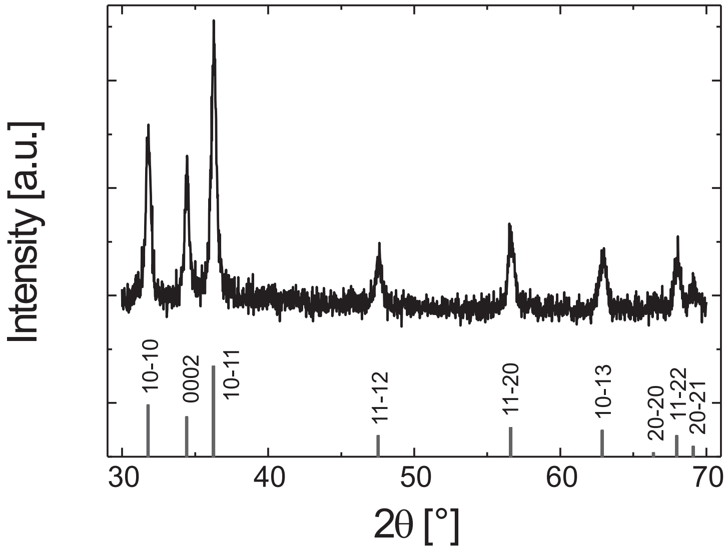

Figure 4.31: *$\theta - 2\theta$ XRD pattern of ZnO nanopowder. Additionally depicted are the peak positions of a simulated XRD scan of randomly oriented wurtzite ZnO crystals.*

4.7.2 Electrical properties

Electrical properties of pressed nanopowders were investigated by distance dependent measurements. Multiple contacts were evaporated onto one disk as schematically shown in the inset of Fig. 4.32(a). While electrode ”a” was fixed, the position of the second electrode (”b” to ”g”) varied. The resulting *I*-*V* characteristics are displayed in Fig. 4.32(a). The measurements were performed in air and under standard light conditions (ordinary laboratory fluorescent lamp).

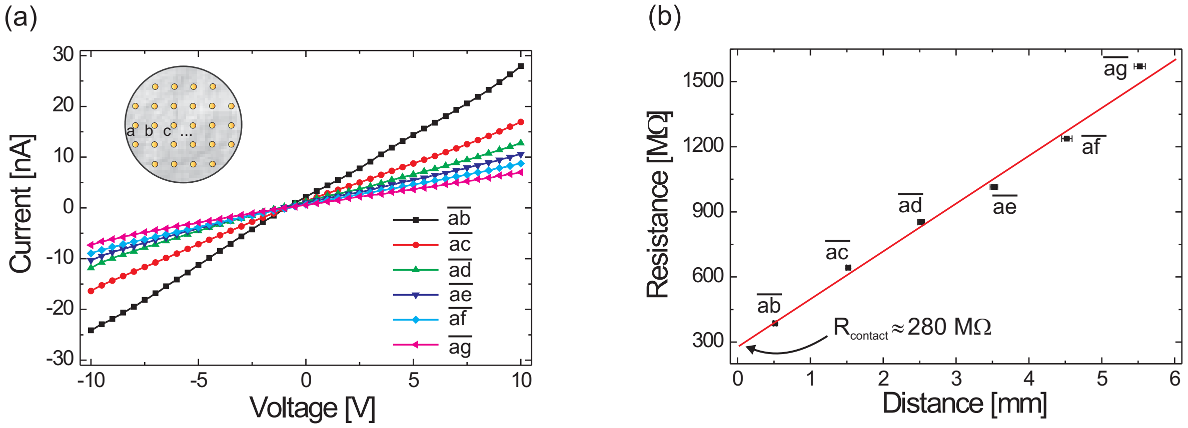

Figure 4.32: *(a) Distance dependent resistance measurements of a pressed nanopowder disk. Electrode ”a” was fixed while the position of the second electrode was varied (from ”b” to ”g”). The inset shows a schematic image of the disk with the contact pads. (b) Deduced resistances over distance.*

All *I*-*V* data show a nearly linear behavior and the deduced resistances over length displayed in Fig. 4.32(b) prove that the resistance almost linearly increases with increasing electrode distance. This confirms the uniformity of the sample. However, it should be pointed out that the measurements were not performed according to the transmission line method because of arising difficulties during structuring attempts of the device.

The electrodes are evaporated onto the top of the disk. The fit of the data extrapolated to zero distance yields a contact resistance of $R_C \approx 280$ MΩ, which is comparable to the value determined for the nanoscale contacts on ZnO nanowires.

In order to compare, *I*-*V* data were evaluated of ZnO nanopowders dispersed in ethanol and drop-casted onto a glass substrate. Using the same conditions as before, no current was detectable on a pA scale. This high resistivity results from the inhomogeneous distribution of the powder particles. Furthermore, the contact resistances at the particle-particle interfaces of the loosely connected grains will be larger than in the pressed disks.

Photoconductive properties

In Chap. 4.5.5 it was already shown that UV illumination drastically changes the electrical properties of ZnO nanostructures and that surface reactions determine the overall conductivity. Compared to ZnO nanowires, devices based on nanopowders exhibit even larger surface to volume ratios and are therefore ideal test structures to further investigate the influence of ambient conditions.

Samples consisting of loosely connected nanopowder grains are highly resistive and no current could be measured in darkness or under standard light conditions. However, under UV illumination, the current increased by several orders of magnitude. In order to explain this large photoresponse, Figure 4.33 displays a cut-out of the corresponding equivalent circuit of the powder sample in darkness (a) and under UV illumination (b).

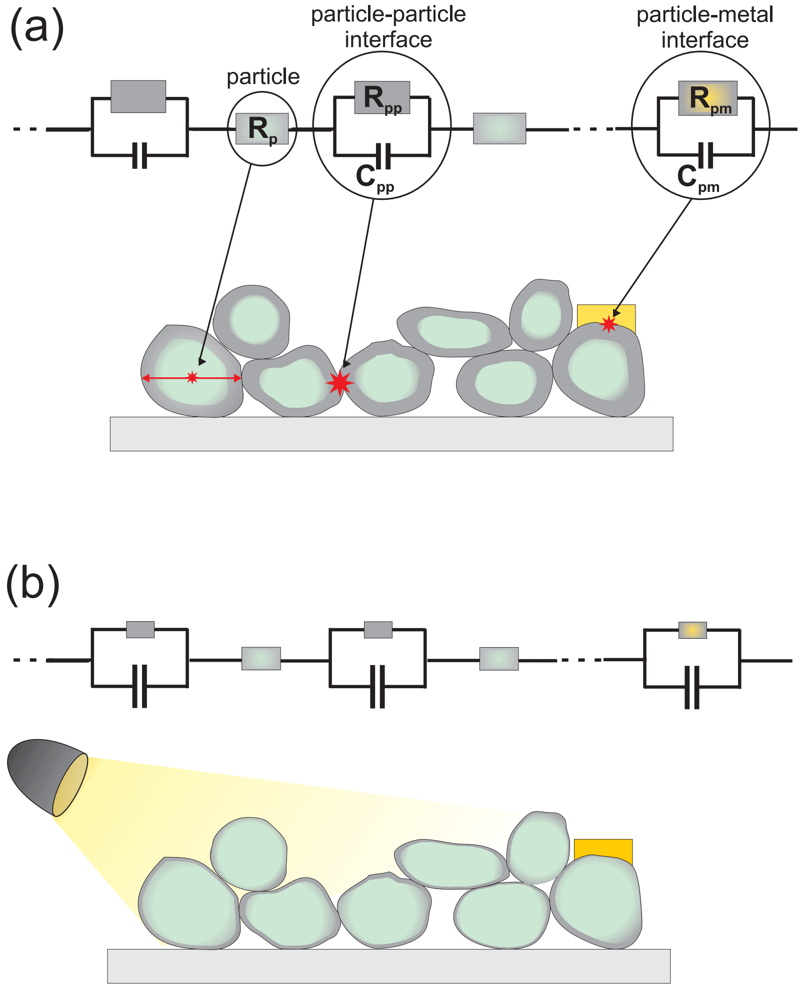

Figure 4.33: Equivalent circuit of a nanpowder sample (a) in darkness and (b) under UV illumination.

R_p stands for the bulk resistances of the ZnO particles, while R_{pp} and C_{pp}, which are arranged in parallel configuration, represent the particle-particle contacts. R_{pp} symbolizes the resistance of the highly resistive depletion layer (grey color) while C_{pp} denotes the capacitance arising from the depletion layer sandwiched between the conductive bulk material (dark gray color). R_{pm} and C_{pm} denote the resistance and capacitance at the particle-metal Schottky contact. Note that for simplification only one electrode is shown.

In darkness, adsorption of oxygen molecules at the grain surfaces leads to the creation of potential barriers and extended depletion layers (broadened grey region) at the intergranular contacts [129], resulting in large R_{pp} and small C_{pp} as shown in Fig. 4.33(a). Under UV light, desorption of oxygen from the particles surfaces takes place leading to a decreased width of the depletion layer, smaller resistances R_{pp} and larger capacitances C_{pp} at the particle-particle interfaces. The surface barriers are therefore diminished which results in an enhanced current flow under UV illumination. Due to the photogeneration of additional carriers, the bulk resistance of the particles R_p will also decrease.

Using the same terminology as in Chap. 4.5.6, the core-shell ratio for the ZnO nanopowders is by far larger than the ratio for a single nanowire. Therefore, the modification of electrical properties upon illumination and changes in ambient conditions will be larger. Note that changes in the gas atmosphere will have a strong impact on R_{pp} and C_{pp} and will also influence R_{pm} and C_{pm}, while R_p will hardly be affected.

Influence of ambient conditions

In order to investigate the influence of different atmospheres, photoresponse measurements of layers consisting of loosely connected ZnO nanopowders were performed in various ambient conditions. Figure 4.34(a) shows the behavior of the nanocrystals in different atmospheres in darkness and under illumination with UV light at 365 nm. The applied voltage was held constant at 10 V. Figure 4.34(b) displays the corresponding photocurrent decay times.

Independent of atmospheric composition, the dark current is below the detection limit of the picoamperemeter as Fig. 4.34(a) shows . Under UV irradiation, the current increases up to nearly six orders of magnitude, where the largest gain is observed at a pressure of around 0.5 mbar (from here on it will be denoted as ”vacuum”) and the lowest in air. Note that for security reasons, the measurement labeled with ”H_2” was performed under a hydrogen pressure (low-pressure) of only 700 mbar in order to prevent leaking of the hydrogen out of the gas chamber.

When comparing all measurements, the least increase in current is observed for oxygen containing atmospheres (air, O_2). Also the photocurrent decay is significantly faster in air (< 1 s) and in O_2-atmosphere (≈ 4 s) and longer in N_2, H_2 and vacuum, as

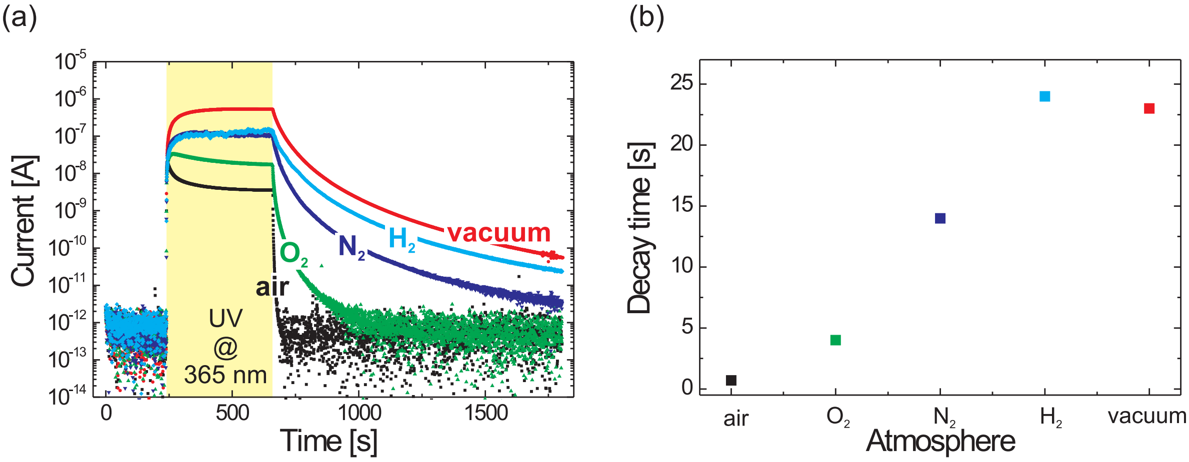

Figure 4.34: *(a) Influence of UV illumination on the conductivity of ZnO nanopowder layers measured in different atmospheres. Applied bias voltage was held constant at 10 V. (b) Deduced photocurrent decay times.*

Fig. 4.34(b) clearly reveals. These findings confirm the strong influence that oxygen has on the resistances of ZnO nanostructures and hence fit well to the dynamic core-shell model presented in Fig. 4.15.

The differences in photoresponse and decay times might also be due to changes in the relative humidity (r. h.) for the different atmospheres, but no variation in humidity was observed between oxygen and nitrogen atmosphere. For both about 5 % r. h. was detected (within the error of measurement).

Even though oxygen has a lower partial pressure in air than in pure O_2-atmosphere, the observed photoresponse in air is smaller and the photocurrent decay time larger than in (dry) oxygen atmosphere. This indicates that besides oxygen adsorption/desorption, another mechanism has to be involved. A factor playing a significant role in the decay of photoconduction is the influence of water vapor which is known to be a major contaminant in air [130].

Also, the change of the photocurrent under varying pressure was investigated in a single measurement. Figure 4.35 displays the measured current in darkness and under UV illumination in air and in vacuum. Furthermore, the gradient of the relative humidity is displayed.

The increase of photocurrent under UV illumination was already extensively described above. However, the additional conductance increase when the chamber is evacuated can not be simply explained by the change in oxygen partial pressure. The bonds of oxygen

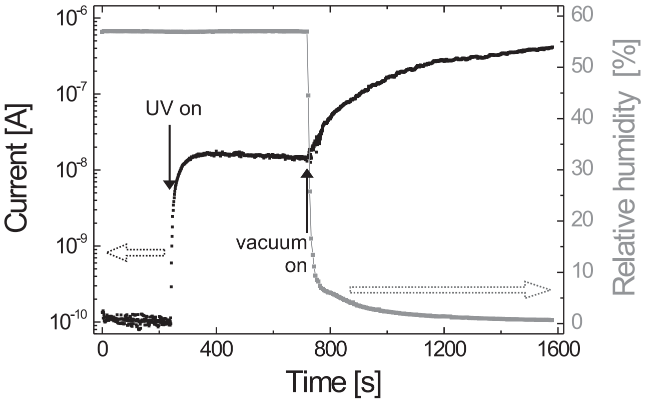

Figure 4.35: *Photocurrent of ZnO nanopowder layers in air and in vacuum (black dots) and the change in humidity upon evacuation of the gas chamber (grey dots).*

with the defect sites are stable at room temperature and the vacuum state alone is not enough to break them [131]. In air, the relative humidity was determined to be about 55 % while in vacuum no water molecules are present. A further increase in current is detected resulting from the desorption of adsorbed water molecules on the ZnO nanoparticle surface [132]. In Chap. 4.5.6 it was stated that UV illumination generates electron-hole pairs; the holes migrate to the ZnO surface and neutralize the adsorbed oxygen molecules (see Eq. (4.15)). However, a more complex mechanism has to be involved as schematically illustrated in Fig. 4.36.

In darkness, mostly oxygen molecules are adsorbed on the nanowire surface (see Fig. 4.36(a)). Under UV illumination, the photogenerated holes may not only neutralize the oxygen molecules but may also react with lattice oxygen leading to the formation of doubly ionized surface oxygen vacancies V_O^{2+}

$$O^{2-} \rightarrow \frac{1}{2}O_2 + V_O^{2+} + 2e^- \tag{4.20}$$

while electrons may react with lattice zinc ions (Zn^{2+})

$$Zn^{2+} + e^- \rightarrow Zn^+ \tag{4.21}$$

to form Zn^+ which will immediately react with oxygen molecules adsorbed on the surface [133]. It can be concluded that steady illumination with UV light leads to an enhancement of the number of surface defects sites (see Fig. 4.36(b,c)). According to Eq. (4.20), the formation of oxygen vacancies should result in two additional free

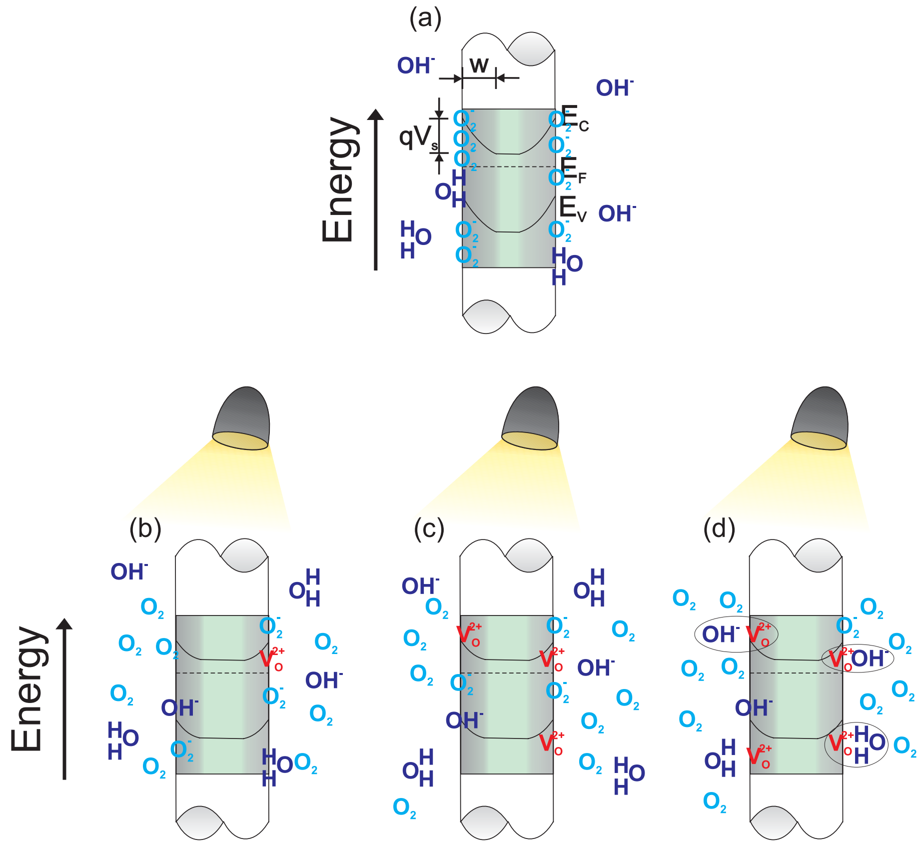

Figure 4.36: *Expanded core-shell model taking into account the formation of oxygen vacancies during steady UV illumination and the influence of water molecules present in the atmosphere. (a) State of the ZnO nanostructure under dark conditions and (b-c) modification of surface states and band bending effects under continuous illumination with UV light.*

electrons and therefore an increase in photocurrent. It is known however, that water molecules favorably adsorb on those kinds of defects as shown in Fig. 4.36(c). This happens either by chemisorption (hydroxyl groups adsorbed on the defective sites) or by physisorption, where polar water molecules bind to the surface defects. Therefore, in water vapor containing atmospheres like air, water and oxygen compete to dissociatively adsorb on surface defective sites. In the adsorption process they capture electrons of the semiconductor which leads to a decrease in photocurrent despite continuous UV illumination, as observed in the measurement performed in air as shown in Fig. 4.34.

Additionally, measurements in artificially synthesized air consisting of 80 % N_2 and 20 % O_2 (pressure 1 bar) and varying humidity were performed by A. Wagner, Institute of Semiconductor Technology. The relative humidity was changed from 5 % to 80 %. The obtained results are displayed in Fig. 4.37.

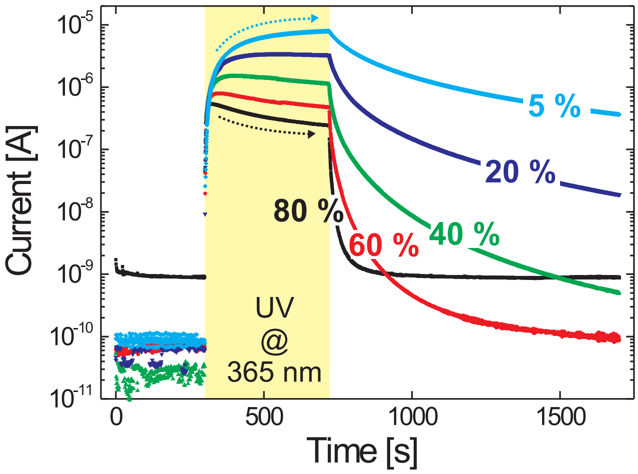

Figure 4.37: *Influence of the relative humidity on the electrical conductivity of ZnO nanopowder layers.*

The lower the humidity in the synthesized air, the larger the increase in current upon UV illumination and the slower the photocurrent decay times when the light is turned off. Furthermore, in humid air (for example 80 % r. h.), the photocurrent decreases even under continuous illumination as indicated by the black dotted arrow, while a further increase in photocurrent is noticed for the measurement performed in dry air (5 % r. h., see gray dotted arrow). These results confirm that besides the impact of oxygen on the electrical transport characteristics, also water vapor significantly influences the electrical transport properties of ZnO.

The high current detected in darkness at a humidity of 80 % does not originate from the sample, but is merely a measuring artifact: At such a high humidity, a water film formed on the vacuum lead-through short-cuts the measurement and leads to distorted results.

Sun *et al.* and Feng *et al.* studied the surface wettability of ZnO films and nanowires [133, 134]. They were able to convert the ZnO surfaces from highly hydrophobic to highly hydrophilic by illumination with UV light, and to re-establish their original state by storing the sample in darkness. Their results confirm the correlation between UV illumination and water adsorption and furthermore indicate that hydroxid adsorption is kinetically more favorable than oxygen adsorption. However, adsorption of OH^- molecules (hydrophilic ZnO surface) leads to a distortion in electronic and geometric structure and is therefore energetically unstable as compared to the hydrophobic state. Consequently, in darkness and in an oxygen containing atmosphere, the adsorbed OH^- groups are gradually replaced by oxygen molecules leading to a thermodynamically preferred state [133].

In summary, it was shown that ambient conditions like illumination, but also oxygen or water vapor present in the atmosphere, severely influence the electrical transport properties of ZnO. The effects are especially pronounced on ZnO based nanostructures like nanowires and nanopowders, due to their enormous surface to volume ratios. Since the nanoparticles and nanowires under investigations did not show any distinct dominant facets, no conclusions can be drawn concerning the influence of the ambient conditions on the differently oriented surfaces.

The results show that ZnO based nanostructures are complex systems and that their electrical transport characteristics are difficult to characterize since many factors influence the results. The overview of resistivity data obtained from measurements on VPT grown nanowires and values taken from various publications reveal that if ZnO nanowires should serve as active elements in gas sensing and UV detecting applications, they should be contacted using large-scale production compatible techniques already in the test stage, since contact resistances might have an impact on the result. Additionally, due to unwanted side effects that can strongly influence the desired response, devices should be characterized under real conditions and not only in a laboratory environment.

From a more optimistic point of view, the large range of observed conductivities (10^{-3} Ωcm to nearly 10^{5} Ωcm) for the ZnO nanowires can be seen as a chance for the tuning of the electrical properties on a large scale and the strong effect of ambient conditions on the transport characteristics provides an excellent basis for the use of ZnO based nanostructures in gas, humidity and UV sensing applications.

Chapter 5

Magnetic nanosystems

In his speech about miniaturization in 1959, R. P. Feynman was not only challenging the audience to build computers with wires having diameters between 10 nm and 100 nm, but also to use systems involving quantized energy levels or the interaction of quantized spins [12]. However, until recently, mainstream electronics was only exploiting the charge of the electrons while their other degree of freedom, namely the angular momentum or spin, was ignored. First steps to make use of the spin were taken in 1988/89 by Fert [135] and Grünberg [136] who discovered the giant magnetoresistance (GMR) effect in which the charge as well as the spin of the electron is exploited[1]. Today, information technology is split into two sections: Information processing is based on conventional electronics employing semiconducting charge-based devices while for data storage metal-based spin-dependent devices are employed (magneto-electronics). The technology combining both, conventional and magneto-electronics, is commonly referred to as ”spintronics”.

In quest of materials for spintronic applications, diluted magnetic semiconductors (DMSs) recently attracted much attention due to their potential for combining semiconducting and magnetic features in a single material. The use of DMSs would also simplify the integration of magnetic modules into already existing semiconducting processing technologies. Advantages of this kind of new devices would be nonvolatility, increased data processing speed, decreased electric power consumption and increased integration densities as compared to conventional semiconducting devices [137]. Some even believe that *”quantized spins in quantum dots may prove to be the holy grail for quantum computing”* [138].

Potential applications of ferromagnetic DMSs are electrically controlled magnetic sensors and actuators, devices combining magnetic, electronic and optical functionality as well

---

[1] For their discovery they were awarded the Nobel prize in physics in 2007.

as spin-polarized light emitters. Especially for the latter, the challenge lies not only in achieving coherent spin injection, but the device dimensions also have to be sufficiently small - smaller than the spin-coherence length. Therefore, magnetic nanoparticles and nanowires seem to be particularly suitable for those kind of devices. Additionally, charge carriers are confined in the radial direction of the nanowires resulting in high carrier concentrations that are required to achieve ferromagnetic coupling.
At this stage, one of the major challenges lies in designing a ferromagnetic material with a Curie temperature above room temperature whose magnetic properties can be controlled electrically and vice versa. There are a number of possible candidates that might fulfill the requirements. Of the III-V and II-VI compound semiconductors, interest is particularly focused on ZnO doped with $3d$ transition metals (TMs).

In the following section, the basic principles of magnetism in solid states are described with a special focus on the ferromagnetic coupling. Subsequently, the ferromagnetism in semiconductors is discussed and results concerning magnetic properties investigations of ZnTMO are presented.

5.1 Magnetism in solid states

Magnetism originates from the orbital and spin motions of the electrons and their mutual interactions. While in some materials there is a strong coupling between the magnetic moments of the atoms (resulting in ferro-, ferri or antiferromagnetic features), for dia- and paramagnetic samples there is no collective interaction of the atomic magnetic moments.

The magnetization $\vec{M}$ of the medium is defined by the material's respond to an applied magnetic field of strength $\vec{H}$ according to

$$\vec{M} = \chi \vec{H}, \tag{5.1}$$

where χ denotes the magnetic susceptibility.

5.1.1 Diamagnetism

Diamagnetism is a property that is present in all materials; however, only systems whose diamagnetic properties are not superimposed by paramagnetism or collective magnetism (like ferro-, ferri- or antiferromagnetism) are denoted as diamagnets.

Diamagnetic solids have no net magnetic moment per atom as a result of their shells being filled. The diamagnetic susceptibility arises from the change in electron orbitals caused by the external magnetic field $\vec{H}$ which leads to a weak magnetization of the material. The induced magnetization opposes the direction of $\vec{H}$, so χ_{dia} is negative and typically ranges between -10^{-6} and -10^{-5},while the value does not depend on temperature.

5.1.2 Paramagnetism

In paramagnetic materials, the atomic magnetic moments that result from unpaired electron spins are only weakly coupled to each other, therefore thermal energy already leads to the random alignment of the atomic moments. When an external magnetic field is applied, the orientation of the magnetic moments shifts slightly towards the direction of the field lines resulting in a positive value of the susceptibility. The susceptibilities of paramagnets range between $10^{-5} \leq \chi_{para} \leq 10^{-3}$ and are inversely proportional to temperature.

The magnetic moment μ of an isolated atom or ion is given by

$$\vec{\mu} = g\mu_B\vec{J}, \tag{5.2}$$

where g represents the Lande splitting factor, μ_B the Bohr magneton and $\vec{J}$ the total angular momentum which is the sum of the atomic spin and the atomic orbital angular momentum. The energy of the magnetic dipole under the action of a magnetic field ($\vec{H}$=(0,0,H)) then results in

$$E_j = -\mu_0\vec{\mu}\vec{H} = -\mu_0 g\mu_B m_j H. \tag{5.3}$$

m_j represent the total magnetic quantum number that can take values between -J, -$J+1$, .., J and μ_0 denotes the permeability of free space. The magnetization of a paramagnetic material is given by the sum over all magnetic moments

$$M = N\langle\mu_z\rangle = N\sum_j \mu_{z,j}p_j, \tag{5.4}$$

where p_j denotes the probability that a system is in the energy state E_j. Accoring to Boltzmann statistics it is given by

$$p_j = \frac{e^{-\frac{E_j}{k_BT}}}{\sum_j e^{-\frac{E_j}{k_BT}}}. \tag{5.5}$$

With $\mu_{z,j} = -g\mu_B m_j$ and p_j from Eq. (5.5), the magnetization then yields

$$M = NgJ\mu_B B_J\left(\frac{gJ\mu_B\mu_0 H}{k_BT}\right), \tag{5.6}$$

where $B_J(x)$ is the Brillouin function which is defined as

$$B_J(x) = \frac{2J+1}{2J}\coth\left(\frac{2J+1}{2J}x\right) - \frac{1}{2J}\coth\frac{x}{2J}. \tag{5.7}$$

5.1.3 Ferromagnetism

The most important kind of magnetic materials are ferromagnetic solids whose susceptibility χ_{ferro} are positive and by far greater than unity. χ_{ferro} may take values from 50 to 10000, the values decrease with increasing temperature. Ferromagnetism (as well as antiferro- and ferrimagnetism) occurs because of the exchange interaction between permanent magnetic moments. Below a certain temperature that is denoted as Curie-temperature (T_C) for ferro- and ferrimagnetic solids and Néel-temperature (T_N) for antiferromagnets, the atomic magnetic moments couple with each other which leads to a spontaneous magnetization of the material. At temperatures exceeding T_C (or T_N, respectively), the systems become paramagnetic.

Figure 5.1 shows a typical magnetization curve (hysteresis loop) of a ferromagnetic material. While the sample is not magnetized in its initial state (at $\vec{H} = 0$), the application of an external field causes the magnetization to increase in field direction. If $\vec{H}$ is sufficiently increased, the magnetization will nearly saturate corresponding to the state when all magnetic dipoles are aligned parallel to $\vec{H}$. Once the material has been magnetized, a remanent magnetization M_r remains, even if $\vec{H}$ is reduced to zero value. The field strength in opposite direction that is required to reduce the magnetization down to zero value is denoted as coercivity field strength. χ_{ferro} is therefore not only a function of temperature but also depends on the history of the sample.

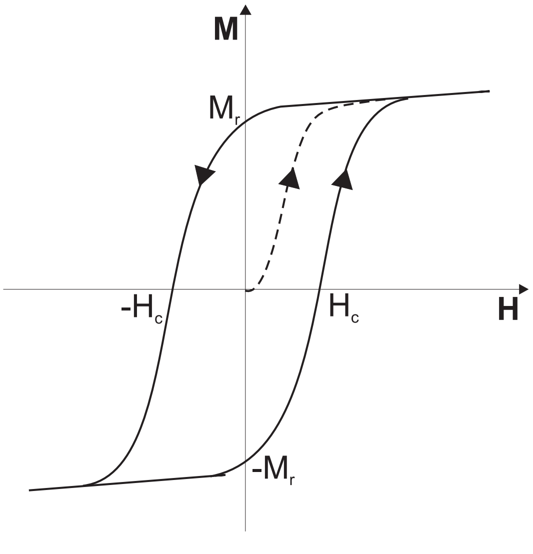

Figure 5.1: *Magnetization curve of a ferromagnet.*

Collective magnetism requires an interaction between the magnetic moments. However, since electrons are fermions and as a consequence of the Pauli exclusion principle, the total electronic wavefunction of a system must be antisymmetric with respect to the interchange of two electrons. Using the Heisenberg-model, the corresponding Hamilton operator then yields

$$\widehat{H} = \sum_{ij} A_{ij} \vec{S}_i \vec{S}_j, \tag{5.8}$$

where A_{ij} denotes the exchange integral between the spins $\vec{S}_i$ and $\vec{S}_j$. For $A > 0$ the spins are in parallel configuration (ferromagnetic ordering), while for $A < 0$ the spin alignment is antiparallel resulting in antiferromagnetic features.

Coupling between magnetic moments can either happen by direct or by indirect exchange interaction. Direct exchange requires an overlap of the wavefunctions of neighboring magnetic atoms, which is commonly (if at all) negligibly small. More important are indirect exchange mechanisms. For example in ionic crystals like MnO, no direct coupling between the transition metal ions is possible. However, interactions between the Mn^{2+} can be mediated by the intermediate non-magnetic O^{2-} anions; such a coupling mechanism is denoted as superexchange. Superexchange commonly leads to antiferromagnetism. In addition to direct and superexchange that can also occur in insulators, there are also carrier-mediated exchange mechanisms. Here, the interaction between localized magnetic moments is mediated by free carriers in the crystal. In metals, a long-range interaction of the magnetic ions can also occur via non-magnetic conduction electrons: A localized magnetic ion polarizes the surrounding delocalized conduction electrons which can transfer their polarization to other magnetic ions. This kind of coupling mechanism is referred to as RKKY after Ruderman, Kittel, Kasuya and Yoshida [139]. Depending on the distance between the magnetic ions, the interaction can either be ferro- or antiferromagnetic. In systems with both local magnetic moments and itinerant electrons or holes, the carriers are able to mediate a ferromagnetic coupling between the magnetic moments. This mechanism is known as Zener carrier-mediated exchange [140].

Additionally, another exchange model exists which explains the experimentally observed ferromagnetism in doped perovskite structure manganites $La_{1-x}Sr_xMnO_3$ (0 ¡ x ¡ 1). The magnetic ions in mixed valence crystals can have different valencies, they can be either incorporated in the Mn^{4+} or in the Mn^{3+} state. Electron hopping processes between these states lead to ferromagnetic coupling known as Zener double exchange [141]. This indirect exchange is also mediated by oxygen atoms, but in contrast to superexchange, also carriers are involved.

5.2 The diluted magnetic semiconductor Zn(TM)O

In DMS systems, some of the non-magnetic cations of the host semiconductor are substituted by magnetic transition metal ions (like V, Co, Mn ..) that induce paramagnetic contributions because of their unfilled $3d$-shells. If the magnetic ions additionally interact with each other, spontaneous magnetization occurs and the sample might exhibit ferromagnetic properties.
There are different classes of exchange interactions in ZnO based DMS structures: antiferromagnetism is observed if transition metal ions couple via superexchange, while ferromagnetism occurs if the interaction between the magnetic atoms is carrier mediated. Therefore, ferromagnetism in semiconductors not only depends on the magnetic dopant concentration but also on the charge carrier type and density.

In recent years, much attention was given to the investigation of Zn(TM)O as a ferromagnetic DMS due to the theoretical calculations by Dietl *et al.* [8]. The authors evaluated the Curie temperatures for various semiconductors by applying Zener's model for ferromagnetism that is driven by the exchange interaction between carriers and localized spins [140]. They predicted that ZnO doped with 5 at.% Mn^{2+} and containing 3.5 x 10^{20} holes/cm^3 should exhibit ferromagnetism with T_C exceeding 300 K. Unfortunately, p-type doping of ZnO, especially in such high concentrations, is difficult to achieve. Sato and Katayama-Yoshida used *ab initio* calculations based on the local density approximation to theoretically investigate the magnetic properties of transition metal doped ZnO [9]. Again, their results suggested that ferromagnetism in ZnMnO is only mediated by holes, while for Mn incorporated into n-type ZnO, they predicted an antiferromagnetic coupling. However, for ZnXO (X = V, Cr, Fe Co and Ni) they expect a ferromagnetic ordering even without any additional p-type doping. The magnetic properties of ZnO doped with transition metals have been extensively studied within the last years; yet, there are still considerable discrepancies in the experimental results reported in the literature.

5.3 Experimental techniques

In most investigations concerning the magnetic properties of the ZnTMO layers and nanostructures, a SQUID (superconducting quantum interference device) magnetometer was employed. However, SQUID is a volume sensitive measuring technique that averages all magnetic contributions. For example, Mofor *et al.* observed a critical influence of the sapphire substrate which strongly affected the magnetic property measurements [142]. Therefore, also local probe techniques should be employed in order to clearly confirm ferromagnetism in ZnTMO. In this work, SQUID and MFM measurements served as the main characterization methods. They are shortly described in the following paragraph.

5.3.1 SQUID magnetometry

Figure 5.2 depicts a schematic image of the inner chamber of a magnetic property measurement system (MPMS). The set-up mainly consists of the sample rod, a superconducting solenoid to produce the magnetic field that serves to induce a magnetic moment to the sample, an array of superconducting pick-up coils and an input coil. Additionally displayed is the magnetically shielded SQUID detector. A SQUID consists of a superconducting ring interrupted by an electrically normal conducting or even insulating material, a so called Josephson contact. This intermediate layer has to be sufficiently thin to allow tunneling of the cooper pairs. The detection coils, the connecting wires and the input coil are connected in such a way that they form a closed loop.

Since the magnetic field in the inner part of a superconductive ring can only take discrete values (flux quantization), a variation of the field strength results in a current flow to screen the magnetic field in order to guarantee that the flux is still quantized.

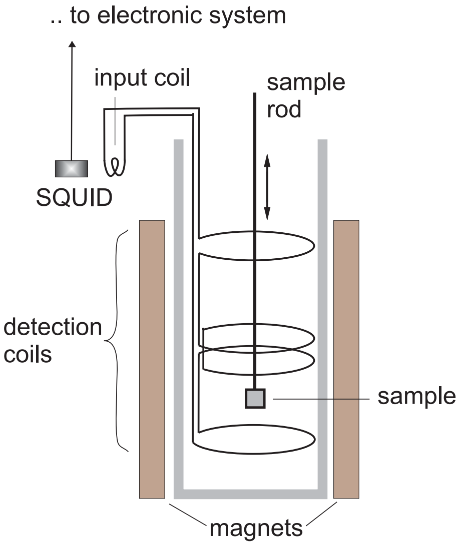

Figure 5.2: *Inner chamber of the magnetic property measurement system.*

The sample is mounted onto the movable sample rod and magnetized by the applied magnetic field. Depending on the orientation of the sample on the holder, the magnetization can either be in plane ($\vec{H} \parallel$ sample) or out of plane ($\vec{H} \perp$ sample). The magnetic moment of the sample is measured by stepping the sample through the array of the detection coils. It induces a current flow in the detection coils and consequently in the input coils which inductively couples to the SQUID detector. The SQUID therefore experiences the same flux change as the detection coils which results in a change in the output voltage. The advantages of the SQUID characterization method lay in its high sensitivity and accuracy. In this work, a Quantum Design MPMS was used to characterize the ZnTMO samples. The system was provided by the Physikalisch Technische Bundesanstalt, Department 2.51. Measurements were performed at temperatures from 5 K to 300 K, while the applied field varied from - 20 kOe to 20 kOe (corresponding to - 2 T to 2 T).

5.3.2 Magnetic force microscopy

Magnetic force microscopy (MFM) is a variation of atomic force microscopy (AFM). In AFM mode, interest is focused only on the topography of the sample, while MFM measurements record the magnetic stray fields emerging from the sample. Figure 5.3 illustrates the working principle of a MFM set-up operated in constant height mode.

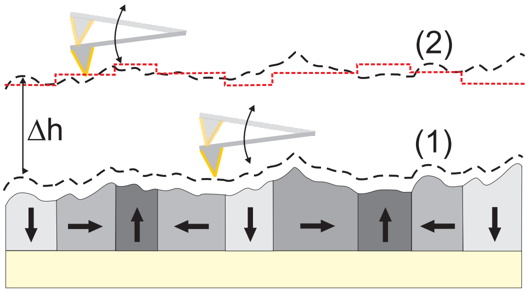

Figure 5.3: *Functional principle of a MFM measurement operated in constant height mode. In the first pass (1), the topography of the sample is measured (dashed black line). In the second pass, the tip is lifted by* Δh *and the topography is retracted. Due to the magnetic interaction between the tip and the magnetic stray signals emerging from the sample are detected.*

Each line of an image is scanned twice. In the first run, the topography of the sample is determined. The tip is in close proximity to the surface and short-reaching van der Waals forces dominate the spectra (see (1) in Fig. 5.3). In the second scan, the tip is lifted up to a predefined height and the contours of topography are retraced, so the tip-sample distance is constant at all times. Typical lift heights vary from 50 nm to about 200 nm. Since surface forces are of short range, only further reaching magnetic signals emerging from the sample are detected.

The tip is coated with a ferromagnetic layer and the force between the tip and the sample depends on the gradient of the magnetic stray field ($\vec{H}$) according to [143]

$$\vec{F} = (\vec{m}_{tip}\vec{\nabla})\vec{H}, \tag{5.9}$$

where $\vec{m}_{tip}$ denotes the magnetic moment of the tip. The magnetic field - tip interaction leads to a change in the resonance frequency, the corresponding signal is indicated by the dashed red line (see (2) in Fig. 5.3).

All measurements were performed at room temperature and in air.

5.4 ZnO:Mn nanostructures

Among the research on ZnO doped with transition metals, interest is focused on ZnMnO in particular. Mn in the Mn^{2+} easily substitutes Zn ions. It is electrically neutral in ZnO and the ionic radii of Mn^{2+} is relatively close to the one of ZnO (0.66 Å and 0.60 Å, respectively [144]). Therefore it can be incorporated up to very high amounts (approximately 35 %) without disturbing the symmetry of the wurtzite crystal structure [145]. Mn in ZnO is not only a good candidate due to the high doping concentrations that can be achieved, but compared to V, Co, Fe, Ni etc, it also exhibits the maximum magnetic moment: the Mn $3d$ shell is exactly half-filled with all spins in parallel alignment according to Hund's rule which results in a maximum magnetic moment of $J=S=5/2$.
Even though the magnetic properties of Mn doped ZnO films and nanostructures were already extensively and thoroughly studied, the published reports are still quite contradictory. While some authors claim to have evidence of the existence of room-temperature ferromagnetism [146, 147], others detected antiferromagnetic [148, 149] or paramagnetic [150–152] features in the material. The Mn doped ZnO samples were mostly grown employing complex and expensive techniques like molecular beam epitaxy, metalorganic vapor phase epitaxy or pulsed laser deposition, growth methods that require high temperatures. In contrast to these approaches, conventional material processing by pressing and sintering of powders is a simple and cost-effective technique.
In this work, commercially available Mn doped ZnO nanopowder was investigated concerning its magnetic properties and its applicability for the fabrication of devices utilizing the magnetoresistive effect. The high-purity ZnO:Mn powder (3.3 at.%) was obtained from Umicore Zinc Chemicals. Besides the structural and magnetic properties of the ensemble of powder particles, the nanochemical composition of individual grains is also emphasized.

5.4.1 Structural properties

Figure 5.4(a) displays a representative SEM micrograph of compressed ZnO:Mn nanopowder and Fig. 5.4(b) displays the corresponding TEM bright-field (BF) image. Specimen for TEM characterization were prepared by dispersing powder particles on a holey carbon filmed copper grid. The TEM measurements were provided by H. Schmid, University of Bonn.

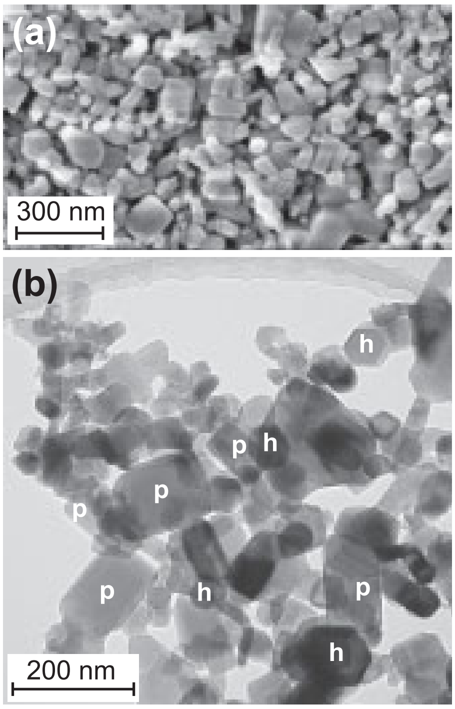

Figure 5.4: *Microstructure of ZnO:Mn nanopowder: (a) Scanning electron micrograph (SEM) and (b) TEM micrograph showing loosely aggregated powder ensemble supported on holey carbon film. Three types of particles are discernible: large platelets ("p"), hexagonal ("h") and irregular shaped particles. TEM images provided by H. Schmid, University of Bonn.*

Three types of particles classified by their morphology are discernible: The majority (approximately 81 %) of particles are irregularly shaped with diameters ranging from 20 to 80 nm, but also larger rectangular-shaped platelets up to $\approx$ 200 nm in size are observed (about 7 %). The platelets are labeled with "p". About 11 % of all nanocrystals exhibit clearly facetted hexagonal shapes, those are labeled with "h". Independent of their contours, all three types of particles are shaped as thin platelets as the linear behavior of cumulative amplitude contrast (absorption) in overlapping particle regions clearly indicates.
The XRD spectra displayed in Fig. 5.5 reveals that the ZnO:Mn nanopowder is of wurtzite crystal structure. Additionally displayed are the peak positions of a simulated XRD scan of randomly oriented wurtzite ZnO powder. XRD data was provided by H. Bremers, Technical University Braunschweig.

Figure 5.6 depicts the photoluminescence spectrum of the Mn doped ZnO nanopowder taken at a temperature of 15 K using a He-Cd laser with an excitation power of 10 mW

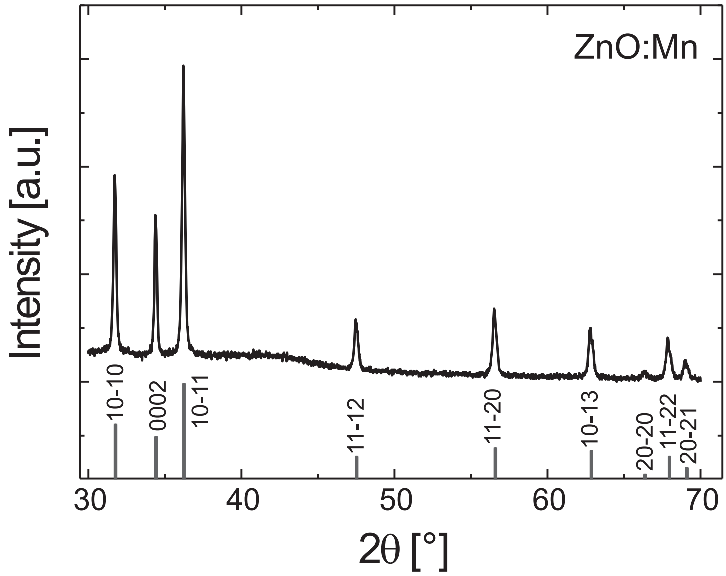

Figure 5.5: *$\theta - 2\theta$ XRD pattern of ZnO:Mn nanopowder. The bottom graph displays the peak positions of a simulated XRD scan of randomly oriented wurtzite ZnO powder.*

at a wavelength of 325 nm. Only ultraviolet near-band edge (NBE) emission of low intensity is detected. The NBE peak intensity is more than one order of magnitude lower than the signal observed for pure ZnO nanopowder (spectra not shown). The PL intensity decreases with increasing Mn concentration in accordance with earlier literature reports [153]. However, in contrast to the results of Roy *et al.* who observed an increased green luminescence with Mn incorporation [154], no PL emission in the visible range was detected. The most intense peak at 3.3605 eV is attributed to the A exciton bound to neutral donors (D^0X_A) [155]. The luminescence at 3.3724 eV is assigned to the B exciton bound to the same neutral donor (D^0X_B), since the energy seperation of 12 meV is consistent with the energy splitting of the A- and B-free exciton lines. On the high-energy side of the B exciton bound to neutral donor, the A-free exciton (FX$_A$) was observed at 3.3776 eV. The longitudinal optical (LO) phonon replica 1LO-FX_A and 2LO-FX_A are detected at 3.306 eV and 3.2336 eV, respectively. PL measurements were performed by M. Al-Suleiman, Institute of Semiconductor Technology.

5.4.2 Chemical composition

In order to check the chemical composition of the powder particles, microanalysis by energy dispersive X-ray spectroscopy (EDS) and electron energy loss spectroscopy (EELS) were conducted. Figure 5.7(a) depicts the TEM-BF image of an ensemble of powder particles. The distribution of constituent elements O, Mn, Zn was qualitatively assessed

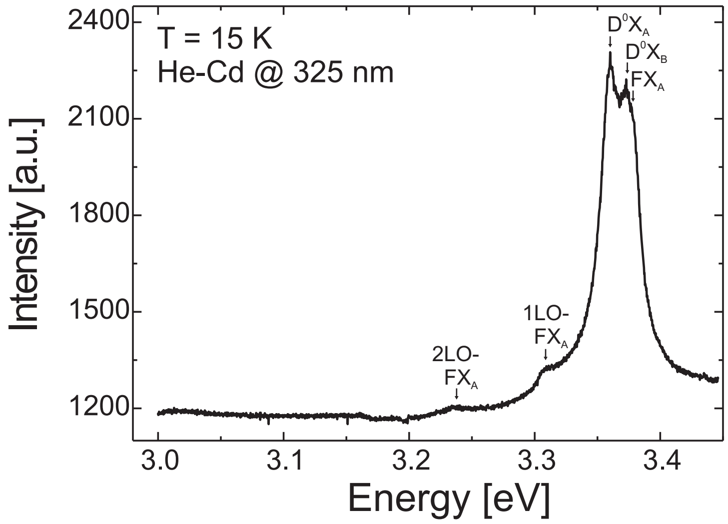

Figure 5.6: *Photoluminescence spectrum of ZnO:Mn nanopowder at 15 K.*

by EDS mapping in STEM mode (Fig. 5.7(b to d)). The analysis was performed by H. Schmid, University of Bonn.

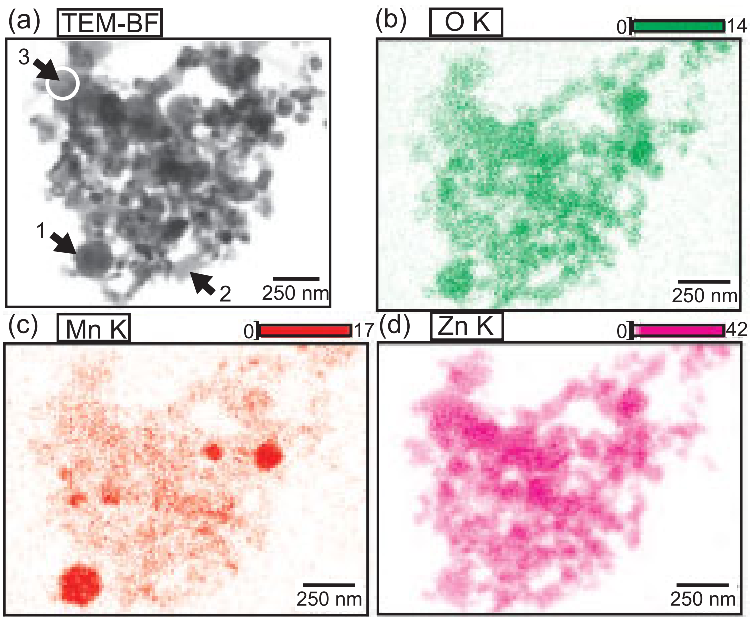

Figure 5.7: *Morphology and composition of ZnO:Mn nanopowder: (a) TEM bright-field image showing loosely aggregated ensemble of powder particles. (b-d) Element maps acquired by EDS in STEM showing distribution of O, Mn and Zn.*

The mapping reveals an inhomogeneous distribution of elements with Mn preferentially concentrated in the hexagonal shaped particles (Fig. 5.7(c)), whereas the Mn signals from the larger rectangular shaped particles are rather low. Relative concentrations (normalized to 100 at.% cations) were measured in selected regions by quantitative EDS analysis within the limits of the standardless thin film approximation [156]. A high cation ratio Mn : Zn $\approx$ 1 : 2 was measured in hexagonal particles (e.g. particle 1), whereas analyses in larger platelets (e.g. particle 2) yielded rather low Mn concentrations at the detection limit $\leq$ 1 at.% Mn. Spot analyses in regions containing only small irregular shaped particles (e.g. region 3) yielded cation concentrations between 2 and 3 at.% Mn.

These findings are supported by EELS measurements with its inherently high spatial resolution capability in the nm range. The obtained spectra are displayed in Fig. 5.8. The Mn-L ionization edge is clearly observed in the spectra acquired from hexagonal shaped particles, whereas no Mn signal is detected in spectra from large platelet-shaped crystals.

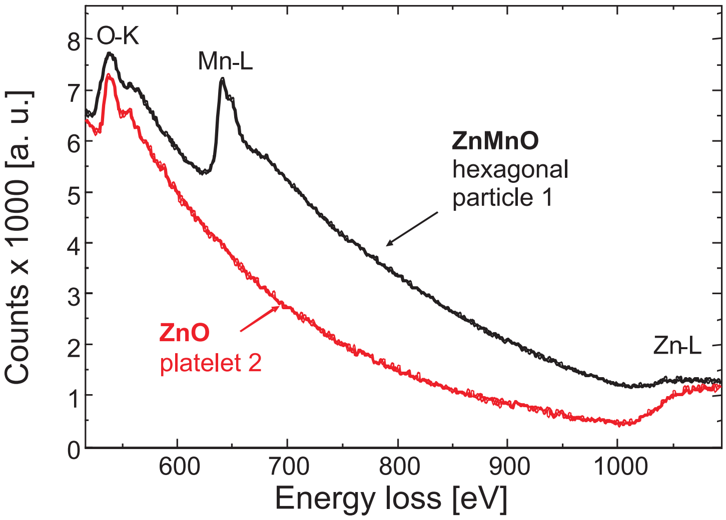

Figure 5.8: *EEL spectra from particle (1) and (2), as indicated in Fig. 5.7(a).*

5.4.3 Magnetic properties

The magnetic properties of the ZnO:Mn powder were analyzed by SQUID and MFM. For SQUID magnetometry, the nanoparticles were embedded in (non-magnetic) epoxy resin. Magnetization curves M(H) were measured at 5 K and 300 K, the applied field H ranging from -20 kOe to 20 kOe. Additionally, field-cooled M(T) measurements were performed from 300 K to 5 K. In order to obtain information on the magnetic properties of single particles, MFM images of compressed powder were taken.

Figure 5.9(a) shows the magnetization data at 5 K and 300 K. At low temperatures, the magnetic moment increases with increasing external field H indicating a paramagnetic behavior. According to Eq. (5.7) the data can be described by a Brillouin function, as can be seen by the added dashed red line. For $J = 5/2$, the theoretically expected value for Mn^{2+} (electronic configuration d^5), the curve given by Eq. (5.7) closely describes the magnetic behavior of the ZnO:Mn nanopowder. However, it should be pointed out that the displayed Brillioun function does not represent a fit to the measured data but is merely superimposed on the experimental values for demonstration purposes.

The magnetic moment per Mn atom could not be evaluated since saturation magnetization is not reached within the applied field strength of 20 kOe.

At 300 K only diamagnetic behavior is detected and the magnetic moment drops by one order of magnitude. For undoped reference ZnO particles, no difference is observed between the magnetization measured at 5 K and 300 K; both measurements revealed pure diamagnetic properties as shown in the inset of Fig. 5.9(a). The temperature dependence of magnetization of the ZnO:Mn sample in a field of 1000 Oe depicts Fig. 5.9(b). From 300 K to 75 K, the powder shows a diamagnetic behavior (negative magnetic moment). When the temperature falls below 70 K, the paramagnetic properties dominate and the magnetization increases. In this temperature range the measured magnetic moment μ can be described by the Curie law $\mu \propto 1/T$ (as displayed in the inset) thus indicating that at least some fractions of the sample material show paramagnetic behavior.

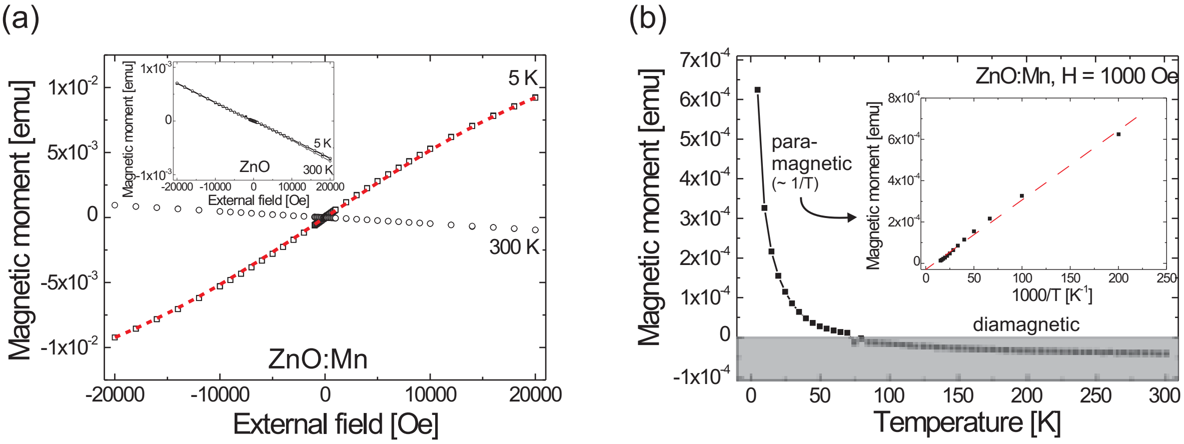

Figure 5.9: *(a) M(H) characteristics of the ZnO:Mn nanopowder at 5 K (squares) and 300 K (circles) measured by SQUID. The inset displays the results obtained for measurements of undoped ZnO reference material. (b) Magnetization vs. temperature M(T) curve measured in a field of 1000 Oe from 300 K to 5 K.*

From EDS and EELS analysis it is obvious that Mn concentrations vary in the different types of particles present in the ZnO:Mn nanopowder. While the apparently undoped large platelets might have little influence, both the low doped irregularly shaped and the highly doped hexagonal shaped particles are expected to contribute to the magnetic

behavior. SQUID measurements of the undoped reference sample revealed that pure in epoxy resin embedded ZnO nanopowder only exhibits diamagnetic properties. It can be assumed that the paramagnetic coupling is essentially due to the Mn atoms in both irregular shaped and hexagonal shaped particles.
Paramagnetism only dominates the magnetic properties in the temperature range below 70 K while at higher temperatures the diamagnetic contributions of the undoped ZnO crystals take over. Since SQUID is a volume sensitive measuring technique that averages the magnetic contributions of all particles, MFM measurements were performed to study the magnetic properties of individual grains.

Figure 5.10(a) displays the topography of the ZnO:Mn particles as scanned in AFM mode. The lift height for MFM image acquisition was set to 100 nm. In order to obtain magnetic contrast from the particles, the MFM tip was mounted onto an iron cantilever holder as shown in Fig. 5.10(b) and magnetized prior to measurement. The remanent magnetization of the whole holder yields approximately 2 to 3 Oe, however, taking into account the geometry of the structure, a stronger field occurs at the position of the MFM tip itself as seen by the accumulation of magnetic field lines in the centre of the tip assembly. Figure 5.10(c) depicts the corresponding MFM micrograph. As can be clearly seen, the MFM image is not just a copy of the measured topography but exhibits more complex features. Since surface forces are only of short range, the detected phase shifts can only be due to further-reaching magnetic signals emerging from the sample. A pronounced magnetic contrast is particularly visible in some particles, while for other grains no contrast is observed. These findings are consistent with the picture of an inhomogenous distribution of the Mn ions within the nanopowder as revealed by EDS and EELS measurements.

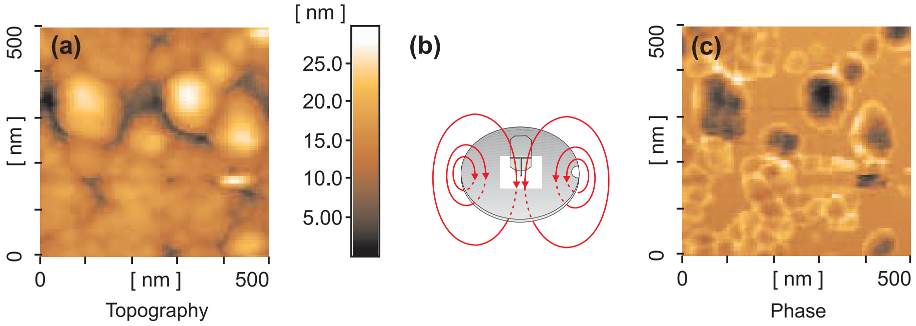

Figure 5.10: *ZnO:Mn nanopowder compact imaged by scanning probe microscopy: (a) Topography scanned in AFM mode; (b) geometry of magnetized tip holder with magnetic field lines; (c) magnetic structure imaged in MFM mode.*

Even though Mn was added up to high amounts into the ZnO nanocrystals, no ferromagnetic phase could be detected. It is therefore concluded that in order to obtain ferromagnetism in the ZnO:Mn system, additional doping to achieve p-type conductivity is needed which is in consistency with the theoretical predictions.

5.5 ZnO:Co nanostructures

Besides ZnO diluted with Mn, also Co doped nanoparticles were investigated regarding their structural and magnetic properties. Using Co as dopant instead of Mn seems to be advantageous, since for ZnO:Co a ferromagnetic behavior is expected even without any additional charge carriers [9]. However, also for this material composition the published results differ significantly. While some authors report of the successful fabrication of ferromagnetic ZnO:Co [157, 158], others found no evidence for a room-temperature ferromagnetic state [159, 160].

In this work, the properties of Co doped ZnO nanopowder were investigated. The nanopowder (4.5 at. % Co) was obtained from Umicore Zinc Chemicals.

5.5.1 Structural properties

Figure 5.11 displays a SEM and TEM image of the Co doped ZnO nanocrystals. The TEM image was provided by H. Schmid, University of Bonn.

The particles show three different types of morphologies: globular shaped particles (labeled with ”g”) with an average diameter of about 25 nm, particles shaped as rods (”r”) having dimensions of about 25 nm x 120 nm and larger platelets (”p”, 100 nm to 150 nm) that exhibit some distinct facets. No amorphous phase was detected.

XRD data proved that the ZnO:Co particles are also of wurtzite crystal structure; however, in contrast to the Mn doped nanopowders, no photoluminescence signal could be detected.

5.5.2 Chemical composition

Also for the Co doped ZnO powders, EDS mapping in STEM mode and EELS measurements were performed by H. Schmid, University of Bonn, in order to check the chemical composition of the nanocrystals. Figure 5.12(a) depicts the TEM-BF image of an ensemble of loosely agglomerated ZnO:Co particles, the element maps of the constituent elements O, Co, Zn acquired by EDS are displayed in Fig. 5.12 (b to d).

EDS measurements of the entire section displayed in Fig. 5.12(a) yield an average Co concentration of about 7 % (normalized to 100 at.% cations). However, extracted spectra

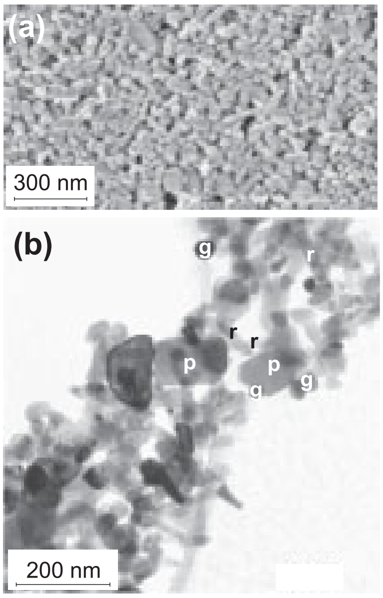

Figure 5.11: *Microstructure of ZnO:Co nanopowder: (a) Scanning electron micrograph and (b) TEM image showing loosely aggregated powder ensemble supported on holey carbon film. Three types of particles are discernible: globular shaped particles ("g"), larger platelets ("p") and particles shaped as rods ("r").*

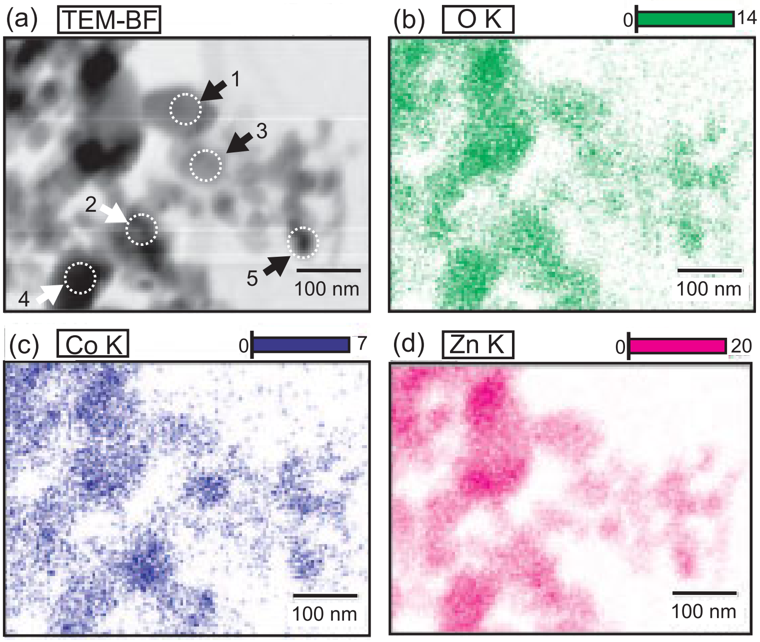

Figure 5.12: *Morphology and composition of ZnO:Co nanopowder: (a) TEM bright-field image showing a loosely aggregated ensemble of powder particles. Additionally marked are some selected regions where EDS spectra were extracted from. (b-d) Element maps acquired by EDS in STEM showing distribution of O, Co and Zn.*

of some selected regions labeled from 1 to 5 yielded Co concentrations of 3 %, 15 %, 19 %, 5 % and 11 % which means that they reveal an inhomogeneous distribution of the Co ions. But in contrast to the Mn doped sample, the local Co concentrations in the ZnO:Co nanopowder do not correlate with specific particle morphologies.

The inhomogeneous distribution of Co is also confirmed by EELS analysis as shown in Fig. 5.13. Even though in all spectra (acquired on different positions of the sample) a Co-L ionization edge was observed, the intensity of the Co signal varies. The average EELS spectra of a larger area (black graph in Fig. 5.13) yields a Co concentration of about 5 % which is in good consistency with the value determined by EDS. Spectra taken from the center of a medium sized particle (blue graph in Fig. 5.13) and between small particles (red graph in Fig. 5.13) give no indication of a core-shell structure of the nanocrystals. It is therefore concluded that Co is not only incorporated into the ZnO matrix, but that Co atoms also accumulate in different concentrations on the particle surfaces. They might exist as Co-rich clusters in the range of 1 nm that are non-resolvable by element mappings.

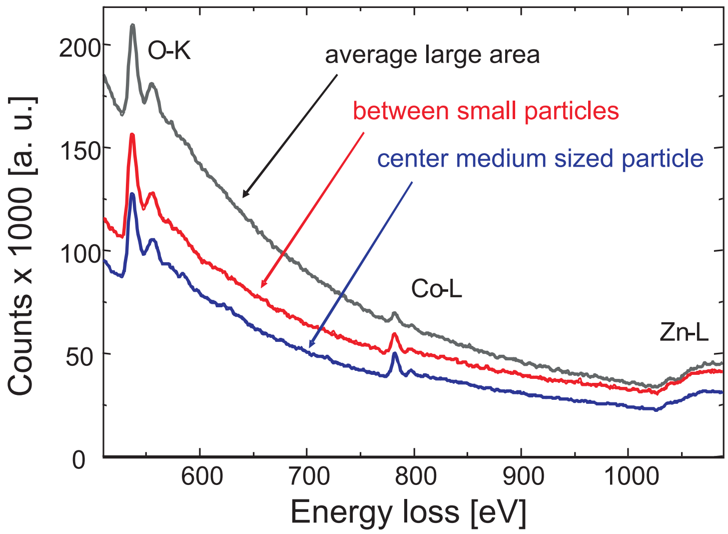

Figure 5.13: *EELS measurement performed at different positions of the ZnO:Co nanopowder: The black graph represents the average data acquired of a large area, while the red and blue graph corresponds to the spectra taken between smaller sized particles and in the center of a medium sized particle, respectively.*

5.5.3 Magnetic properties

The magnetic properties of the ZnO:Co nanopowder were also investigated by means of SQUID and MFM measurements. Figure 5.14(a) shows the magnetization data at 5 K and 300 K and Fig. 5.14(b) displays the temperature dependence of magnetization in a field of 1000 Oe . The characteristics strongly resemble the ones obtained for the Mn doped ZnO powder: At low temperatures, a paramagnetic behavior is detected and the data can be described by a Brillouin function (according to Eq. (5.7)), while at 300 K, the diamagnetic properties of the sample dominate the magnetization characteristics. The transition of the overall magnetic signal from para- to diamagnetic is also observable in the M(T) measurement. From 300 K to 75 K the ZnO:Co powder has a negative magnetic moment corresponding to a diamagnetic behavior, while at temperatures below 70 K, the paramagnetic properties dominate and the magnetization increases. The inset displays that for temperatures below 70 K the data can be described again by the Curie law ($\mu \propto 1/T$) which indicates a paramagnetic behavior.

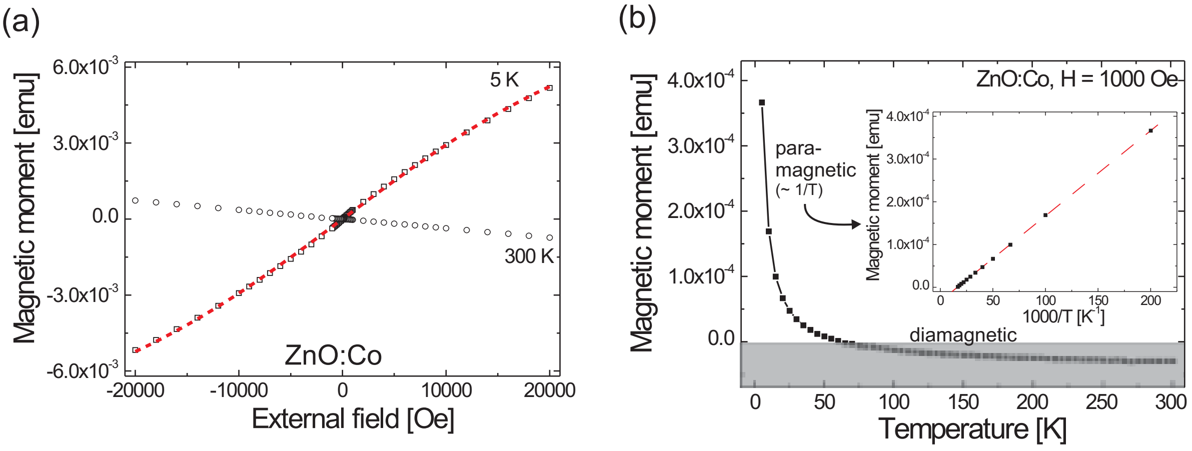

Figure 5.14: *(a) M(H) characteristics of the ZnO:Co nanopowder at 5 K (squares) and 300 K (circles) measured by SQUID. (b) Magnetization vs temperature M(T) curve measured in a field of 1000 Oe from 5 K to 300 K.*

Additionally, ZnO:Co nanopowder compacted into thin plates (same pressing method applied as described in Chap. 4.7) was imaged by atomic and magnetic force microscopy using the same set-up as for the Mn doped sample. Figure 5.15(a) displays the topography of the pressed particles and Figure 5.15(b) the corresponding magnetic image taken at a lift height of 200 nm.

The observed magnetic contrast is particularly pronounced in some particles while for other grains only a weak contrast is observed which is in agreement with the results obtained from EDS and EELS measurements that revealed the inhomogenous distribution of the Co ions within the ZnO:Co nanopowder.

Even though ferromagnetism in Co doped ZnO is predicted without the need to introduce any additional charge carriers (holes), at low temperatures the ZnO:Co samples show

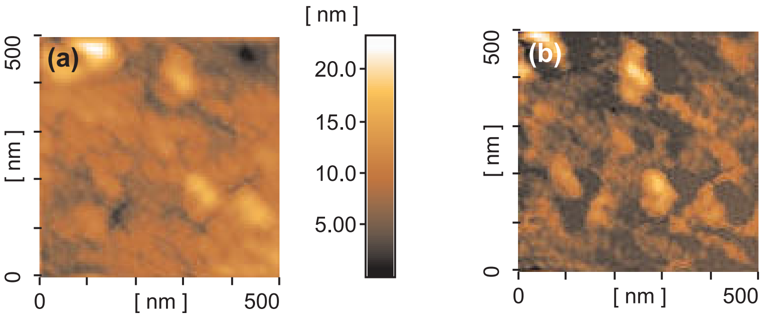

Figure 5.15: ZnO:Co nanopowder compact imaged by scanning probe microscopy: (a) Topography imaged in AFM mode; (b) magnetic structure imaged in MFM mode.

no more than the normal paramagnetic behavior of Co in the 2+ state and at elevated temperatures only diamagnetic features are detected; however no evidence of ferromagnetism has been found.

This means that neither for the Mn nor for the Co doped ZnO nanopowder ferromagnetic properties could be observed. If the ferromagnetism in ZnO diluted transition metals is induced by carriers (either by RKKY or by double exchange), samples with higher carrier concentrations are more likely to show ferromagnetic behavior. This hypothesis is supported by the results presented by Ueda *et al.* who only detected ferromagnetism in ZnCoO films having high carrier densities. They also found that the Curie temperature as well as the saturation magnetization increased with increasing carrier concentration [158]. Therefore, co-doping with Al or In (to increase the n-type conductivity) or the introduction of additional defects might by required in order to obtain a material that can be used to produce devices utilizing the magnetoresistive effect.

5.6 ZnO:V nanostructures

Besides Mn and Co, also V as transition metal in ZnO was investigated. Even though for this material composition the published data are quite contradictory too [161–163], ferromagnetic behavior of highly V-doped ZnO layers was already observed and attributed to a carrier-induced coupling mechanism between V ions [164].

In this study, the effects of V implantation into ACG grown nanowires were investigated. Nanowires grown by a wet chemical approach seem to be especially suitable for this kind of investigation, since they are known to exhibit high carrier concentrations that are required to attain a ferromagnetic coupling. In the investigation of the implanted nanowires, both the micro-/nanostructural developments during implantation and annealing and the analysis of the magnetic properties are emphasized.

5.6.1 V implantation into ACG grown nanopillars

ZnO nanowires grown by ACG on (100) Si substrate were implanted with $^{51}V^{+}$ ions. Implantation was carried out at room temperature using an ion energy of 50 keV and ion fluences of 5 x 10^{15} cm^{-2} and 1 x 10^{16} cm^{-2}. The incident beam direction was set normal to the substrate surface. The implantation process was performed by C. Ronning, University of Göttingen.

Figure 5.16 depicts the expected doping profile as calculated with the program package *TRIM* [165]. The corresponding ion range is about 26 nm with a straggling of 12 nm, leading to a V peak concentration of approximately 1.8 at.% and 3.6 at.%, respectively. The maximum penetration depth was calculated to 60 nm (without taking any channeling effects into account).

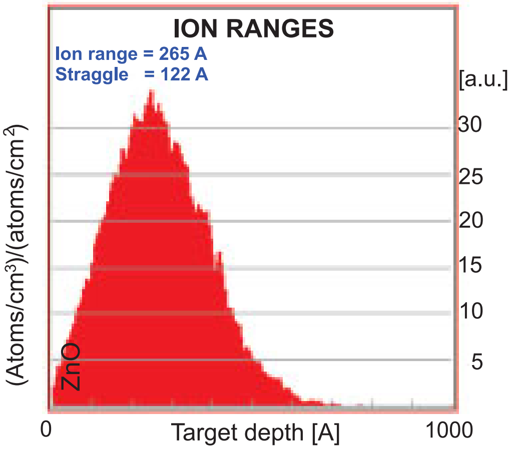

Figure 5.16: *Doping profile of V implanted in ZnO using an ion energy of 50 keV. Profile was caluated using TRIM [165].*

In order to reduce the number of defects inflicted by the implantation process, the samples were subsequently annealed under oxygen atmosphere at 500°C for 30 minutes.

5.6.2 Structural properties

The effects induced by the implantation and annealing processes were investigated by means of TEM and PL analysis. TEM images (as well as EELS results) were provided by H. Schmid, University of Bonn, while PL measurements were performed by M. Al-Suleiman, Institute of Semiconductor Technology.

The nanowires in the as-grown state are of single crystalline quality as the transmission electron micrograph displayed in Fig. 5.17(a) confirms. The wires have well defined edges and exhibit smooth surfaces. Besides bend contours and thickness fringes, no crystal defects are observed. The TEM images taken after V-ion implantation reveal that the size and the length of the nanowires did not change during the process (Fig. 5.17(b)). However, the wire surfaces show a considerable roughening as a result of atoms sputtered from the surface. In addition speckle contrast is observed that is indicative of the presence of a high number of defects (small stacking faults due to atom displacement) and lattice distortions due to residual stress. Furthermore, ion implantation leads to a large number of induced point defects that are not observable with TEM.

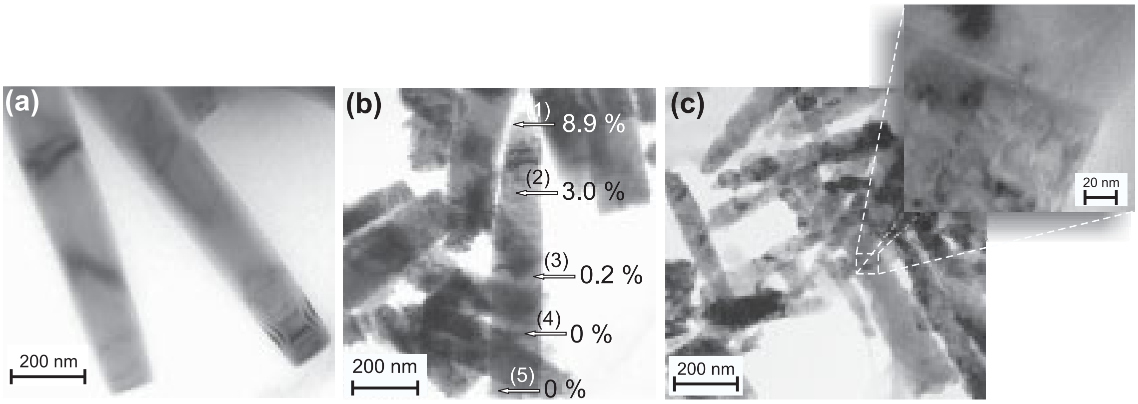

Figure 5.17: *TEM images of (a) as-grown, (b) as-implanted and (c) implanted and subsequently annealed nanowires. Figure (b) additionally displays the vanadium concentration (% cations) in the as-implanted wires measured by EELS.*

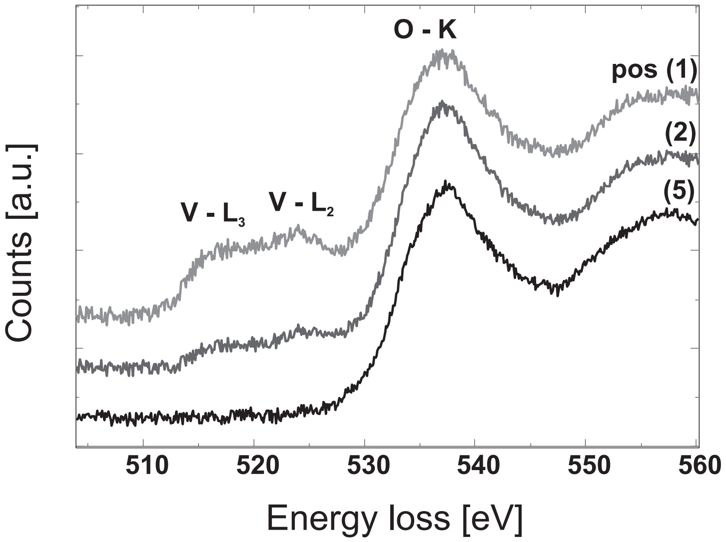

Figure 5.18: *EELS spectra acquired for positions (1), (2) and (5) as indicated in figure 5.17.*

The distribution of the V in ZnO nanowires in the as-implanted state was investigated by EELS. Wires protruding over the edge of the carbon support TEM film and with the tip region still intact i.e. the tip not broken off or destroyed by the ion irradiation, were selected for analysis. Figure 5.18 displays the EELS data acquired from various regions (labeled (1), (2) and (5), from the tip to the base), as indicated in Fig. 5.17(b). The spot size was about 80 nm. The EEL spectrum taken from the tip region (position 1) clearly shows the presence of vanadium as shown by the V-$L_{2,3}$ ionization edge onset at an energy loss of about 513 eV. The V-$L_{2,3}$ signal gradually diminishes with increasing distance from the tip. The maximum intensity ratio (V-$L_{2,3}$)/(O-K) measured yielded a cation concentration of 8.9 % V (with respect to O atoms) in the tip region, as expected for the implantation into vertically aligned wires. At a penetration depth of 200 nm the concentration decreased to $\approx$ 3 % V, whereas apparently no V is detected at depths exceeding 500 nm.

Even though the maximum penetration depth of the implanted V ions was calculated to about 60 nm, it is not surprising that there are still V atoms present at a range of 200 nm. Due to their conical shape, the effective surface of the nanowires is increased which leads to a higher amount of implanted V ions at a certain depth. Furthermore, not all wires are 100 % vertically aligned: some grow at a slightly tilted angle. This means that the implanted V ions are not only incident on the top of the wires.

The micrograph displayed in Fig. 5.17(c) indicates that the damage seen in the as-implanted nanowires seems to be even more pronounced after annealing. However, as shown in the enlargement, the crystallinity of the lattice is still preserved within small grains, thus providing evidence for a partial recovery of the matrix [166]. The resulting material appears to be nanocrystalline with lattice-mismatched grains. Concerning the incorporation of the V ions into the ZnO matrix, neither V clusters nor secondary phases are observed.

The TEM observations of a damaged but also a partially recovered crystal structure are supported by PL results displayed in Fig. 5.19. The measurements were performed at a temperature of 13 K using a He-Cd laser at 325 nm at a power of 10 mW.

For the as-grown sample (Fig. 5.19(a)) only ultraviolet near-band-edge emission (NBE) luminescence at around 3.36 eV with quite a large linewidth (approx. 15 meV) is detected. The NBE peak shows no fine structure, which is likely due to the high density of donor states in the ACG grown nanowires. The investigation of the as-grown sample after annealing supports this explanation. Optical properties of the ZnO nanowires are drastically improved by the heat treatment: The PL intensity rises by more than one order of magnitude and the width of the NBE peak decreases to about 3 meV. Both effects are attributed to an enhancement of the crystal quality due to a reduction of point defects during annealing. After the V-ion implantation (Fig. 5.19(b)) only a weak NBE and a

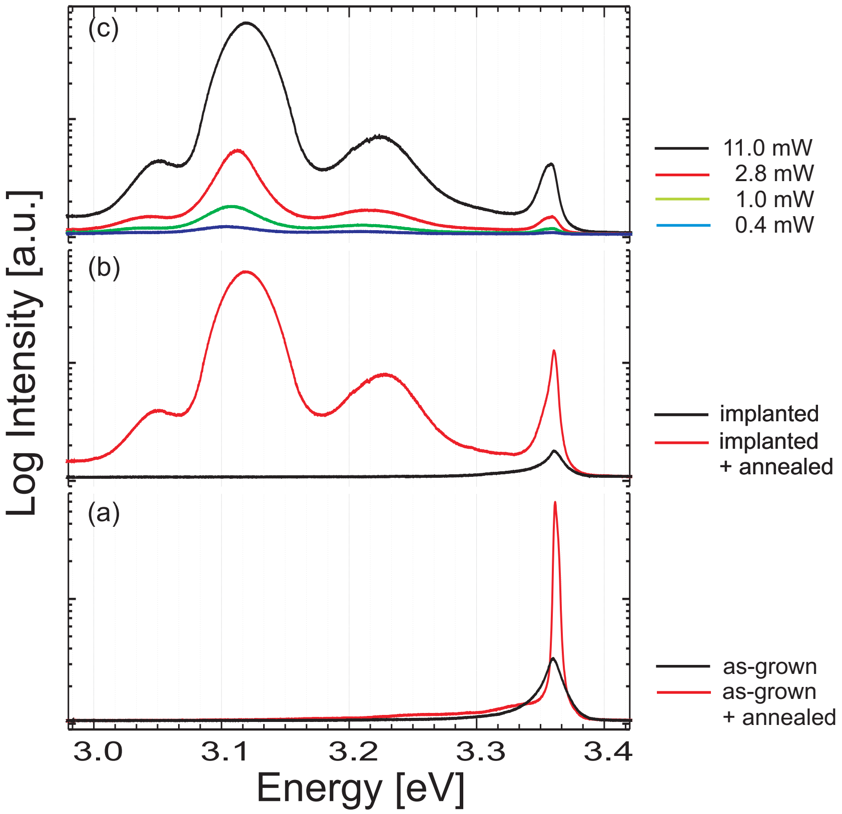

Figure 5.19: *PL spectra from nanowires in (a) the as-grown and the as-grown + annealed, (b) the as-implanted and implanted + annealed states. (c) Power-resolved measurements of the implanted + annealed sample.*

broadening of the corresponding linewidth to approx. 16 meV are detected, which is not surprising considering the damage inflicted. Annealing of the ZnO:V nanowires leads to an increase of the NBE, and also the linewidth decreases to about 7 meV. These findings give evidence that the majority of the defects caused upon implantation are removed by the heat treatment. However, strong luminescence occurs in the energy range between 3.0 and 3.3 eV, which is attributed to defect-related transitions [55]. Figure 5.19(c) displays the power-resolved measurement of the implanted and annealed sample. As the power increases the peak at 3.12 eV shifts to higher energies, giving hints towards a donor-acceptor pair (DAP) recombination followed by a longitudinal optical (LO) phonon replica separated by 72 meV. The luminescence measured at 3.23 eV can be assigned to a free electron to the acceptor (FA) transition. A similar behaviour was also detected for a Co implanted nanowire sample; however, no anomalies were found for implanted ZnO layers or other nanowire samples.

5.6.3 Magnetic properties

SQUID and MFM measurements served to characterize the magnetic properties of the sample. Figure 5.20(a) depicts the out-of-plane (with respect to the c-axis orientation of the nanowires) magnetization curves M(H) measured at 5 K. The applied field H ranged from -20 kOe to 20 kOe.

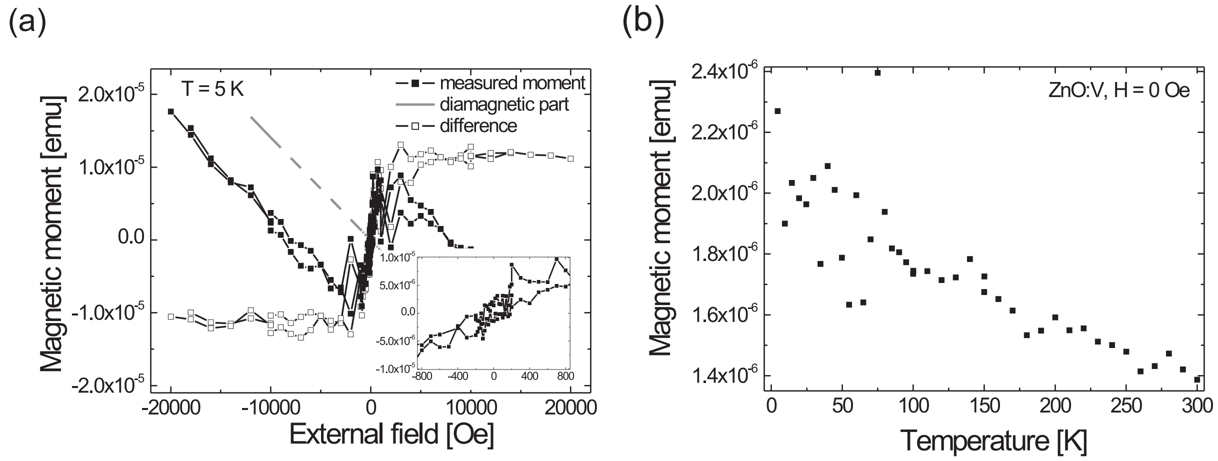

Figure 5.20: *(a) M(H) and (b) M(T) curves for ZnO:V measured with SQUID. The solid symbols indicate the measured moment, the open symbols specify the magnetization with subtracted diamagnetic fraction (dashed line). The inset in (a) shows a magnification of the graph between - 850 Oe and 850 Oe.*

A strong diamagnetic signal is detected, probably originating from the Si substrate, and only a very weak hysteresis is observed. When subtracting the diamagnetic contribution (indicated by the dashed line) the saturation magnetic moment comes to about 1 x 10^{-5} emu.

Zero-field cooled temperature dependencies M(T) within a temperature range of 5 K to 300 K were obtained separately as shown in Figure 5.20(b). With increasing temperature, the magnetization continuously decreases but no abrupt drop is observable. The multiple sudden changes in magnetization in the M(T) measurements also do not result from transitions between different magnetic states, but are due to noise and possible oxygen contaminations in the sample chamber. At about 43 K, molecular oxygen undergoes a transition from antiferromagnetic to paramagnetic and due to the MPMS system's high sensitivity, already smallest amounts of oxygen molecules are detected [167].

In both the M(H) and the M(T) measurements, the noise to signal ratio is quite significant which is not surprising regarding the very small amount (5 x 10^{15} cm^{-2}) of incorporated V ions in the top implanted region.

In addition to SQUID analysis, also MFM images were taken on ensembles as well as on single from the substrate detached nanowires using a MFM whisker tip 50 nm in diameter. In this investigation, the MFM measurements were performed by S. Sievers and M. Albrecht from the Physikalisch-Technische Bundesanstalt, Braunschweig.

Figure 5.21(a) shows the topography (AFM mode) of an ensemble of nanowires while Fig. 5.21(b) displays the corresponding MFM micrograph. The lift height for MFM image acquisition was set to 200 nm with no external magnetic field present.

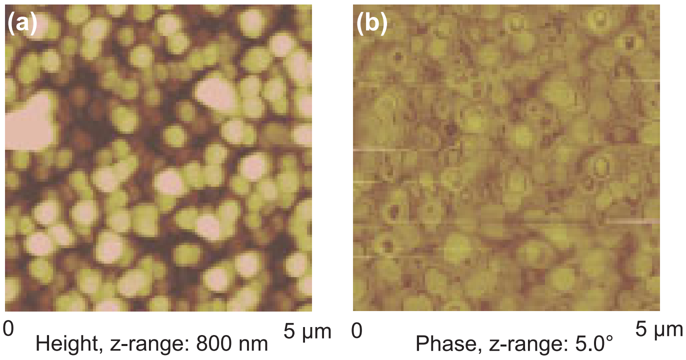

Figure 5.21: *(a) AFM and (b) corresponding MFM (b) image of the ZnO:V nanowires.*

The MFM data are not just a copy of the measured topography but reveal more complex ring structures: either a darker area in the centre of the rod surrounded by a lighter contrast or vice versa. They are randomly oriented as expected for a non-magnetized sample. Since surface forces are only short range, they cannot account for the measured phase shifts in MFM mode. This immediately suggests that the contrast can only be due to far-reaching magnetic signals emerging from the ZnO:V nanowires.

To further exclude possible effects from magnetic contaminations of the substrate which might falsify the results, a single nanorod was detached and transferred to another Si substrate. After application of in-plane oriented external magnetic fields of ± 250 Oe, the AFM topography (Fig. 5.22(a)) and the corresponding MFM micrographs (Fig. 5.22(b) and (c)) at a lift height of 100 nm were measured. Figure 5.22(b) displays the MFM image after application of an external field of +250 Oe; the result obtained after applying a reversed field of -250 Oe is shown in Fig. 5.22(c). It should be noted that prior to image acquisition the external field was turned off.
As can be clearly seen, the AFM and MFM pictures differ significantly. Furthermore, the contrasts measured in MFM mode shift after the change of the external magnetic field.

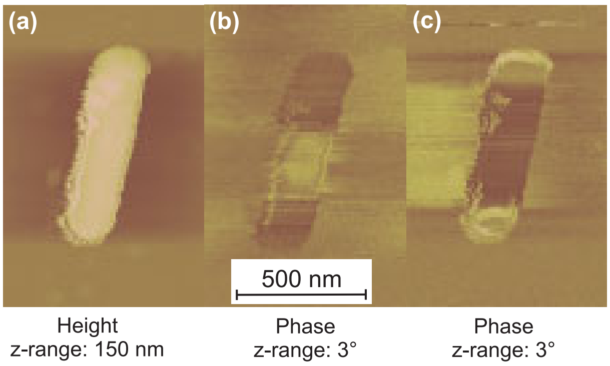

Figure 5.22: *(a) AFM and (b,c) corresponding MFM images of a single ZnO:V nanowire detached from the initial substrate on which it was grown and transferred to a Si substrate for further investigations. Prior to image acquisition an external magnetic field of +250 Oe was applied in case of (b) and a reverse field of -250 Oe in case of (c).*

From a standing ferro- or paramagnet, it is expected that the corresponding MFM micrograph shows a repulsive region (lighter color) in the centre surrounded by an attractive region (darker color), or vice versa as illustrated in Fig. 5.23(a) (left image). For a horizontally oriented magnet, the MFM image also shows only a lighter and a darker region (Fig. 5.23(a), right image). However, in Fig. 5.21(b) the measured data reveal more complex ring structures and also Fig. 5.22(b) and (c) display multiple magnetic sections. The observed micrographs correspond to the images expected for several vertically stacked magnetic dipoles as schematically illustrated in Fig. 5.23(b).

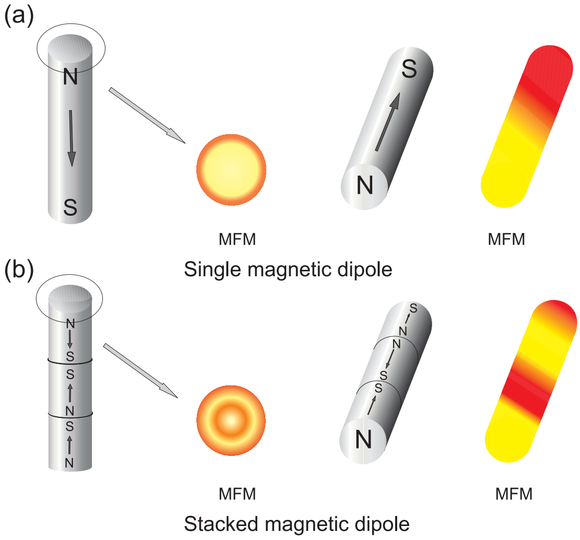

Figure 5.23: *Schematic view of a single (a) and multiple stacked (b) magnetic dipoles and the expected MFM images.*

Since the magnetic contrast is rather strong even though all measurements were performed at room temperature and simulations revealed that the magnetization of the MFM whisker at its tip comes to only about 20 Oe, a paramagnetic behavior of the ZnO:V nanowires seems rather doubtful.

Additionally, a series of measurement was taken of a cluster of nanowires. Prior to image acquisition, an external magnetic field of varying strength and direction was applied. Figure 5.24 depicts the obtained results. The image on the left displays the AFM image, the corresponding MFM micrographs taken at a lift height of 100 nm are shown on the right hand side. The arrow indicates the sequence of the performed measurements.
The magnetic field varied from 125 Oe to 500 Oe. At the same time, the orientation of the applied field was also changed between facing northward and southward. Note that during the measurements, the external magnetic field was turned off.
As can be clearly seen, the MFM images differ significantly from the topography and also the magnetic contrasts change notably throughout the series. Although the TEM observations reveal a damaged material after the implantation and annealing process, magnetic features are still detected. Therefore even an incomplete recovery of the crystal structure in combination with the V ions occupying their allocated lattice sites appears to be sufficient to enable a magnetic coupling [166]. Since topography effects can be ruled out for the contrasts occurring in the phase images, they are interpreted as a strong indication that ferromagnetism is observed at room temperature in V-ion implanted ZnO nanowires.

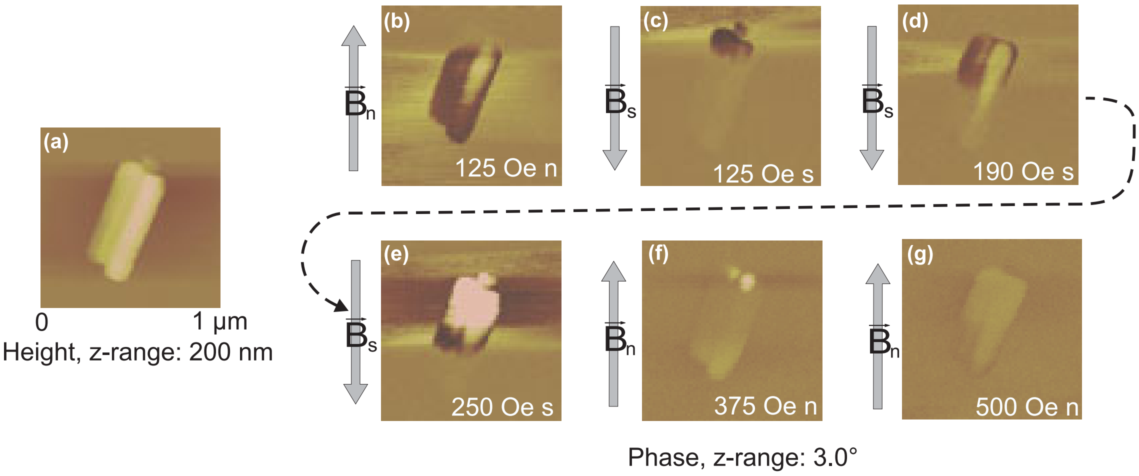

Figure 5.24: *(a) AFM (left image) and (b-g) corresponding MFM micrographs of a bundle of nanowires detached from the initial growth substrate. Prior to image acquisition an external magnetic field of varying strength and direction was applied. The lift height for scanning in MFM mode was set to 100 nm.*

The results concerning the magnetic property investigations of transition metal doped ZnO nanostructures show that of the samples examined, the V doped nanowires seem to be the most promising candidates for a room temperature ferromagnet. The MFM images taken on ensembles as well as on single wires revealed magnetic contrasts that strongly indicate ferromagnetic features of the sample.

It is widely believed that the exchange interaction of the magnetic ions in ZnO is mediated by electrons/holes, therefore nanowires grown by ACG seemed especially suitable for this kind of investigation since they exhibit a large number of charge carriers. However, there are still some questions that need to be addressed, e.g. it should be investigated if it is important that the nanowires are doped by ion implantation (which leads to an increased number of defects).

Additionally, the magnetic properties of nanowires doped with transition metals other than V should be studied. Measurements on ACG grown wires implanted with Co-ions were already performed. While SQUID analysis revealed a small hysteresis, the MFM images show by far less contrast than the phase images of the V doped nanowires.

Chapter 6

ZnO nanostructure based devices

In the preceding chapters it was already shown that ZnO nanostructures exhibit some unique electrical and magnetic properties. UV illumination and the atmospheric composition severely influence the resistivities of ZnO nanowires and nanopowders, a finding that can be used in light detecting or gas sensing applications. Layers consisting of ZnO nanopowder particles are especially suitable for such devices, since they not only have an enormous surface to volume ratio, but they are also easy to fabricate.
Additionally, magnetic features of V-implanted ZnO nanowires were already observed. Besides their potential function as storage media, polarized light emitters or spin field effect transistors (spin-FETs), also various other kind of magnetically controlled devices can be implemented.

The following section presents the results of the investigations concerning the applicability of ZnO nanopowders as sensing elements in oxygen detectors. Additionally, set-ups for a nanowire spin-FET structure and a magnetically controlled nanowire-switch are introduced.

6.1 Oxygen sensors

Ambient conditions strongly influence the electrical properties of ZnO nanostructures. Besides water vapor, it was found that oxygen molecules not only significantly reduce the photoresponse of the nanopowder samples upon UV illumination but also lead to a reduction of the photocurrent decay time. Therefore, both the decay time and the maximum photocurrent provide information of the oxygen content in the atmosphere.

In this investigation, a porous layer consisting of ZnO nanopowder particles served as gas sensing element. The layer and the electrical contacts were processed like described in Chap. 4.7. The nanopowder was provided by Grillo Zinkoxid GmbH, Germany.
The measurement was performed in the following way: While continuously applying a bias voltage of 10 V and recording the current flow, the sample was alternately illuminated with UV light for 30 s and kept in darkness for 210 s. The resulting characteristic therefore shows strong oscillations as Fig. 6.1(a) depicts. The gradual increase of oxygen pressure in the chamber (dry oxygen, about 5 % relative humidity) leads to a steady decrease of the attained maximum photocurrents and the photocurrent decay times. Figure 6.1(b) assigns the deduced maximum photocurrents and decay times to the oxygen pressure in the chamber. With increasing pressure the maximum recorded current decreases from 1.2 x 10^{-6} A to 1.0 x 10^{-7} A by nearly one order of magnitude. The decay times also drop from almost 70 s in vacuum to about 6 s, so both the maximum photocurrent and the decay time correlate with the oxygen pressure in the chamber. The data point at zero pressure should not be taken into account (as indicated by the brackets). Prior to the first measurement cycle, the sample was stored in darkness for at least 30 min while for the successive cycles the time in darkness between measurements was 210 s. Therefore, the first measurement cycle should be only regarded as test run.

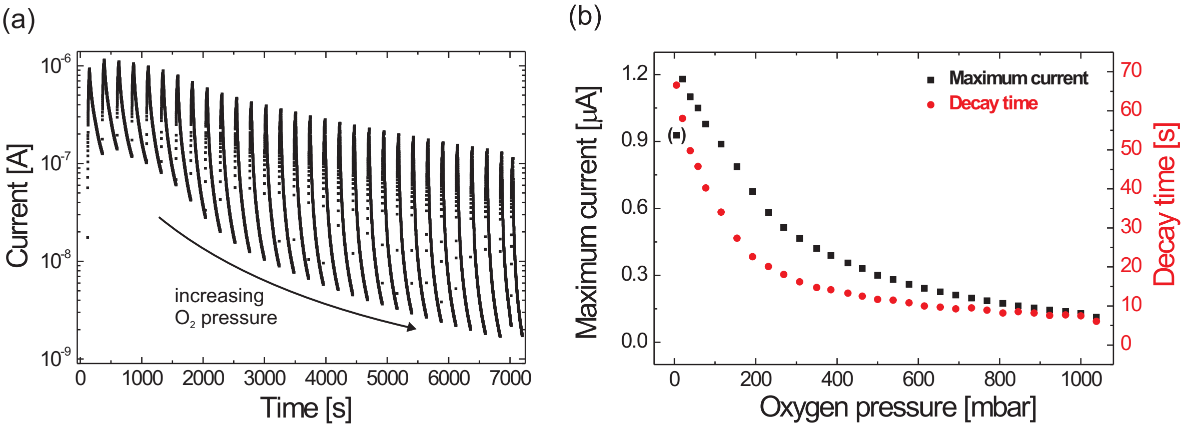

Figure 6.1: *(a) I-Vcharacteristic of a ZnO nanopowder sensing layer. The oxygen content gradually increases from 0.5 mbar to 1 bar. During measurement the sample was alternately illuminated with UV light (30 s) and kept in darkness (210 s). (b) Deduced maximum photocurrents and decay times over oxygen pressure.*

In order to verify the data and to investigate the stability of the device, the measurement was repeated at a constant oxygen pressure of about 400 mbar. Figure 6.2 displays the deduced maximum photocurrents and decay times, the inset depicts the corresponding *I(t)* characteristic. Since the system requires some time to settle in a stable state, the first cycle should not be taken into account.

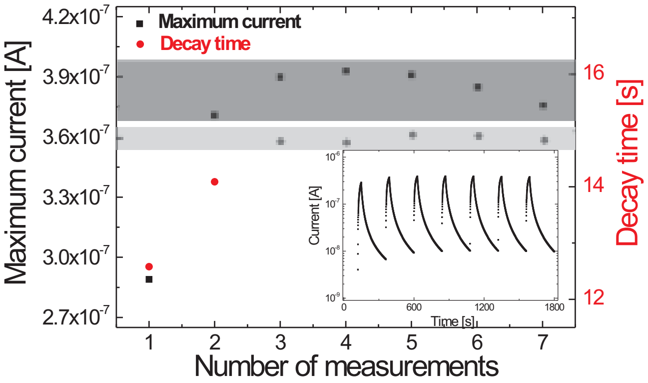

Figure 6.2: *Deduced maximum photocurrents and decay times at a constant oxygen pressure of 400 mbar. The sample was alternately illuminated with UV light (30 s) and kept in darkness (210 s). The inset shows the corresponding I(t) characteristic.*

The values are pretty stable throughout the measurement series. The deduced maximum photocurrents range between 3.7 x 10^{-7} A and 4.0 x 10^{-7} A, while the decay times approximate a nearly stable level of about 15 s. These results are in good consistency with the values derived at 400 mbar from the pressure dependent measurement (3.8 x 10^{-7} A and 14.2 s).

In the experiments presented above, the ZnO nanopowder layers were deposited onto a glass substrate and a commercially available LED served as light source. The next step towards realization of a sensor would be to integrate the two components (sensing layer and LED) into a single device. This can be realized by simply depositing the nanopowder layer on top of a non-packaged LED structure like schematically depicted in Fig. 6.3. The set-up may consists of an AlGaN-GaN LED structure covered by an electrically insulating but UV transparent film (like Al_2O_3). A layer consisting of ZnO nanoparticles is deposited on top of the device. It should be taken care that the powder layer is sufficiently thin to ensure that the UV light can penetrate the entire ZnO layer. Electrical contact is provided by thermally evaporated top electrodes.

Such a sensor is well suited for measurements in dry environments; however, in order to utilize the device in air, also the influence of humidity on the sensor performance has to be taken into account.

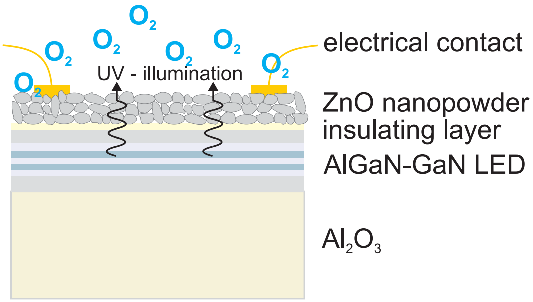

Figure 6.3: *Schematic image of an oxygen sensor incorporating both the ZnO sensing layer and the UV light source (LED structure).*

6.2 Magnetic nanowire based devices

A spin-FET is probably one of the most popular proposed spintronic devices. The theoretical concept was first proposed in 1990 by Datta and Das [168]. In analogy of an electron-optic light modulator, they envisioned a magnetically-sensitive transistor where the source and drain contacts are made up of ferromagnetic materials. The magnetized source contact injects spin-polarized electrons into the non-magnetized channel where they are transported to the spin-selective drain contact. The transistor is in the ON state if the spins of the conducting electrons reaching the drain contact are in parallel alignment to the magnetization of the drain electrode. If they are oriented differently, the device is in the OFF state.

In contrast to ordinary FETs, the applied gate voltage in a spin-transistor not only controls the conductivity of the channel but also the spin-orientation of the electrons. The orientation of the electron spins at the position of the drain contact depends on the length of the channel and on the strength of the applied gate voltage. Since spin states are non-volatile and can be altered without necessarily requiring the application of an electric current, they are promising components for storage medias.

In the set-up proposed by Datta and Das, ferromagnetic metals (iron) served as source and drain electrodes. However, electrical spin-injection from ferromagnetic metals into semiconductors is difficult to achieve due to significant mismatches in the conductivity values. To overcome these problems, ferromagnetic semiconductors can be employed as spin-injecting source and spin-selective drain contacts. The successful realization of spin-injection from a ferromagnetic semiconductor was already shown by Fiederling *et al.* [169].

A ZnO nanoscale spin-FET can be realized by utilizing undoped ZnO nanowires as non-magnetic channel with selected V implanted regions serving as ferromagnetic contacts. The gate electrode can be simply implemented by using a conducting substrate covered by an isolating layer (e.g. a Si substrate covered by isolating SiO_2). Figure 6.4 schematically depicts a layout of such a device structure.

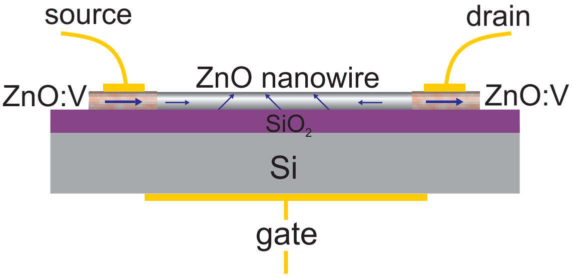

Figure 6.4: *Concept of a ZnO nanowire based spin-FET (OFF state). V implanted areas serve as ferromagnetic source and drain electrodes for spin-injection and spin-selection, respectively. The gate electrode is realized by employing a Si substrate covered by an isolating* SiO_2 *layer.*

Prior to fabricate a nanowire transistor, experiments on ZnO layers grown by MBE were performed. An advantage of using layers as opposed to nanowires is that they can be structured by photolithographic techniques. Furthermore, selective doping with V-ions can be achieved by implanting through a net structure while selective doping of single nanowires requires implantation by employing focused ion beam.

The resulting pattern of a selectively V-doped ZnO surface is displayed in Fig. 6.5. The implanted squares are of darker color than the non-implanted stripes which is due to the damages inflicted to the crystal structure upon irradiation with V-ions. The photograph was taken prior to annealing.

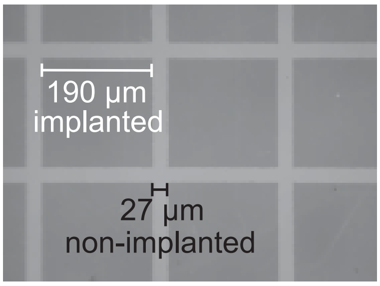

Figure 6.5: *Optical microscopy image of a selectively implanted ZnO layer. Implantation process was performed by C. Ronning, University of Göttingen. The image was taken prior to annealing.*

However, even after multiple annealing steps, the crystal structure of the implanted layer is still severely damaged and highly resistive as PL and electrical measurements reveal. Furthermore, compared to the results obtained from magnetic measurements of ZnO:V nanowires grown by ACG, the MFM images taken of the implanted ZnO layers show no magnetic contrast. It seems likely that the charge concentration in the high purity ZnO layers is too low to enable a magnetic coupling between the V-ions. Therefore, experiments on nanowire FET structures which require more complex patterning techniques need to be performed in order to reveal if a nanoscale spin sensitive transistor can be implemented in such a way.

Ferromagnetic ZnO:V nanowires can not only be employed in devices utilizing the magnetoresistive effect, but they might also serve as switches in electric circuits. The nanowires used for such switches have to be sufficiently flexible and also need to be responsive to magnetic fields.
ACG grown nanowires are highly conductive and also very flexible; therefore they seem to be ideal candidates for such applications. Furthermore, they can be grown on all kind of substrate material, also on metals or ITO covered glass. Additionally, by prestructuring the substrate, growth of single isolated nanowires is possible [170] that can be employed as single nanoscale switches.

The MFM micrographs of the V-implanted ACG grown nanowires (see Chap. 5.6.3) showed magnetic contrast even though the images were acquired after the external magnetic field was turned off. In addition to these investigations, measurements were performed during application of an in-plane oriented magnetic field of 250 Oe.
Figure 6.6 shows a series of scans displayed in chronological order. The images were taken either with or without an applied magnetic field. The micrographs on the left show the topography of the nanowires while the scans on the right depict the corresponding MFM micrographs. The measurements were provided by S. Sievers and M. Albrecht, Physikalisch-Technische Bundesanstalt, Braunschweig.

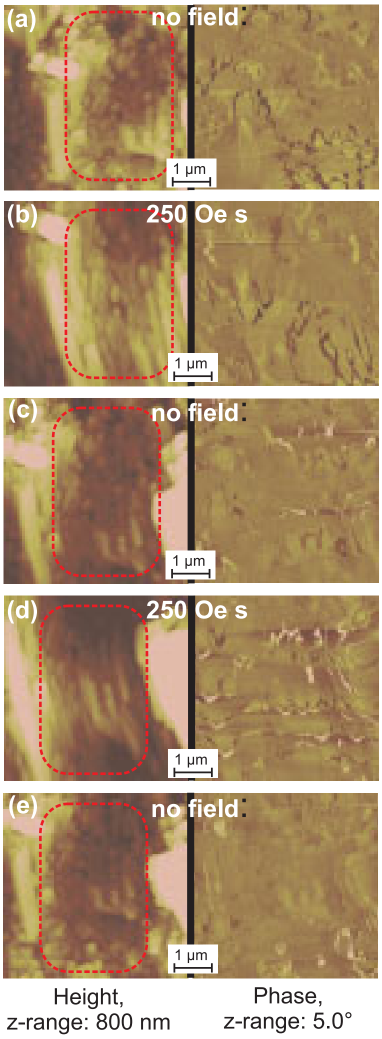

Figure 6.6: *AFM/MFM measurement series of ACG grown nanowires implanted with V-ions. Images were taken with or without application of an in-plane oriented external field. The micrographs are arranged in chronological order. The dashed red lines that are added to the AFM images mark the region of interest.*

Without applying a magnetic field (Fig. 6.6(a) - no B field), the nanowires are vertically aligned as the topography scan reveals. Also magnetic contrast in the phase image is observed. When a magnetic field of 250 Oe is applied, the nanowires tend to align themselves parallel to the B field lines as evidently depicted in the AFM micrograph of Fig. 6.6(b). The contrasts in the MFM phase image shift too.

Figure 6.6(c) was taken at least 12 hours after the previous scan. The AFM image reveals that most of the nanowires partly returned to an upright position. However, if the B-field is reapplied, the nanowires change their orientation and again align themselves horizontally (Figure 6.6(d)). The observed effect is repeated every time the B-field is turned off (Figure 6.6(e)). The AFM measurements therefore indicate that the orientation of the nanowires can be switched between a vertical and horizontal alignment simply by applying a magnetic field. The effect of an applied B-field also becomes obvious in the phase images. The contrasts observed in the MFM micrographs shift significantly between the measurements thus indicating ferromagnetic features of the sample.

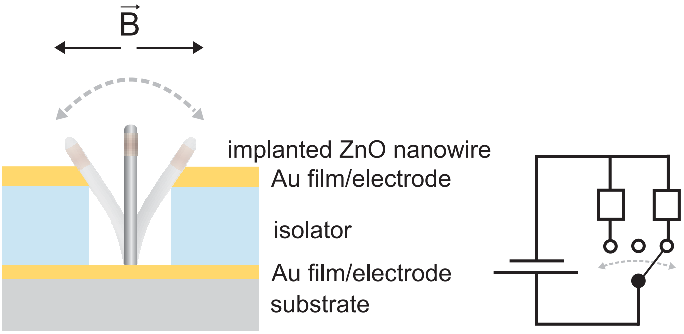

Figure 6.7: *Schematic image of a nanoscale switch based on a magnetic nanowire. Additionally displayed on the right hand side is the corresponding equivalent circuit of the device.*

Magnetic nanowires could therefore be used as magnetically controlled switches in electric circuits. A layout of a device structure incorporating such a transition metal doped wire is schematically displayed in Figure 6.7. By changing the direction of the applied field, the nanowire either contacts the left or the right electrode, thus acting as a magnetically controlled nanowire switch. The corresponding equivalent circuit of the device is depicted on the right of Fig. 6.7.

Outlook

This thesis provides a thorough characterization of the electrical properties of ZnO nanowires grown by different methods. Additionally, the magnetic features of ZnO nanostructures diluted with Mn-, Co- and V-ions are studied and discussed in detail. The gained knowledge is used to develop new device structures and concepts. Nevertheless, there are still some issues that need to be clarified.

Electrical properties

This work not only investigates the electrical transport characteristics of ZnO nanostructures, but also provides a model explaining the observed effects. The results reveal that even though they are simple in chemical structure, ZnO nanowires are complex systems. Their electrical properties are difficult to characterize since they are influenced by many factors. Performances of devices incorporating nanostructures should therefore be checked under real conditions in every development stage.
Since changes in illumination and ambient conditions severely affect the resistivity of the nanostructures, they provide an ideal foundation for sensing elements needed in UV or gas detectors, for instance in oxygen sensors. Nevertheless, the results reveal that not only the amount of oxygen in the atmosphere influences the resistivity and the photocurrent decay time, but also humidity has a strong effect on these magnitudes. Therefore, prior to realize an oxygen sensor that can be employed in humid air, it is a necessity to perform further investigations to be able to precisely distinguish between the influences of oxygen and water vapor.

Magnetic properties

The presented studies reveal that among nanostructures doped with transition metal ions, nanowires grown by ACG and implanted with V-ions show the most promising results concerning ferromagnetic properties at room temperature. ACG grown nanowires typically exhibit higher charge carrier concentrations as compared to nanowires grown from the gas

phase. It is therefore of particular importance to identify if there is indeed a correlation between the magnetic coupling and the charge carrier densities in the wires.
A way to respond to this question is to investigate the magnetic properties of V-implanted VPT grown nanowires. The electrical measurements presented in Chap. 4 reveal that the high purity nanowires grown by VPT have lower charge carrier densities than the ACG grown nanowires, therefore MFM micrographs should reveal less contrast. Another possibility would be to use co-doping, for instance with Al, to alter the carrier concentration in the nanostructures.
Nevertheless, there should also be further research on the in-situ doping of the nanostructures with transition metal ions during growth. First experiments were already performed using a modified wet chemical approach in expansion of the method patented in [171]: A solution consisting of zinc acetate and cobalt acetate (0.02 mol l^{-1} and 0.002 mol l^{-1}, respectively, mixed in a ratio of 1:1) is drop-cast onto a Si substrate that is heated to 220°C. Figure 6.8 displays a SEM micrograph of the nanowires that can be found on the substrate after the solution is vaporized.

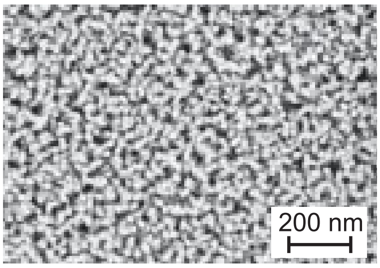

Figure 6.8: *Scanning electron micrograph of ZnO(:Co) nanowires fabricated by drop-casting a solution consisting of Zn- and Co-acetate onto a Si substrate that is heated to* 220° *C.*

The resulting nanowires are typically about 150 nm in length and between 20 nm to 30 nm in diameter. Even though first EDS measurements showed no Co-signal coming from the nanowires, further investigations, for instance EELS analyses, are a necessity, since the detection limit of the EDS set-up is merely 5 %, therefore lower amounts of incorporated Co atoms are not detectable.

Device concepts

Merging the information obtained from the measurement presented in Chap. 4 and Chap. 5 will allow to introduce some novel kind of device structures. However, there are still some problems that must be overcome: First, the applicability of the oxygen sensor needs to be extended to humid air. This could be achieved by heating the ZnO sensing layer in order to get rid of water contaminants on the surface. Secondly, the sensing layer and the LED structure should be combined into a single device.

Additionally, before processing devices based on the magnetic properties of ZnO, further basic experiments are required to obtain a deeper understanding of magnetic coupling in transition metal doped semiconductors. If this is achieved then the conversion of the gained knowledge into devices like the ones presented in Chap. 6 is not such a challenging task anymore.

Appendix A

Estimation of charge carrier concentration

The probability that an impurity is ionized is determined by the impurity distribution function. This distribution function slightly differs from the Fermi-Dirac function which is commonly used for electrons (fermions). In Fermi-Dirac statistics, each energy level can be occupied by two electrons with oppositely orientated spins. However, a donor energy level can only be occupied by one electron. If it was occupied by two electrons, the donor atom would by negatively charged and would therefore have a different energy. The concentration of ionized donors N_d^+ is therefore given by

$$N_d^+ = N_d \left(2\, exp\left(\frac{E_F - E_d}{kT}\right) + 1\right)^{-1}, \tag{A.1}$$

where N_d denotes the donor density at the energy level E_d.
The charge carrier concentration equals the number of ionized donors ($n = N_d^+$). Furthermore, according to Eq. (4.17) the position of the Fermi energy is given by

$$E_F = E_C + kT\, ln\left(\frac{n}{N_C}\right), \tag{A.2}$$

with E_C symbolizing the energy level of the conduction band and N_C the effective density of states in the conduction band which is specified as

$$N_C = 2\left(\frac{m^* kT}{2\pi\hbar^2}\right)^{3/2}. \tag{A.3}$$

m^* represents the effective mass (for ZnO $m^* = 0.27 m_e$). Inserting Eq. (A.2) into Eq. (A.1) and using some simple mathematical modifications, the relationship between n and N_d is finally given by

$$0 = \frac{2}{N_C} exp\left(\frac{E_C - E_d}{kT}\right) n^2 + n - N_d. \tag{A.4}$$

Solutions of this equation are

$$n_{1,2} = \frac{-1 \pm \sqrt{1 + \frac{8}{N_C} exp\left(\frac{E_C - E_d}{kT}\right) N_d}}{\frac{4}{N_C} exp\left(\frac{E_C - E_d}{kT}\right)} \tag{A.5}$$

whereas only the positive sign leads to a physically reasonable solution.

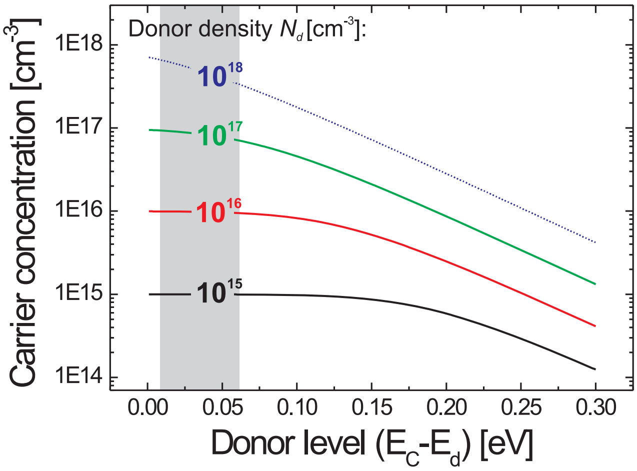

Figure A.1: *Calculated carrier concentration over ionization energy for different donor densities.*

Figure A.1 displays the calculated carrier concentrations n over ionization energy $(E_C - E_d)$ for different donor densities. In the energy range where the donor states in ZnO are located (10 - 60 meV, as indicated by the grey area), n is almost constant and equals the corresponding value of the donor concentration. Note that the graph calculated for a donor density of 10^{18} cm^{-3} is only conditionally valid, since Eq. (A.1) is only applicable for $|E_F - E_d| << kT$. Nevertheless, also for this donor density, the differences observed between the charge carrier and the donor concentration are less than a factor of 3, therefore the assumption $n = N_d$ is justified.

Appendix B

Derivation of the conductance

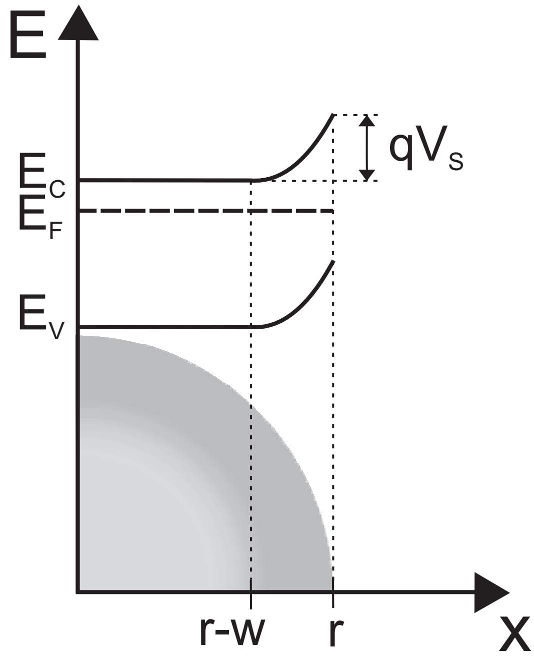

Figure B.1: *Band bending effects at the surface of the ZnO nanowire.* V_s *denotes the surface potential while* E_F*,* E_C *and* E_V *respectively, represent the energy positions of the Fermi level, the conduction and the valence band.* r *symbolizes the radius of the nanowire and* w *the width of the depletion layer ("shell").*

The equivalent circuit of a nanowire exhibiting such a core-shell structure consists of two resistors arranged in parallel configuration. The total resistance R_{total} is therefore determined by

$$\frac{1}{R_{total}} = \frac{1}{R_{shell}} + \frac{1}{R_{core}}, \tag{B.1}$$

where R_{shell} denotes the resistance of the shell and R_{core} the resistance of the core. The conductance is defined by the reciprocal of the resistance ($G = R^{-1}$), hence the total conductance is given by

$$G_{total} = G_{shell} + G_{core} = \sigma_{shell}\frac{A_{shell}}{l} + \sigma_{core}\frac{A_{core}}{l}, \tag{B.2}$$

and the conductance times the length of the nanowire yields

$$G_L = \int\limits_{0}^{2\pi}\int\limits_{r-w}^{r} x\sigma_{shell}\, dx\, d\varphi + \sigma_{core}A_{core}. \tag{B.3}$$

By using Poisson's equation (with ψ symbolizing the electrostatic potential, F the electric field and ρ the charge density)

$$\frac{d^2\psi}{dx^2} \equiv -\frac{dF}{dx} = -\frac{\rho}{\epsilon\epsilon_0} = \frac{qN_d}{\epsilon\epsilon_0}, \tag{B.4}$$

an expression for $E_C(x) - E_C(0)$ can be derived:

$\int_{F(0)}^{F(x)} dx = \frac{q}{\epsilon\epsilon_0} N_d \int_0^x dx$

with

$\frac{dE}{dx} = qF$

$\hookrightarrow \int_{E_C(0)}^{E_C(x)} dE = q\int_0^x F(x)dx = q\int_0^x \frac{q}{\epsilon\epsilon_0} N_d x\, dx$

$$\hookrightarrow E_C(x) - E_C(0) = \frac{q^2}{2\epsilon\epsilon_0} N_d x^2. \tag{B.5}$$

The charge carrier concentration $n(x)$ in the conduction band is determined by

$$n(x) = N_C exp\left(-\frac{E_C(x) - E_F}{kT}\right), \tag{B.6}$$

where N_C denotes the effective density of states in the conduction band.
When assuming that $n \approx N_d$ and simply modifying Eq. (B.6), in the flatband region (at position $x = 0$) $E_C(0) - E_F$ is given by

$$E_C(0) - E_F = -kT\, ln\frac{N_d}{N_C}. \tag{B.7}$$

The conductivity in the core (σ_{core}) is constant; however, the conductivity in the shell is a function of x ($\sigma_{shell} = \sigma_{shell}(x)$):

$$\sigma_{shell}(x) = q\;\mu\;n_{shell}(x) \tag{B.8}$$

$$\overset{Eq.\ (B.6)}{=} q\mu N_C exp\left(-\tfrac{E_C(x)-E_F}{kT}\right)$$

$$= q\mu N_C exp\left(-\tfrac{E_C(x)-E_C(0)+E_C(0)-E_F}{kT}\right)$$

$$= q\mu N_C exp\left(-\tfrac{E_C(x)-E_C(0)}{kT}\right) exp\left(-\tfrac{E_C(0)-E_F}{kT}\right)$$

$$\overset{Eq.\ (B.5)}{=} q\mu N_C exp\left(-\tfrac{q^2 N_d x^2}{2\epsilon\epsilon_0 kT}\right) exp\left(-\tfrac{E_C(0)-E_F}{kT}\right)$$

$$\overset{Eq.\ (B.7), n\approx N_d}{=} q\mu N_C exp\left(-\tfrac{q^2 N_d x^2}{2\epsilon\epsilon_0 kT}\right) exp\left(-\tfrac{-kTln\frac{N_d}{N_C}}{kT}\right)$$

$$\hookrightarrow \sigma_{shell}(x) = q\mu N_d exp\left(-\frac{q^2 N_d x^2}{2\epsilon\epsilon_0 kT}\right). \tag{B.9}$$

Therefore, the conductance finally yields

$$G_L = \underbrace{2\pi q\mu N_d \int_{r-w}^{r} x exp\left(-\frac{q^2 N_d}{2\epsilon\epsilon_0 kT}x^2\right) dx}_{\sigma_{shell}(x)A_{shell}} + \underbrace{q\mu N_d \pi (r-w)^2}_{\sigma_{core}A_{core}}, \tag{B.10}$$

where w denotes the length of the depletion region and is given by

$$w = \sqrt{\frac{2\epsilon\epsilon_0 V_S}{qN_d}}. \tag{B.11}$$

Appendix C

Abbreviations and symbols

ACG	aqueous chemical growth	-
AFM	atomic force microscopy	-
DAP	donor-acceptor pair	-
DMS	diluted magnetic semiconductor	-
EDS	energy dispersive X-ray spectroscopy	-
EELS	electron energy loss spectroscopy	-
EL	electroluminescence	-
FA	free electron to acceptor	-
FX	free exciton	-
FET	field effect transistor	-
FIB	focus ion beam	-
I-V	current-voltage	-
ITO	indium tin oxide	-
LED	light emitting diode	-
MBE	molecular beam epitaxy	-
MFM	magnetic force microscopy	-
MIS	metal-insulator-semiconductor	-
MOVPE	metalorganic vapor phase epitaxy	-
NBE	near-band edge emission	-
PL	photoluminescence	-
PMMA	polymethyl methacrylate	-
PTB	Physikalisch Technische Bundesanstalt	-
(FE)SEM	(field emission) scanning electron microscopy	-

RKKY	Ruderman-Kittel-Kasuya-Yoshida	-
SQUID	superconducting quantum interference device	-
STM	scanning tunneling microscopy	-
TEM	transmission electron microscopy	-
TLM	transmission line measurement	-
TM	transition metal	-
UV	ultraviolett	-
VLS	vapor-liquid-solid	-
VPT	vapor phase transport	-
VS	vapor-solid	-
XRD	X-ray diffraction	-

Symbols

$\chi_{\mathrm{dia,para,ferro}}$	(dia-, para-, ferro-) magnetic susceptibility	-
χ_{sc}	electron affinity (of the semiconductor)	eV
$\epsilon\epsilon_0$	dielectric constant	As/Vm
Φ_{b}	barrier height	eV
Φ_{m}	work function (of the metal)	eV
$\hbar$	(reduced) Planck's constant	1.05×10^{-34} Js
λ	wavelength	nm
μ	magnetic moment	Am^2
μ_{B}	Bohr magneton	9.274×10^{-24} Am^2
$\mu_{\mathrm{n,h}}$	electron, hole mobility	$\mathrm{cm}^2/\mathrm{Vs}$
ρ	resitivity	$\Omega\mathrm{cm}$
σ	conductivity	$(\Omega\mathrm{cm})^{-1}$
σ_{core}	conductivity of nanowire core	$(\Omega\mathrm{cm})^{-1}$
σ_{shell}	conductivity of nanowire shell	$(\Omega\mathrm{cm})^{-1}$
τ	decay time	s
a, c	lattice constants	Å
A_{core}	cross-section of nanowire core	cm^2
A_{shell}	cross-section of nanowire shell	cm^2
A_{geo}	geometrical cross-section	cm^2
A_{eff}	effective cross-section	cm^2
A^*	Richardson constant	$\mathrm{Acm}^2/\mathrm{K}^2$

$B_{\mathrm{J}}(x)$	Brillouin function	-
C_{pm}	capacitance (at particle-metal interface)	F
C_{pp}	capacitance (at particle-particle interface)	F
$D^0X_{A/B}$	A/B exciton bound to neutral donor	-
e	electron	-
E	energy	eV
E_{00}	characteristic tunneling energy	eV
E_{AB}	energy splitting between A and B	eV
E_{C}	conduction band edge energy	eV
E_{D}	donor energy	eV
E_{F}	Fermi energy	eV
E_{g}	band gap energy	eV
E_{V}	valence band edge energy	eV
(LO-)FX_A	(longitudinal optical phonon replica) of the A-free exciton	-
g	Lande splitting factor	-
G	conductance	S (or Ω^{-1})
h	hole	-
H	magnetic field	A/m
I	current	A
I_{ds}	drain-source current	A
J	current density	A/cm^2
J_S	saturation current density	A/cm^2
J_{rev}	reverse current density	A/cm^2
k	Boltzmann constant	1.38 x 10^{-23} J/K
l	length	m
l_{eff}	effective (channel) length	m
$m^*_{\mathrm{n,h}}$	normalized effective mass of electron/hole	kg
M	magnetization	A/m
n_{id}	ideality factor	-
$n_{\mathrm{n/h}}$	electron/hole concentration	cm^{-3}
$N_{\mathrm{a}}, N_{\mathrm{d}}$	acceptor and donor concentration	cm^{-3}
N_{C}	effective density of states in the conduction band	cm^{-3}
N_{d}^+	ionized donor concentration	cm^{-3}

$O_{2,\text{ gas/ad}}$	oxygen (gaseous/adsorbed)	-
q	elementary charge	1.6 x 10^{-19} C
r.h.	relative humidity	%
R_C	contact resistance	Ω
R_NW	resistance of the nanowire	Ω
R_pm	resistance at particle-metal interface	Ω
R_pp	resistance at particle-particle interface	Ω
R_tot	total resistance	Ω
T	temperature	°C or K
T_C	Curie-temperature	°C or K
T_N	Néel-temperature	°C or K
v_d	drift velocity	m/s
V	voltage	V
V_bi	built-in voltage	V
$V_\text{ds,(sat)}$	(saturation) drain-source voltage	V
V_gs	gate-source voltage	V
V_p	pinch-off voltage	V
V_S	surface potential	V
w	width of depletion layer	m

Publications and conference contributions

Publications as main author

1. E. Schlenker, A. Bakin, T. Weimann, P. Hinze, D. H. Weber, A. Gölzhäuser, H.-H. Wehmann and A. Waag, *On the difficulties in characterizing ZnO nanowires*, Nanotechnology, **19**, 365707 (2008).

2. E. Schlenker, A. Bakin, H. Schmid, W. Mader, H. Bremers, A. Hangleiter, H.-H. Wehmann, M. Al-Suleiman, J. Lüdke, M. Albrecht and A. Waag, *Properties of Mn-doped ZnO nanopowders*, Applied Physics A **91**, 375 (2008).

3. E. Schlenker, A. Bakin, H.-H. Wehmann, A. C. Mofor, A. Behrends, A. Waag, T. Weimann, P. Hinze, A. Melnikov and A. D. Wieck, *Electrical properties of ZnO based nanostructures* , Journal of the Korean Physical Society, **53**, 119 (2008).

4. E. Schlenker, A. Bakin, H. Schmid, W. Mader, S. Sievers, M. Albrecht, C. Ronning, S. Müller, M. Al-Suleiman, B. Postels, H.-H. Wehmann, U. Siegner and A. Waag, *Properties of V-implanted ZnO nanorods*, Nanotechnology, **18**, 125609 (2007).

5. E. Schlenker, A. Bakin, B. Postels, A. Che Mofor, H.-H. Wehmann, T. Weimann, P. Hinze and A. Waag, *Electrical charaterization of ZnO nanorods* , Physica Status Solidi (b), **244**, 1473 (2007).

6. E. Schlenker, V. Mertens, J. Parisi, R. Reineke-Koch and M. Köntges, *Schottky contact analysis of photovoltaic chalcopyrite thin film absorbers*, Physics Letters A, **362**, 229 (2007).

7. E. Schlenker, A. Bakin, B. Postels, A. Che Mofor, M. Kreye, C. Ronning, S. Sievers, M. Albrecht, U. Siegner, R. Kling and A. Waag, *Magnetic characterization of vanadium doped ZnO nanorods*, Journal of Superlattices and Microstructures, **42**, 236 (2006).

8. E. Schlenker, V. Mertens, J. Parisi, R. Reineke-Koch and M. Köntges, *Schottky contacts on Cu(In,Ga)*Se_2 *thin films*, in Proceedings of the 20th European Photovoltaic Solar Energy Conference, 1793 (2005).

Publications as co-author

1. A. Bakin, A. Wagner, E. Schlenker, B. Postels, M. Al-Suleiman, A. Behrends, A.-H. Elshaer, V. Petukhov and A. Waag, *ZnO Nanostructures and Thin Layers for Device Applications*, ECS Trans, **16**, 107 (2008).

2. T. Weimann, P. Hinze, E. Schlenker, A. Bakin, A. C. Mofor, A. Behrends and A. Waag, *Electrical and structural characterisation of single ZnO nanorods* , Microelectronic Engineering, **85**, 1248 (2008).

3. B. Postels, A. Kasprzak, T. Buergel, A. Bakin, E. Schlenker, H.-H. Wehmann and A.Waag, *Dye-sensitized solar cells on the basis of ZnO nanorods*, Journal Korean Physical Society, **53**, 115 (2008).

4. D. H. Weber, A. Beyer, B. Völkel, A. Gölzhäuser, E. Schlenker, A. Bakin and A. Waag, *Determination of the specific resistance of individual freestanding ZnO nanowires with the low energy electron point source microscope*, Applied Physics Letters, **91**, 253126 (2007).

5. A. Bakin, A. El-Shaer, A. C. Mofor, M. Al-Suleiman, E. Schlenker, A. Waag, *ZnMgO-ZnO quantum wells embedded in ZnO nanopillars: towards realisation of nano-LEDs*, Physica Status Solidi (c), **4**, 158 (2007).

6. A. El-Shaer, A. Bakin, E. Schlenker, A. C. Mofor, G. Wagner, S. A. Reshanov and A. Waag, *Fabrication and characterization of n-ZnO on p-SiC heterojunction diodes on 4H-SiC substrates*, Journal of Superlattices and Microstructures, **42**, 387 (2007).

7. A. C. Mofor, A. Bakin, U. Chejarla, E. Schlenker, A. El-Shaer, G. Wagner, N. Boukos, A. Travlos and A. Waag, *Fabrication of ZnO nanorod-based p-n heterojunction on SiC substrate* , Journal of Superlattices and Microstructures, **42**, 415 (2007).

8. A. C. Mofor, F. Reuss, A. El-Shaer, R. Kling, E. Schlenker, A. Bakin, H. Ahlers, U. Siegner, S. Sievers, M. Albrecht, W. Schoch, W. Limmer, J. Eisenmenger, T. Mueller, A. Huebel, G. Denninger, P. Ziemann, A. Waag, *Magnetism in V-/Mn-doped ZnO layers fabricated on sapphire* , Applied Physics A, **88**, 161 (2007).

Oral presentations

1. E. Schlenker, A. Bakin, H. Schmid, W. Mader, H. Bremers, A. Hangleiter, H.-H. Wehmann, M. Al-Suleiman, J. Lüdke, M. Albrecht and A. Waag, *Characterization of Mn doped ZnO nanopowder*, Spring meeting of the German Physical Society, Berlin (2008).

2. E. Schlenker, A. C. Mofor, A. Behrends, H.-H. Wehmann, M. Al-Suleiman, A. Bakin and A. Waag, *Oxidische Halbleiter für die Spinelektronik* , Status Seminar BMBF nanoQUIT, Stuttgart (2007).

3. E. Schlenker, A. Bakin, B. Postels, A. C. Mofor, H.-H. Wehmann, A. Waag , T. Weimann and P. Hinze, *Electrical characterization of ZnO-nanostructures*, Fall meeting of the European Materials Research Society, Warsaw, Poland (2006)

4. E. Schlenker, A. Bakin, B. Postels, M. Al-Suleiman, A. C. Mofor, A. Waag, C. Ronning , S. Sievers, M. Albrecht and U. Siegner, *Magnetism in vanadium-doped ZnO nanorods*, The 4th International Workshop on ZnO and Related Materials, Gießen (2006).

5. E. Schlenker, A. Bakin, A. C. Mofor, B. Postels, M. Kreye, A. El-Shaer, A. Waag , C. Ronning, S. Sievers, M. Albrecht and U. Siegner, *Magnetic properties of vanadium doped ZnO-nanopillars*, Spring meeting of the German Physical Society, Dresden (2008).

Poster presentations

1. E. Schlenker, T. Weimann, P. Hinze, A. Bakin, H.-H. Wehmann, A. C. Mofor, A. Behrends, A. Melnikov, A. Wieck and A. Waag, *Electrical properties of ZnO nanorods*, The 13th International Conference on II-VI Compounds, Jeju, Korea (2007)

2. E. Schlenker, T. Weimann, P. Hinze-b, A. Bakin, H.-H. Wehmann, A. C. Mofor, B. Postels, A. Waag, *Electrical properties of ZnO nanorods*, Spring meeting of the German Physical Society, Regensburg (2007)

3. E. Schlenker, A. Bakin, B. Postels, A. C. Mofor, M. Kreye, C. Ronning, S. Sievers, M. Albrecht, U. Sieger, R. Kling and A. Waag, *Magnetic characterisation of vanadium-doped ZnO nanorods* , Spring meeting of the European Materials Research Society, Strasbourg, France (2006)

4. E. Schlenker, V. Mertens, J. Parisi, R. Reineke-Koch, M. Köntges, *Schottky contacts on Cu(In,Ga)*Se_2 *thin films*, 20th European Photovoltaic Solar Energy Conference, Barcelona, Spain (2005)

Bibliography

[1] D. Appell, Nature **419**, 553 (2002).

[2] S. Iijima, Nature **354**, 56 (1991).

[3] A. M. Morales and C. M. Lieber, Science **279**, 208 (1998).

[4] J. Xiang, W. Lu, Y. Hu, Y. Wu, H. Yan, and C. M. Lieber, Nature **441**, 489 (2006).

[5] Y. Huang, X. Duan, L. J. Lauhon, K.-H. Kim, and C. M. Lieber, Science **294**, 1313 (2001).

[6] F. Qian, S. Gradecak, Y. Li, C.-Y. Wen, and C. Lieber, Nano Lett. **5**, 2287 (2005).

[7] Y. Qin, X. Wang, and Z. L. Wang, Nature **451**, 809 (2008).

[8] T. Dietl, H. Ohno, F. Matsukura, J. Cibert, and D. Ferrand, Science **287**, 1019 (2000).

[9] K. Sato and H. Katayama-Yoshida, Jpn. J. Appl. Phys. **39**, L555 (2000).

[10] H. Kind, H. Yan, B. Messer, M. Law, and P. Yang, Adv. Mater. **14**, 158 (2002).

[11] Q. H. Li, Y. X. Liang, Q. Wan, and T. H. Wang, Appl. Phys. Lett. **85**, 6389 (2004).

[12] R. P. Feynman, California Institute of Technology Journal of Engineering and Science **4**, 23 (1960).

[13] N. Taniguchi, Proc. Intl. Conf. Prod. Eng. Tokyo, Part II, Japan Society of Precision Engineering (1974).

[14] A. Aviram and M. A. Ratner, Chem. Phys. Lett. **29**, 277 (1974).

[15] C. K. Chiang, C. R. Fincher, Y. W. Park, A. J. Heeger, H. Shirakawa, E. J. Louis, S. C. Gau, and A. G. MacDiarmid, Phys. Rev. Lett. **39**, 1098 (1977).

[16] J. Sagiv, J. Am. Chem. Soc. **102**, 92 (1980).

[17] R. G. Nuzzo and D. L. Allara, J. Am. Chem. Soc. **105**, 4481 (1983).

[18] G. Binnig, H. Rohrer, C. Gerber, and E. Weibel, Appl. Phys. Lett. **40**, 178 (1982).

[19] G. Binnig, H. Rohrer, C. Gerber, and E. Weibel, Phys. Rev. Lett. **49**, 57 (1982).

[20] G. Binnig, C. F. Quate, and C. Gerber, Phys. Rev. Lett. **56**, 930 (1986).

[21] C. W. Tang, Appl. Phys. Lett. **48**, 183 (1986).

[22] C. W. Tang and S. A. VanSlyke, Appl. Phys. Lett. **51**, 913 (1987).

[23] K. Kudo, M. Yamashina, and T. Moriizumi, Jpn. J. Appl. Phys. **23**, 130 (1984).

[24] R. Rossetti, S. Nakahara, and L. E. Brus, J. Chem. Phys. **79**, 1086 (1983).

[25] D. M. Eigler and E. K. Schweizer, Nature **344**, 524 (1990).

[26] D. S. Bethune, M. S. de Vries, G. Gorman, R. Savoy, J. Vazquez, and R. Beyers, Nature **363**, 605 (1993).

[27] S. Iijima and T. Ichihashi, Nature **363**, 603 (1993).

[28] S. J. Tans, M. H. Devoret, H. Dai, A. Thess, R. E. Smalley, L. J. Geerligs, and C. Dekker, Nature **386**, 474 (1997).

[29] M. Bockrath, D. H. Cobden, P. L. McEuen, N. G. Chopra, A. Zettl, A. Thess, and R. E. Smalley, Science **275**, 1922 (1997).

[30] S. J. Tans, A. R. M. Verschueren, and C. Dekker, Nature **393**, 49 (1998).

[31] R. Martel, T. Schmidt, H. R. Shea, T. Hertel, and P. Avourisa, Appl. Phys. Lett. **73**, 2447 (1998).

[32] Z. W. Pan, Z. R. Dai, and Z. L. Wang, Science **291**, 1947 (2001).

[33] Y. Wu, R. Fan, and P. Yang, Nano Lett. **2**, 87 (2002).

[34] M. Bjork, B. Ohlsson, T. Sass, A. Persson, C. Thelander, M. H. Magnusson, K. Deppert, L. R. Wallenberg, and L. Samuelson, Nano Lett. **2**, 87 (2002).

[35] Y. Cui, Q. Wei, H. Park, and C. Lieber, Science **293**, 1289 (2001).

[36] X. Duan, Y. Huang, Y. Cui, J. Wang, and C. M. Lieber, Nature **409**, 66 (2001).

[37] Y. Cui and C. Lieber, Science **291**, 851 (2001).

[38] P.-C. Chang, Z. Fan, C.-J. Chien, D. Stichtenoth, C. Ronning, and J. G. Lu, Appl. Phys. Lett. **89**, 133113 (2006).

[39] Y. Dong, G. Yu, M. McAlpine, W. Lu, and C. Lieber, Nano Lett. **8**, 386 (2008).

[40] A. Nadarajah, R. Word, J. Meiss, and R. Konenkamp, Nano Lett. **8**, 534 (2008).

[41] C. Soci, A. Zhang, B. Xiang, S. A. Dayeh, D. P. R. Aplin, J. Park, X. Y. Bao, Y. H. Lo, and D. Wang, Nano Lett. **7**, 1003 (2007).

[42] E. Schlenker, A. Bakin, T. Weimann, P. Hinze, D. H. Weber, A. Gölzhäuser, H.-H. Wehmann, and A. Waag, Nanotechnology **19**, 365707 (2008).

[43] M. H. Huang, S. Mao, H. Feick, H. Yan, Y. Wu, H. Kind, E. Weber, R. Russo, and P. Yang, Science **292**, 1897 (2001).

[44] J. C. Johnson, H.-J. Choi, K. P. Knutsen, R. D. Schaller, P. Yang, and R. J. Saykally, Nature Mater. **1**, 101 (2002).

[45] R. K. Joshi and F. E. Kruis, Appl. Phys. Lett. **89**, 153116 (2006).

[46] N. Barsan and U. Weimar, J. Electroceramics **7**, 143 (2001).

[47] C. Li, D. Zhang, X. Liu, S. Han, T. Tang, J. Han, and C. Zhou, Appl. Phys. Lett. **82**, 1613 (2003).

[48] X. Wang and C. Ozkan, Nano Lett. **8**, 398 (2008).

[49] B. O'Regan and M. Grätzel, Nature **353**, 737 (1991).

[50] M. Law, L. Greene, J. Johnson, R. Saykally, and P. Yang, Nature Mater. **4**, 455 (2005).

[51] S. J. Pearton, D. P. Norton, K. Ip, Y. W. Heo, and T. Steiner, J. Vac. Sci. Technol. B **22**, 932 (2004).

[52] T. Makino, Y. Segawa, M. Kawasaki, A. Ohtomo, R. Shiroki, K. Tamura, T. Yasuda, and H. Koinuma, Appl. Phys. Lett. **78**, 1237 (2001).

[53] D. Vogel, P. Krueger, and J. Pollmann, Phys. Rev. B **52**, R14316 (1995).

[54] W. J. Fan, J. B. Xia, P. A. Agus, S. T. Tan, S. F. Yu, and X. W. Sun, J. Appl. Phys. **99**, 013702 (2006).

[55] B. K. Meyer, H. Alves, D. M. Hofmann, W. Kriegseis, D. Forster, F. Bertram, J. Christen, A. Hoffmann, M. Straßburg, M. Dworzak, U. Haboeck, and A. V. Rodina, phys. stat. sol. (b) **241**, 231 (2004).

[56] D. C. Reynolds, D. C. Look, B. Jogai, C. W. Litton, G. Cantwell, and W. C. Harsch, Phys. Rev. B **60**, 2340 (1999).

[57] C. Boemare, T. Monteiro, M. Soares, J. Guilherme, and E. Alves, Physica B **308-310**, 985 (2001).

[58] D. C. Look, B. Claflin, Y. I. Alivov, and S. J. Park, phys. stat. sol. (a) **201**, 2203 (2004).

[59] W. Hirschwald, P. Bonasewicz, L. Ernst, M. Grade, D. Hofmann, S. Krebs, R. Littbarski, and G. Neumann, in *Current Topics in Materials Science (Vol 7)*, edited by E. Kaldis (North-Holland, Amsterdam, 1981).

[60] S. E. Harrison, Phys. Rev. **93**, 52 (1954).

[61] D. C. Look, J. W. Hemsky, and J. R. Sizelove, Phys. Rev. Lett. **82**, 2552 (1999).

[62] S. F. J. Cox, E. A. Davis, S. P. Cottrell, P. J. C. King, J. S. Lord, J. M. Gil, H. Alberto, R. C. Vilao, J. P. Duarte, N. A. de Campos, A. Weidinger, R. L. Lichti, and S. J. C. Irvine, Phys. Rev. Lett. **86**, 2601 (2001).

[63] D. M. Hofmann, A. Hofstaetter, F. Leiter, H. Zhou, F. Henecker, B. K. Meyer, S. B. Orlinskii, J. Schmidt, and P. G. Baranov, Phys. Rev. Lett. **88**, 045504 (2002).

[64] C. G. van de Walle, Phys. Rev. Lett. **85**, 1012 (2000).

[65] A. Janotti and C. G. V. de Walle, Phys. Rev. B **76**, 165202 (2007).

[66] D. C. Look, Mat. Sci. Engin. B **80**, 283 (2001).

[67] T. Makino, Y. Segawa, A. Tsukazaki, A. Ohtomo, and M. Kawasaki, Appl. Phys. Lett. **87**, 022101 (2005).

[68] Z. L. Wang, J. Phys.: Condens. Matter **16**, R829 (2004).

[69] P. X. Gao, Y. Ding, W. Mai, W. L. Hughes, C. Lao, and Z. L. Wang, Science **309**, 1700 (2005).

[70] M. H. Huang, Y. Wu, H. Feick, N. Tran, E. Weber, and P. Yang, Adv. Mater. **13**, 113 (2001).

[71] J. B. Hannon, S. Kodambaka, F. M. Ross, and R. M. Tromp, Nature **440**, 69 (2006).

[72] R. Hauschild, Dissertation, University of Karlsruhe, 2006.

[73] A. C. Mofor, A. S. Bakin, A. Elshaer, D. Fuhrmann, F. Bertram, A. Hangleiter, J. Christen, and A. Waag, phys. stat. sol. (c) **3**, 1046 (2006).

[74] A. Mofor, A. Bakin, A. Elshaer, D. Fuhrmann, F. Bertram, A. Hangleiter, J. Christen, and A. Waag, Appl. Phys. A **88**, 17 (2007).

[75] M. Al-Suleiman, A. C. Mofor, A. El-Shaer, A. Bakin, H.-H. Wehmann, and A. Waag, Appl. Phys. Lett. **89**, 231911 (2006).

[76] A. C. Mofor, Dissertation, Technical University Braunschweig, 2007.

[77] B. Postels, H.-H. Wehmann, A. Bakin, M. Kreye, D. Fuhrmann, J. Blaesing, A. Hangleiter, A. Krost, and A. Waag, Nanotechnology **18**, 195602 (2007).

[78] B. Postels, Dissertation, Technical University Braunschweig, 2008.

[79] E. H. Rhoderick and R. H. Williams, in *Metal-Semiconductor Contacts*, edited by P. Hammond and R. L. Grimsdale (Oxford Science Publications, Oxford, 1987).

[80] D. K. Schroder, *Semiconductor Material and Device Characterization* (John Wiley & Sons, Inc., New York, 1990).

[81] F. A. Padovani and R. Stratton, Solid-State Electron. **9**, 695 (1966).

[82] Z. Y. Zhang, C. H. Jin, X. L. Liang, Q. Chen, and L.-M. Peng, Appl. Phys. Lett. **88**, 073102 (2006).

[83] J. Appenzeller, M. Radosavljević, J. Knoch, and P. Avouris, Phys. Rev. Lett. **92**, 048301 (2004).

[84] A. El-Shaer, A. Bakin, A. C. Mofor, J. Stoimenos, B. Pecz, and A. Waag, Superlatt. Microstruct. **42**, 158 (2007).

[85] H. S. Yang, D. P. Norton, S. J. Pearton, and F. Ren, Appl. Phys. Lett. **87**, 212106 (2005).

[86] Y. Cheng, P. Xiong, L. Fields, J. P. Zheng, R. S. Yang, and Z. L. Wang, Appl. Phys. Lett. **89**, 093114 (2006).

[87] a. J. L. Chang Shi Lao, P. Gao, L. Zhang, D. Davidovic, R. Tummala, and Z. L. Wang, Nano Lett. **6**, 263 (2006).

[88] J.-R. Kim, H. Oh, H. M. So, J.-J. Kim, J. Kim, C. J. Lee, and S. C. Lyu, Nanotechnology **13**, 701 (2002).

[89] A. Schlachetzki, *Halbleiter-Elektronik: Grundlagen und moderne Entwicklung* (B.G. Teubner, Stuttgart, 1990).

[90] H. Stöcker, *Taschenbuch der Physik* (Verlag Harri Deutsch, Frankfurt a. M., 1998).

[91] J. H. Hea, S. T. Hob, T. B. Wub, L. J. Chenb, and Z. L. Wang, Chem. Phys. Lett. **435**, 119 (2007).

[92] H. von Wenckstern, E. M. Kaidashev, M. Lorenz, H. Hochmuth, G. Biehne, J. Lenzner, V. Gottschalch, R. Pickenhain, and M. Grundmann, Appl. Phys. Lett. **84**, 79 (2004).

[93] A. Umar, B.-K. Kim, Ju-JinKim, and Y. B. Hahn, Nanotechnology **18**, 175606 (2007).

[94] W. I. Park, J. S. Kim, , G.-C. Yi, M. H. Bae, and H.-J. Lee, Appl. Phys. Lett. **85**, 5052 (2004).

[95] K. Keem, H. Kim, G.-T. Kim, J. S. Lee, B. Min, K. Cho, M.-Y. Sung, and S. Kim, Appl. Phys. Lett. **84**, 4376 (2004).

[96] R. R. Mehta and B. S. Sharma, J. Appl. Phys. **44**, 325 (1973).

[97] Z. Fan, P.-C. Chang, J. G. Lu, E. C. Walter, R. M. Penner, C. hung Lin, and H. P. Lee, Appl. Phys. Lett. **85**, 6128 (2004).

[98] D. H. Weber, A. Beyer, B. Völkel, A. Gölzhäuser, E. Schlenker, A. Bakin, and A. Waag, Appl. Phys. Lett. **91**, 253126 (2007).

[99] D. H. Weber, Dissertation, University of Bielefeld, 2008.

[100] T. Voss and L. Wischmeier, J. Nanosci. Nanotechnol. **8**, 228 (2008).

[101] I. Shalish, H. Temkin, and V. Narayanamurti, Phys. Rev. B **69**, 245401 (2004).

[102] J.-P. Richters, T. Voss, L. Wischmeier, I. Rückmann, and J. Gutowski, Appl. Phys. Lett. **92**, 011103 (2008).

[103] Y. W. Heo, L. C. Tien, D. P. Norton, B. S. Kang, F. Ren, B. P. Gila, and S. J. Pearton, Appl. Phys. Lett. **85**, 2002 (2004).

[104] Y.-J. Ma, Z. Zhang, F. Zhou, L. Lu, A. Jin, and C. Gu, Nanotechnology **16**, 746 (2005).

[105] Z.-M. Liao, K.-J. Liu, J.-M. Zhang, J. Xu, and D.-P. Yu, Phys. Lett. A **367**, 207 (2007).

[106] Y.-F. Lin, W.-B. Jian, C. P. Wang, Y.-W. Suen, Z.-Y. Wu, F.-R. Chen, J.-J. Kai, and J.-J. Lin, Appl. Phys. Lett. **90**, 223117 (2007).

[107] Y. W. Heo, L. C. Tien, D. P. Norton, S. J. Pearton, B. S. Kang, F. Ren, and J. R. LaRoche, Appl. Phys. Lett. **85**, 3107 (2004).

[108] P.-C. Chang, C.-J. Chien, D. Stichtenoth, C. Ronning, and J. G. Lu, Appl. Phys. Lett. **90**, 113101 (2007).

[109] X. Lin, X. B. He, T. Z. Yang, W. Guo, D. X. Shi, H.-J. Gao, D. D. D. Ma, S. T. Lee, F. Liu, and X. C. Xie, Appl. Phys. Lett. **89**, 043103 (2006).

[110] J. Goldberger, D. J. Sirbuly, M. Law, , and P. Yang, J. Phys. Chem. B **109**, 9 (2005).

[111] J. Y. Park, H. Oh, J.-J. Kim, and S. S. Kim, Nanotechnology **17**, 1255 (2006).

[112] Q. H. Li, Q. Wan, Y. X. Liang, and T. H. Wang, Appl. Phys. Lett. **84**, 4556 (2004).

[113] Z. Fan, D. Wang, P.-C. Chang, W.-Y. Tseng, and J. G. Lu, Appl. Phys. Lett. **85**, 5923 (2004).

[114] L. J. Brillson, H. L. Mosbacker, M. J. Hetzer, Y. Strzhemechny, G. H. Jessen, D. C. Look, G. Cantwell, J. Zhang, and J. J. Song, Appl. Phys. Lett. **90**, 102116 (2007).

[115] G. D. J. Smit, S. Rogge, and T. M. Klapwijk, Applied Physics Letters **81**, 3852 (2002).

[116] Y. Ding and Z. Wang, J. Phys. Chem. B **108**, 12280 (2004).

[117] J. Liu, P. Gao, W. Mai, C. Lao, Z. L. Wang, and R. Tummala, Appl. Phys. Lett. **89**, 063125 (2006).

[118] D. C. Look, G. C. Farlow, P. Reunchan, S. Limpijumnong, S. B. Zhang, and K. Nordlund, Phys. Rev. Lett. **95**, 225502 (2005).

[119] E. Comini, G. Faglia, M. Ferroni, and G. Sberveglieri, Appl. Phys. A **88**, 45 (2007).

[120] T. Voss, C. Bekeny, L. Wischmeier, H. Gafsi, S. Börner, W. Schade, A. C. Mofor, A. Bakin, and A. Waag, Appl. Phys. Lett. **89**, 182107 (2006).

[121] C. Bekeny, T. Voss, H. Gafsi, J. Gutowski, B. Postels, M. Kreye, and A. Waag, J. Appl. Phys. **100**, 104317 (2006).

[122] C. Bekeny, T. Voss, B. Hilker, J. Gutowski, R. Hauschild, H. Kalt, B. Postels, A. Bakin, and A. Waag, J. Appl. Phys. **102**, 044908 (2007).

[123] M. N. Rahaman, L. C. de Jonghe, J. A. Voigt, and B. A. Tuttle, J. Mat. Sci. **25**, 737 (1990).

[124] C. Y. Wang, V. Cimalla, T. Kups, C.-C. Röhlig, T. Stauden, O. Ambacher, M. Kunzer, T. Passow, W. Schirmacher, W. Pletschen, K. Köhler, and J. Wagner, Appl. Phys. Lett. **91**, 103509 (2007).

[125] S. Polarz, A. Roy, M. Lehmann, M. Driess, F. E. Kruis, A. Hoffmann, and P. Zimmer, Adv. Funct. Mater. **17**, 1385 (2007).

[126] Y. Ni, X. Cao, G. Wu, G. Hu, Z. Yang, and X. Wei, Nanotechnology **18**, 155603 (6pp) (2007).

[127] Z. Wang, H. Zhang, L. Zhang, J. Yuan, S. Yan, and C. Wang, Nanotechnology **14**, 11 (2003).

[128] K. Giannakopoulos, N. Boukos, and A. Travlos, Superlatt. Microstruct. **39**, 115 (2006).

[129] N. Barsan and U. Weimar, J. Phys.: Condens. Matter **15**, R813 (2003).

[130] Y. Takahashi, M. Kanamori, A. Kondoh, H. Minoura, and Y. Ohya, Jpn. J. Appl. Phys **33**, 6611 (1994).

[131] S. E. Ahn, J. S. Lee, H. Kim, S. Kim, B. H. Kang, K. H. Kim, and G. T. Kim, Appl. Phys. Lett. **84**, 5022 (2004).

[132] R. Ghosh, M. Dutta, and D. Basak, Appl. Phys. Lett. **91**, 073108 (2007).

[133] R. Sun, A. Nakajima, A. Fujishima, T. Watanabe, and K. Hashimoto, J. Phys. Chem. B **105**, 1984 (2001).

[134] X. Feng, L. Feng, M. Jin, J. Zhai, L. Jiang, and D. Zhu, J. Am. Chem. Soc. **126**, 62 (2004).

[135] M. N. Baibich, J. M. Broto, A. Fert, F. N. Van Dau, F. Petroff, P. Eitenne, G. Creuzet, A. Friederich, and J. Chazelas, Phys. Rev. Lett. **61**, 2472 (1988).

[136] G. Binasch, P. Grünberg, F. Saurenbach, and W. Zinn, Phys. Rev. B **39**, 4828 (1989).

[137] S. A. Wolf, D. D. Awschalom, R. A. Buhrman, J. M. Daughton, S. von Molnar, M. L. Roukes, A. Y. Chtchelkanova, and D. M. Treger, Science **294**, 1488 (2001).

[138] S. A. Wolf, J. Supercond. **13**, 195 (2000).

[139] K. Yosida, *Theory of Magnetism* (Springer, Heidelberg, 1996).

[140] C. Zener, Phys. Rev. **81**, 440 (1951).

[141] C. Zener, Phys. Rev. **82**, 403 (1951).

[142] A. C. Mofor, A. El-Shaer, A. Bakin, A. Waag, H. Ahlers, U. Siegner, S. Sievers, M. Albrecht, W. Schoch, N. Izyumskaya, V. Avrutin, S. Sorokin, S. Ivanov, and J. Stoimenos, Appl. Phys. Lett. **87**, 062501 (2005).

[143] D. Rugar, H. J. Mamin, P. Guethner, S. E. Lambert, J. E. Stern, I. McFadyen, and T. Yogi, J. Appl. Phys. **68**, 1169 (1990).

[144] Y. Heo, D. Norton, L. Tien, Y. Kwon, B. Kang, F. Ren, S. Pearton, and J. LaRoche, Mat. Sci. Engin. R **R47**, 1 (2004).

[145] T. Fukumura, Z. Jin, A. Ohtomo, H. Koinuma, and M. Kawasaki, Appl. Phys. Lett. **75**, 3366 (1999).

[146] D.-L. Hou, X.-J. Ye, H.-J. Meng, H.-J. Zhou, X.-L. Li, C.-M. Zhen, and G.-D. Tang, Mat. Sci. Engin. B **138**, 184 (2007).

[147] H. Schmidt, M. Diaconu, H. Hochmuth, M. Lorenz, A. Setzer, P. Esquinazi, A. Pöppl, D. Spemann, K.-W. Nielsen, R. Gross, G. Wagner, and M. Grundmann, Superlatt. Microstruct. **39**, 334 (2006).

[148] T. Fukumura, Z. Jin, M. Kawasaki, T. Shono, T. Hasegawa, S. Koshihara, and H. Koinuma, Appl. Phys. Lett. **78**, 958 (2001).

[149] E. Chikoidze, Y. Dumont, H. von Bardeleben, J. Gleize, F. Jomard, E. Rzepka, G. Berrerar, D. Ferrand, and O. Gorochov, Appl. Phys. A **88**, 167 (2007).

[150] A. Tomaszewska-Grzeda, A. Opalińska, E. Grzanka, W. Łojkowski, A. Gedanken, M. Godlewski, S. Yatsunenko, V. Osinniy, and T. Story, Appl. Phys. Lett. **89**, 242102 (2006).

[151] X. M. Cheng and C. L. Chien, J. Appl. Phys. **93**, 7876 (2003).

[152] M. G. V.Yu. Ivanov and, S. Yatsunenko, A. Khachapuridze, Z. Golstrokacki, M. Sawicki, A. Omel'chuk, M. Bulany, and A. Gorban, phys. stat. sol. (c) **1**, 250 (2004).

[153] V. Avrutin, N. Izyumskaya, U. Özgür, A. El-Shaer, H. Lee, W. Schoch, F. Reuss, V. Beshenkov, A. Pustovit, A. C. Mofor, A. Bakin, H. Morkoç, and A. Waag, Superlatt. Microstruct. **39**, 291 (2006).

[154] V. A. L. Roy, A. B. Djurišić, H. Liu, X. X. Zhang, Y. H. Leung, M. H. Xie, J. Gao, H. F. Lui, and C. Surya, Appl. Phys. Lett. **84**, 756 (2004).

[155] A. Teke, U. Özgür, S. Doğan, X. Gu, H. Morkoç, B. Nemeth, J. Nause, and H. O. Everitt, Phys. Rev. B **70**, 195207 (2004).

[156] *Practical Analytical Electron Microscopy in Material Science*, edited by D. B. Williams (Philips Electron Optics Publishing Group, Mahwah/ NJ, 1984).

[157] K. R. Kittilstved, N. S. Norberg, and D. R. Gamelin, Phys. Rev. Lett. **94**, 147209 (2005).

[158] K. Ueda, H. Tabata, and T. Kawai, Appl. Phys. Lett. **79**, 988 (2001).

[159] N. Jedrecy, H. J. von Bardeleben, Y. Zheng, and J.-L. Cantin, Phys. Rev. B **69**, 041308 (2004).

[160] N. Volbers, H. Zhou, C. Knies, D. Pfisterer, J. Sann, D. Hofmann, and B. Meyer, Appl. Phys. A **88**, 153 (2007).

[161] H. Tabata, M. Saeki, S. L. Guo, J. H. Choi, and T. Kawai, Physica B **308**, 993 (2001).

[162] S. Ramachandran, A. Tiwari, J. Narayan, and J. T. Prater, Appl. Phys. Lett. **87**, 172502 (2005).

[163] K. Ando, H. Saito, Z. Jin, T. Fukumura, M. Kawasaki, Y. Matsumoto, and H. Koinuma, J. Appl. Phys. **89**, 7284 (2001).

[164] H. Saeki, H. Tabata, and T. Kawai, Solid State Commun. **120**, 439 (2001).

[165] J. F. Ziegler, J. P. Biersack, and U. Littmark, *The Stopping and Range of Ions in Solids* (Pergamon, New York, 1985), see also http://www.srim.org.

[166] C. Ronning, P. X. Gao, Y. Ding, Z. L. Wang, and D. Schwen, Appl. Phys. Lett. **84**, 783 (2004).

[167] *Quantum design MPMS Application Note 1014-210 (www.qdusa.com).*

[168] S. Datta and B. Das, Appl. Phys. Lett. **56**, 665 (1990).

[169] R. Fiederling, M. Keim, G. Reuscher, W. Ossau, G. Schmidt, A. Waag, and L. W. Molenkamp, Nature **402**, 787 (1999).

[170] M. Lehnhardt, Master's thesis, Technical University Braunschweig, 2007.

[171] M. Elbahri, R. Adelung, and D. Paretkar, Verfahren zur Herstellung von Nanostrukturen auf einem Substrat, Patent - DE 10 2005 060 407 B3, 2007.

Curriculum Vitae

Persönliche Angaben

Name	Eva Schlenker
Geburtsdatum	07. Februar 1978
Geburtsort	VS-Schwenningen
Familienstand	ledig

Schulbildung

1984–1988	Grundschule in VS-Schwenningen
1988–1997	Gymnasium am Deutenberg in VS-Schwenningen
05. 1997	Abitur, Gesamtnote 1.3

Freiwilliges Soziales Jahr

1997–1998	Mitarbeit in einem Alten- und Pflegeheim in Kiel/Molfsee

Studium der Physik

1998–2000	Grundstudium, Universität Oldenburg
2001	Auslandsstudium, University of Sydney, Australien
2002–2005	Hauptstudium, Universität Oldenburg
2004–2005	Diplomarbeit, Thema ”Schottky-Kontakte auf $Cu(In,Ga)Se_2$ Absorbern”
03. 2005	Abschluss Diplom, Gesamtnote ”sehr gut”

Promotion

seit 05. 2005	Wissenschaftliche Mitarbeiterin am Institut für Halbleitertechnik, Technische Universität Braunschweig

Acknowledgements

Finally, I would like to express my gratitude to ..

- Prof. Dr. Andreas Waag for accepting me as a member of his group at the Institute of Semiconductor Technology (Institut für Halbleitertechnik - *IHT*), for providing excellent working conditions and for giving me the opportunity to write this thesis.

- Prof. Dr. Wolfgang Kowalsky for kindly taking over the co-report of this thesis.

- my tutor Dr. habil. Andrey Bakin for always being supportive, encouraging and willing to find a way out when I hit a dead end. I really appreciate your effort and I just want to say a really big ”thank you, Andrey”, for your continuous assistance throughout my PhD studies and for always being there when needed!

- my tutor Dr. habil. Hergo Wehmann for his willingness to answer any questions about measurements methods and techniques at all times. I am very grateful that you always took the time for discussions and that you shared some of your vast knowledge concerning solid state physics with me. The conversations with you were definitely of great help!

- our cooperation partners. Among those, I would like to especially express my gratitude to Peter Hinze and Dr. Thomas Weimann from the Physikalisch Technische Bundesanstalt (PTB). The characterization of single nanowires presented in this thesis could not have been performed without your assistance and I really enjoyed the days I was spending with you in the PTB's clean room.
  Additionally, I would like to thank Dr. Sibylle Sievers and Dr. Martin Albrecht (also from the PTB) for providing some of the MFM measurements presented in this work and for letting me use their SQUID magnetometer. When it comes to SQUID measurements, I especially want to thank Joachim Lüdke (PTB), not only for sharing his morning tea with me but also for applying his special tricks when it came to fitting the samples into the sample holder.
  Very special thanks to Dr. Dirk Weber (at that time at the University of Bielefeld) for many fruitful discussions about the tricky business of characterizing single ZnO nanowires.
  Prof. Dr. Carsten Ronning (at that time at the University of Göttingen) for implantation of the nanowire samples.
  Dr. Herbert Schmidt from the University of Bonn for providing the EDS, TEM and EELS data.

Dr. Heiko Bremers from the Technical University Braunschweig for performing the XRD analysis.

- the Bundesministerium für Bildung und Forschung (BMBF) for the financial support in the form of the project nanoQUIT.
- Doris Rümmler and Angelika Schmidt for their assistence. Thanks for the innumerable times you were supporting me technically (and also morally when necessary - thank you Doris!). I am also grateful to Gerhard Palm for pressing of the nanopowder samples.
- Angelika John for her help with administrative tasks.
- Manfred Karsten and Wolfgang Weiß for their technical assistance.
- Karl-Heinz Lachmund for the excellent IT support and for ensuring the running of the measurement equipment.
- my *IHT* collegues. I would like to extend my warmest thanks to all of you for the good time I had at the *IHT* - I really enjoyed working with you!
  Special thanks also to the colleagues providing the samples - Bianca Postels, Arne Behrends, Dr. Augustine Che Mofor, Dr. Hamid El-Shaer. To Mohamed Al-Suleiman for the PL measurements and to Alexander Wagner for the humidity dependent I-Vmeasurements. Furthermore, thanks to Jafet Fernandez, Stephan Merzsch and Ole Peters for good co-operation during their study thesis.
  Thanks also to Hergo Wehmann, Arne Behrends, Sönke Fündling and Stephan Merzsch for much fun during lunch-time jogging.
- Anita Kessels and Hilke Heppelmann. Thank you so much not only for critically reading this manuscript but also for the good times I had with you during our jogging, swimming and biking sessions and all the fun besides sports.
- my mother and grandparents for always supporting me. Liebe Doris, liebe Lore, liebe Lotte! Einfach nur vielen vielen Dank für alles!
  Thanks also to my brother Thomas for always encouraging me.
- Dirk. My biggest THANKS to you - thank you for ”going d’accord” with me!

Thank you!
Eva Schlenker